

2015-02-02

# The Aerodynamics of Rapid Area Change in Perching Manoeuvres

Polet, Delyle

---

Polet, D. (2015). The Aerodynamics of Rapid Area Change in Perching Manoeuvres (Master's thesis, University of Calgary, Calgary, Canada). Retrieved from <https://prism.ucalgary.ca>. doi:10.11575/PRISM/28007  
<http://hdl.handle.net/11023/2050>

*Downloaded from PRISM Repository, University of Calgary*

UNIVERSITY OF CALGARY

The Aerodynamics of Rapid Area Change in Perching Manoeuvres.

by

Delyle Thomas Polet

A THESIS

SUBMITTED TO THE FACULTY OF GRADUATE STUDIES  
IN PARTIAL FULFILLMENT OF THE REQUIREMENTS FOR THE  
DEGREE OF MASTER OF SCIENCE

DEPARTMENT OF MECHANICAL AND MANUFACTURING ENGINEERING

CALGARY, ALBERTA

JANUARY, 2015

© Delyle Thomas Polet 2015

# Abstract

This thesis presents a multidisciplinary study on bird perching to inspire Micro Aerial Vehicle design. Birds use a rapid pitch-up manoeuvre during perching, which modifies frontal area. Vorticity fields and forces are measured and simulated on an airfoil performing simultaneous deceleration and pitching to high angles of attack. Forces scale with the *shape change number*, a ratio between velocity of frontal area change and velocity change during deceleration. A simple analytical model agrees remarkably well with observed forces, and shows that the majority of forces are caused by boundary-layer separation and added-mass effects. Next, the kinematics of a small perching bird (the black-capped chickadee; *Poecile atricapillus*) are measured and parameterized with a three-dimensional analogue to the two-dimensional shape change number. The shape change numbers used by these birds are within the range of laboratory and computational tests discussed herein. These small birds use shape change numbers in proportion to the kinetic and potential energy at the start of the deceleration phase, in accordance with analytical predictions.

# Acknowledgements

First, I would like to thank the Natural Sciences and Engineering Research Council of Canada (NSERC) and Alberta Innovates Technology Futures (AITF) for their financial backing. I would like to thank my supervisor, Dr. David Rival, for providing guidance, encouragement and expertise throughout this degree. I also wish to thank Dr. Gabriel Weymouth for helpful insights, perspectives and feedback surrounding chapter 3. I would like to thank Mr. Jaime Wong, Mr. Tyler Christensen and Mr. Eric Limacher for assistance with the experiments and observations presented in this thesis. Finally, I would like to express my deepest gratitude to my friends and family, particularly to Heather, my loving and patient wife, for emotional and spiritual support throughout this degree.

# Table of Contents

<b>Abstract</b> . . . . .	i
<b>Acknowledgements</b> . . . . .	ii
Table of Contents . . . . .	iii
List of Tables . . . . .	v
List of Figures . . . . .	vi
List of Symbols . . . . .	xi
1 Introduction . . . . .	1
2 Overview of perching strategies in birds . . . . .	4
3 Unsteady dynamics of rapid perching manoeuvres . . . . .	11
3.1 Introduction . . . . .	11
3.2 Analytic arguments . . . . .	14
3.2.1 Model problem description and the shape change number . . . . .	14
3.2.2 Added-mass manipulation through frontal area change . . . . .	16
3.2.3 The added-mass force . . . . .	17
3.2.4 Circulatory forces . . . . .	19
3.2.5 The net force on an airfoil . . . . .	22
3.3 Experimental setup . . . . .	22
3.3.1 Force measurements . . . . .	23
3.3.2 Particle Image Velocimetry (PIV) . . . . .	25
3.4 Numerical method . . . . .	26
3.5 Results and discussion . . . . .	27
3.5.1 Velocity-field results . . . . .	28
3.5.2 Force history . . . . .	30
3.5.3 Time-averaged forces . . . . .	33
3.6 Summary and conclusions . . . . .	35
4 Rapid area change from pitch-up manoeuvres in a small perching bird . . . . .	38
4.1 Introduction . . . . .	38
4.1.1 Energy dissipation through rapid area change . . . . .	40
4.2 Experimental setup . . . . .	42
4.3 Results and discussion . . . . .	44
4.3.1 Overview of perching behaviour in <i>P. atricapillus</i> . . . . .	44
4.3.2 A three-dimensional analogue to the two-dimensional shape change number . . . . .	46
4.3.3 Rapid pitch-up manoeuvres and area change to increase force production . . . . .	48
4.4 Conclusions . . . . .	51
5 Synthesis and conclusions . . . . .	53
A A derivation of the added-mass force in a pitching and translating plate . . . . .	58
A.1 Motivating problem . . . . .	58
A.2 Added-mass force of a slowly-rotating thin airfoil . . . . .	61
A.3 Rapidly rotating airfoil . . . . .	63
A.4 Total added-mass force . . . . .	68
B Experimental error . . . . .	70

B.1	Force balance resolution and calibration error . . . . .	70
B.2	Uncertainty in angle of attack . . . . .	73
C	MATLAB scripts . . . . .	77
C.1	A script for batch shape change number calculation . . . . .	77
C.2	A script for calculating the gravity-based rotation matrix from a falling object. . . . .	83
C.3	Smaller functions called by the larger scripts . . . . .	87

## List of Tables

- 3.1 Estimates of uncertainty and signal-to-noise ratios ( $\text{SNR}_{\text{dB}}$ , in decibels) for lift and drag.  $\sigma_f$  is the measured standard deviation of the peak force coefficient across trials, and  $\sigma_t$  is the measured standard deviation of peak force time.  $C_{l\text{max}}$  and  $C_{d\text{max}}$  are the peak average lift and drag coefficients, respectively. . 25

# List of Figures and Illustrations

2.1	A sequence of still frames from two perching events for a female house sparrow ( <i>P. domesticus</i> ; top) and a black-capped chickadee ( <i>P. atricapillus</i> ; bottom). The central column is the moment where the bird first touched the feeder with its feet. The leftmost column is 24 ms before touchdown, while the rightmost column is 21 ms after touchdown. (Top row) In the first frame, the sparrow has fully extended its legs and has completed its final power stroke before landing. At touchdown, its legs are fully extended. 21 ms later, the sparrow has nearly come to a halt and its bent legs have absorbed most of the momentum. (Bottom row) In the first frame, the chickadee has just finished its final power stroke before landing. At touchdown, its legs are fully extended and its body is in line with the feeder. In the final frame, its body has collided with the feeder. The displacement of the chickadee in the first two frames is larger than the displacement of the sparrow; this indicates that the chickadee has a higher speed at touchdown. . . . .	6
2.2	A magpie filmed in Edmonton in August 2014 exhibiting a pitch-and-decelerate manoeuvre. (a) The bird finishing the last powerstroke before beginning the pitch-up manoeuvre (b-c) The pitch up manoeuvre involves a large increase in frontal area as the wings approach high angles of attack. The bird takes a more upright posture. (d-e) The wings are flexed slightly and the area decreases (f) less than 20 ms after touchdown, the bird begins retracting its wings. (Time between frames a-b: 88 ms; otherwise, 63 ms.) . . . . .	8
2.3	Frequency of deceleratory wingbeats ( $f$ , in Hz) is inversely proportional to mass ( $m$ , in g) on a log-log scale ( $R^2 = 0.81$ ). For three species, $m$ and $f$ were derived from Provini et al. (2014) and Berg & Biewener (2010) (squares). Remaining data points were derived from videos of perching sequences (diamonds). Frequency was calculated from the first wingbeat until the last wingbeat before touchdown. Mass was not measured for data collected from video trials; therefore, the average mass of that species according to Mugaas & Templeton (1970), Selander & Johnston (1967), Chaplin (1974), or Reese & Kadlec (1982) was used. . . . .	10
3.1	(a) A diagram showing the NACA0012 airfoil section with chord $c$ and pivot point marked by a black dot at a distance $cx_p^*$ from the leading edge. The instantaneous angle of attack $\alpha(t)$ and velocity at the pivot $U(t)$ are prescribed. (b) The kinematics used in experiments and simulations, plotted as a function of non-dimensional time $t^* = t/T$ , where $T$ is the time period of the manoeuvre. The velocity is scaled by the initial value $U_0$ , while the angle is scaled by the final value $\pi/2$ radians. $\alpha$ is varied with a cycloidal function given in equation (3.6). . . . .	15

3.2	Predicted circulatory (equation (3.14), dashed lines) and added-mass (equations (3.7) and (3.8), dotted lines) forces for the kinematic values given by equations (3.5-3.6). For lift, added-mass forces are most pronounced early in the manoeuvre but are quickly surpassed by circulatory forces. Peak circulatory drag dominates peak added-mass drag, however the parasitic thrust from the added-mass force overwhelms circulatory contributions late in the manoeuvre at high $\Xi$ . As $\Xi \rightarrow 0$ , added-mass lift and drag approach zero. . . . .	18
3.3	(Colour online) Sketch of the circulation production model. Velocity on the pressure side increases an amount equal to $U_{\perp}$ while the separated fluid on the suction side does not. This differential speed leads to a circulation per unit length $\gamma = \Delta u_{\parallel} = U_{\perp}$ at the trailing edge. The negative vorticity in the wake, shown here as a blue line, increases in length at the trailing edge at a rate equal to the trailing-edge speed: $\frac{ds}{dt} = U_{te}$ . This results in the total rate of change of circulation $\dot{\Gamma} = \frac{d\Gamma}{ds} \frac{ds}{dt} = U_{te}U_{\perp}$ . The circulation of the LEV increases by an equal and opposite amount in accordance with Kelvin's Theorem. . . . .	20
3.4	(a) PIV setup, showing a laser (A) projecting a laser sheet into the water tunnel from the side. The airfoil (C), attached to the traverse stage (B), was translated through the laser sheet with prescribed kinematics. A Photron SA4 high-speed camera (D) filmed the manoeuvre through the glass bottom of the water channel. (b) The airfoil attachment used for PIV and force measurements. The airfoil (C) was attached to a 6-component force/torque balance (F), which in turn was attached to a stepper motor (E). A plastic skim plate (G) prevented the formation of free-surface vortex funnels. The entire attachment was secured to the stage of a linear traverse (B), which sat on top of the water channel. (c) The airfoil attachment used for steady force measurements. The same airfoil (C), skim plate (G), and force balance (F) attachment as the unsteady setup (b) was used. The force balance was attached to a rotational stage (H), which in turn was secured to the traverse stage (B). . . . .	24
3.5	Normalized simulation error of the peak values of lift and drag coefficient for the $\Xi = 1/4$ , $Re = 2000$ test case as a function of the grid size $h$ . The error is computed relative to the values obtained using a fine $c = 400h$ reference grid. The solid lines indicate second-order convergence with $h$ and the dashed lines indicate first-order convergence. . . . .	28

3.6	PIV measurements ( $Re = 22000$ ) and simulations ( $Re = 2000$ ) of vorticity fields at $\Xi = 1/4$ (top) and $\Xi = 1/2$ (bottom). Black dotted lines represent the approximate $x$ -position of the centre-of-mass of the starting vortex and LEV. In the higher- $Re$ $\Xi = 1/4$ case, the starting vortex trails behind the LEV by a distance of $x/c = 1.4$ at $t^* = 0.67$ , whereas the starting vortex trails less than $x/c = 1.0$ behind the LEV in the other cases. The white arrows, shown at $Re = 2000$ , point to a stagnation streamline that connects with the airfoil near the trailing edge. At $t^* = 0.33$ , the stagnation streamline does not lie at the trailing edge. By $t^* = 0.67$ , the stagnation streamline has moved to the airfoil tip. The reference frame translates such that the origin is fixed at the pivot point. The airfoil is translating in the positive $x$ -direction. Grey-shaded areas in PIV plots denote regions that have been masked due to shadowing effects or visual obstruction. Vorticity is non-dimensionalized by $\omega^* = \omega c/U_0$ . . . . .	29
3.7	A comparison between force results from experiments at $Re = 22000$ (solid lines), simulations at $Re = 2000$ (dotted lines), and model predictions (dot-dash lines) for $1/8 \leq \Xi \leq 1/2$ . The magnitudes and timing of peaks in drag are similar between $Re$ cases. The timing of peak lift is similar as well. However, magnitudes of lift are similar only in the $\Xi = 1/2$ case. Model predictions are in close agreement with low- $Re$ force histories. . . . .	31
3.8	Lift and drag coefficients in non-dimensionalized time, plotted for varying $\Xi$ . The magnitudes of forces increase with $\Xi$ . At lower $\Xi$ , results approach quasi-steady predictions (solid black line). The model is overlaid as a dot-dash line. Experiment agrees with the model best at low shape change numbers. The $\Xi = 0$ case displays a peak lift at pre-stall angles of attack. . . . .	32
3.9	Time-averaged lift ( $\bar{C}_l$ ) and drag ( $\bar{C}_d$ ) are always positive and increase with $\Xi$ . Time-averaged lift is greater than drag at higher shape change numbers due to added-mass forces that contribute to lift but detract from drag (figure 3.2). Time-averaged lift is greater at $Re = 22000$ , compared to $Re = 2000$ results and model predictions, due to lift generation from vortex convection present in the higher- $Re$ cases. . . . .	34
4.1	A diagram of the setup used in data collection. A feeder was placed at the centre of an enclosure, which was open on two ends. Four cameras were positioned around the enclosure, forming effectively two reconstruction volumes: a smaller control volume for improved resolution of the pitch-up manoeuvre (green) and a larger control volume to capture the entire perching sequence (blue). . . . .	42

- 4.2 (A) A compound image from a single perching sequence, showing (left to right) the end of the ballistic phase ( $t_0$ ), the first frame where the wrist straightens ( $t_1$ ), and the final frame before the wrist flexes ( $t_2$ ). The shape change number is calculated between  $t_1$  and  $t_2$ .  $x'$  denotes the displacement vector of the center of mass from  $t_1$  to  $t_2$ . The angle between  $x'$  and the horizontal denotes the angle by which the vertical is rotated to form  $z'$ . Angle of attack is measured relative to the plane whose normal is  $z'$ . ( $t_0 \rightarrow t_1$  : 38 ms.  $t_1 \rightarrow t_2$  : 23 ms.) (B) Video still at  $t_1$ . Digitized points are shown as red circles. Points 1 and 2 are the beak and rump tip, respectively. The average of points 1 and 2 was used as a proxy for the CoM. Point 3 is the wing tip, distinguished as the next-to-last primary feather. Points 4 and 5 were used to measure wing chord and angle of attack and are, respectively, the shoulder and the tip of the secondary feather most proximal and posterior to the bird. (C) Video still at  $t_2$ . Note the more vertical orientation of both body and wing as compared to (B). The approximate location of the left wrist is shown as a blue arrow. For instantaneous CoM acceleration plots, the true rump location (point 2b) was digitized for one trial where it could be distinguished easily. . . . . 45
- 4.3 Members of *P. atricapillus* exhibit large center-of-mass accelerations along with a rapid increase in angle of attack from the moment when the wing wrist is straightened to the moment where it is bent again. The peak thrust near the point of arm flexion is likely an artifact due to head movement relative to the center of mass. . . . . 48
- 4.4 Members of *P. atricapillus* pitch their wings at a higher shape change number as the total energetic requirements of the perching manoeuvre increase. (a) The linear trend observed here is consistent with predictions based on analytic force models of pitching and decelerating airfoils, without corrections for the new shape change metric. The trial denoted with a circle is an outlier from the central tendency, exhibiting a much higher shape change number given its initial energy. The bird in this trial exhibited different landing patterns than the others. Excluding this outlier, the least-squares residual is shown as a dotted line ( $R^2 = 0.73$ ,  $p = 0.002$ ). The triangle represents the single trial where the wingtip could not be discerned for a minimum two frames after the pitch-up manoeuvre; in that case, the shape change number was calculated up to the last frame where wing speed could be determined according to equation 4.5. (b) Shape change number, when multiplied by a correction factor for the new three-dimensional metric (equation 4.11), continues to display a strong linear relationship with energetic requirements ( $R^2 = 0.58$ ;  $p = 0.01$ ). Multiplicity of kinematic parameters amplifies any digitization error, and is thought responsible for the slightly reduced  $R^2$  value in this case. . . . . 49
- 5.1 A black-capped chickadee showing covert deflection during a perching power stroke. This is indicative of a stalled state near the leading edge. It is unknown whether covert deflection plays a role in stabilizing the LEV. . . . . 54

5.2	For a small bird at the onset of the pitch-up phase, the sweep angle is approximately $90^\circ$ to the translation direction. Net forces generate lift and drag. At the end of the pitch-up phase, sweep angle is close to $180^\circ$ . Each wing may generate a parasitic thrust, as observed in chapter 3 at high angles of attack and low speed, but this thrust is largely canceled due to wing orientation. . .	56
A.1	The conformal maps used in this derivation. We start with a circle in the $\zeta$ plane rotating about its edge. We then rotate the cylinder by $\theta_p$ , and impose a free-stream velocity $U$ . Finally, we map this back to the $z$ plane using the Joukowski Transform (Eq. A.7) . . . . .	60
B.1	A comparison of lift coefficients from a variety of sources for the NACA0012 profile. <b>(a)</b> Lift coefficients from chapter 3 steady lift measurements at $Re = 2.2 \times 10^4$ and pre-stall angles of attach ( $\alpha < 10^\circ$ ) follow the trend of $2\pi\alpha$ and are bounded from above by lift coefficients measured at $Re = 5 \times 10^5$ , in accordance with theoretical expectations. Results from an aspect-ratio 6 wing (Laitone, 1997) at two turbulence levels are comparatively reduced. <b>(b)</b> Airfoil lift from chapter 3 has been reduced by the factor $6/8$ , in accordance with equation B.1 using the aspect ratio of the wing used by Laitone (1997). The reduced airfoil and wing lift are in close agreement, validating chapter 3 measurements and indicating that calibration error is small. . . . .	71
B.2	Rotation error for (a) $\Xi = 1/2$ and (b) $\Xi = 1/4$ . Diamonds denote the rotational position of the motor based on the command syntax, while the dotted line is the cycloidal function used to transform forces from the wing-fixed to laboratory frame in chapter 3. $t^*$ and $\alpha$ are defined as in chapter 3. . . . .	75

# List of Symbols, Abbreviations and Nomenclature

<u>Abbreviation</u>	<u>Definition</u>
BDIM	Boundary Data Immersion Method
CoM	Center of Mass
LED	Light-Emitting Diode
LEV	Leading-Edge Vortex
MAV	Micro Aerial Vehicle
PIV	Particle Image Velocimetry
SNR <sub>dB</sub>	Signal to Noise Ratio in decibels

<u>Symbol</u>	<u>Definition</u>
<b><i>a</i></b>	Acceleration
<i>A</i>	Wing planform area
<i>c</i>	Airfoil or wing chord length
$C_l, C_d$	Coefficient of lift and drag, respectively
$\bar{C}_l, \bar{C}_d$	Time-averaged coefficient of lift and drag, respectively
$C_{lmax}, C_{dmax}$	Peak average coefficient of lift and drag, respectively
$C_{F\phi}$	Chord-normal added-mass force coefficient
$C_{F\phi}$	Chord-normal circulatory force coefficient
$C_F$	Net chord-normal force coefficient
$C_{pL}, C_{pD}$	Pressure force lift and drag coefficients, respectively
<i>d</i>	Translational distance
<i>D</i>	Drag
<i>f</i>	Frequency
<i>F</i>	Force magnitude
$F_{AM}$	Added-mass force
$\mathbf{F}_\gamma$	Circulatory force
<i>g</i>	Acceleration due to gravity
<i>h</i>	Computational grid spacing
<i>i</i>	(As a subscript) frame number
<b><i>I</i></b>	Hydrodynamic impulse
<i>k</i>	Reduced frequency
<i>L</i>	Body length
<i>m</i>	Mass
$m_a$	Added mass
<i>n</i>	Sample size
$\hat{\mathbf{n}}$	Surface unit normal vector
<i>q</i>	Fluid speed
<i>r</i>	Radial distance (in polar coordinates)
<i>Re</i>	Reynolds number
<i>s</i>	Distance along trailing-edge wake
<i>S</i>	Wingspan

$t$	Dimensional time
$t_0$	Time at the end of the ballistic phase during perching
$t_1$	Time when wrist is first fully extended during perching
$t_2$	Time when wrist is first flexed after full extension during perching
$t^*$	Time, normalized by $T$
$T$	Time period
$\mathbf{u}$	Velocity
$u_{\parallel}, u_{\perp}$	Flow speed parallel and perpendicular to airfoil chord, respectively
$U$	Instantaneous translational speed
$U_0$	Initial or reference speed
$U_{\infty}$	Far-field flow speed
$U_{\perp}$	Trailing edge speed perpendicular to the airfoil chord
$U_{te}$	Total trailing edge speed
$\mathbf{v}_b$	Body velocity
$V$	Average speed of frontal area increase
$\mathbf{V}_0$	Translational velocity of a body in fluid
$\hat{\mathbf{x}}, \hat{\mathbf{y}}, \hat{\mathbf{z}}$	Unit vector in x, y and z directions
$\mathbf{x}$	Displacement relative to the origin
$x_p^*$	Pivot distance from leading edge, normalized by $c$
$\alpha$	Angle of attack
$\alpha_1, \alpha_2$	Angle of attack at $t_1$ and $t_2$ , respectively
$\gamma$	Circulation per unit length
$\Gamma$	Circulation
$\Delta E$	Total change in kinetic and potential energy during perching
$\Delta t$	Time increment
$\Delta U$	Characteristic velocity change during pitch-up
$\Delta z$	Height of a bird's CoM relative to perch at the onset of perching
$\eta_p^*$	Pivot distance from trailing edge, normalized by $c$
$\lambda$	Wavelength
$\nu$	Dynamic viscosity
$\Xi$	Shape change number
$\rho$	Mass per unit volume
$\sigma$	Standard deviation
$\sigma_f, \sigma_t$	Measured standard deviations of peak force magnitude and time, respectively
$\phi$	Velocity potential
$\Omega$	Rotational velocity of a body in fluid

# Chapter 1

## Introduction

Birds are an amazingly diverse clade of vertebrates, consisting of about 10 000 species (Campbell et al., 2008). As most of these species can fly, they represent a trove of inspiration for flying machines. Flight in birds has been evolving for more than 140 million years by some estimates (Zhou, 2004), making them incredibly experienced fliers. Man's experience with flying machines pales in comparison to nature's: the earliest examples of human-designed aircraft are kites (Deng, 2011) and hovering rotary tops (Leishman, 2006) from fifth-century B.C. in China. More recently, there has been great interest in developing small flying vehicles for use in reconnaissance, search and rescue, and surveying operations. Dubbed *Micro Aerial Vehicles* (MAVs), the goal is to develop aircraft that have a mass less than 30 g, a wingspan of about 8 cm, and speeds up to 65 km/h (Mueller & DeLaurier, 2001). These machines should also be manoeuvrable, able to navigate narrow corridors and regions hard to reach by humans.

Small birds fill these criteria well, are highly manoeuvrable flyers, and could serve as inspiration for the next generation of man-made flying machines. Birds must solve some of the same problems as MAVs (*e.g.* flight at small scales, navigation and obstacle avoidance) but must also contend with other problems (*e.g.* digestion and reproduction). Rather than blindly copying natural behaviour in artificial machines, we can first attempt to uncover the physical mechanisms used in the natural system. This allows us to not only understand how birds solve the problems we are interested in, but also to improve on these designs for our own specific needs.

Birds are able to perform an array of unsteady manoeuvres, allowing them to navigate cluttered airspaces. Mimicking these abilities would allow MAVs to complete the most de-

manding remote sensing tasks effectively and efficiently. Perching is one such manoeuvre, characterized by a controlled deceleration to land on a small platform. This thesis investigates the perching behaviour of birds and the underlying physics. Though perching is the central focus, many of the strategies used could be reapplied to other unsteady manoeuvres, such as braking or banking.

A multi-disciplinary approach is taken to explore the perching problem. Chapter 2 is an overview of perching strategies in birds, highlighting the complexity of the problem and some of the considerations biologists and engineers must take in interpreting behaviour. The scope is then narrowed to the use of *rapid area change* in perching birds; in particular, how a pitch-up manoeuvre alters frontal area and so drastically modifies forces.

Chapter 3 explores the physics of a pitch-and-decelerate manoeuvre in an airfoil as a simple abstraction of a perching bird. Simple analytic models are developed and incorporated from prior work, and are tested on simulations and experiments in a water tunnel. The model and observed forces help explain the advantages and disadvantages of such manoeuvres for perching birds. Chapter 4 returns to the actual organisms, showing how a small bird (the black-capped chickadee; *Poecile atricapillus*, Linnaeus 1766) uses rapid area change through a pitch-up manoeuvre to quickly dissipate energy and land safely. Some of the behaviours observed in these birds are explained through the physics developed in chapter 3. Chapter 5 is a synthesis of the previous chapters, reviewing how simple analytical models explain forces observed in a perching airfoil, how this in turn explains behaviour in the black-capped chickadee, and the implications for MAV design. Finally, interesting avenues of future research are highlighted.

Chapters 3 and 4 are written in the format of journal articles. The author of this thesis is first author on both these works. Chapter 3 has been accepted for publication in the *Journal of Fluid Mechanics* (2015, in press), under the title *Unsteady Dynamics of Rapid Perching Manoeuvres*. The co-authors, Dr. David Rival and Dr. Gabriel Weymouth, advised

the primary author in data collection, modelling and analysis and edited the manuscript before submission. Dr. Weymouth performed the computational experiments. Chapter 4 is a preliminary manuscript intended for publication in the journal *Bioinspiration and Biomimetics* under the title *Rapid area change from pitch-up manoeuvres in a small perching bird*. Dr. David Rival is co-author on this work. Three appendices are also included in this thesis. Appendix A shows a derivation of the added-mass force on a pitching and accelerating airfoil. Appendix B discusses chapter 3 experimental error in greater detail. Appendix C provides MATLAB<sup>TM</sup> scripts for use in kinematic analyses of perching birds.

## Chapter 2

### Overview of perching strategies in birds

Perching is an unsteady manoeuvre that has attracted the attention of biologists and engineers alike. It is complex, as the bird must carefully balance competing costs: too much speed at landing, and the bird risks crashing into the perch; too little speed requires extra energy to stay airborne. The rate of deceleration is equally important; slow deceleration requires long periods of sustained lift, but rapid deceleration hinders control and puts greater stresses on the bird. Optimal kinematics for a controlled, efficient and safe landing are not obvious, and are likely to change depending on circumstance, species and size.

A perching bird must coordinate visual cues, proprioception, muscle activation and careful kinematic adjustments to stay airborne; it must decelerate safely but efficiently, respond to changes in fluid speed, and land in a controlled manner on a small landing platform. The numerous demands on the bird yield many factors that contribute to variation in perching behaviour. Presently, these factors are broadly categorized as physiological, cognitive and aerodynamic. The first two categories are presented generally for completeness, while the latter is the central focus of this thesis.

Physiological factors play into a bird's ability to perch effectively. A bird needs to be able to not only land, but cruise, takeoff, and perform other biological functions besides flight. These biological needs sometimes compete; thus the design of a bird is a compromise weighted by its ecological specialty. Birds that perform more unsteady manoeuvres tend to have relatively thick wing skeletal elements, and a relatively large distribution of forearm muscle (Dial, 1992b). Birds lacking these features have more difficulty performing unsteady manoeuvres such as perching. Power demands on the main downstroke muscle in rock pigeons (*Columba livia*, Gmelin 1789) are higher during landing flight than takeoff and cruising flight

(Biewener et al., 1998), and members of the same species with forearm muscles disabled are able to maintain cruising flight but not landing (Dial, 1992b). Landing also strains the skeletal elements of legs. Starlings (*Sturnus vulgaris*, Linnaeus 1758) sustain an average of 1.8 times their body weight in the legs during landing (Bonser & Rayner, 1996), while rock pigeons sustain up to eight times their body weight in landing (Green & Cheng, 1998).

Cognitive and behavioural factors can influence a bird's perching behaviour. Green & Cheng (1998) found that rock pigeons would approach a novel perch more slowly than a familiar perch. Tobalske et al. (2004) found hummingbirds frightened into a take-off generated larger forces compared to individuals who took off voluntarily to feed. Provini et al. (2014) suggested emotional state may also affect landing behaviour in a similar way. Foraging strategies can also influence the observed kinematics in birds. Black-capped chickadees (*Poecile atricapillus*, Linnaeus 1766) in Calgary, Alberta were observed to land at a feeder, grab a single seed and dart off quickly ( $n=5$ ). In contrast, house sparrows (*Passer domesticus*, Linnaeus 1758) fed at the same feeder for minutes at a time ( $n=10$ ). Accordingly, speed at touchdown was larger in chickadees compared to sparrows (figure 2.1), consistent with the preference of chickadees to spend less time in the open.

Though all these factors influence perching in birds, it would be intractable to consider them all in detail in the present work. Instead, this thesis focuses on the *aerodynamics* of perching in small birds: how and to what degree the observed kinematics in birds can be explained through aerodynamic mechanisms. Once we understand the aerodynamics of perching, we can distinguish which designs in nature are best for force production under a given set of circumstances, and better replicate and improve on these designs in biomimetic flying machines.

Aerodynamic mechanisms account for the majority of energy dissipation during perching. Provini et al. (2014) observed 32 times more energy dissipated aerodynamically than through the legs in a perching diamond dove (*Geopelia cuneata*, Latham 1801). The pre-



Figure 2.1: A sequence of still frames from two perching events for a female house sparrow (*P. domesticus*; top) and a black-capped chickadee (*P. atricapillus*; bottom). The central column is the moment where the bird first touched the feeder with its feet. The leftmost column is 24 ms before touchdown, while the rightmost column is 21 ms after touchdown. (Top row) In the first frame, the sparrow has fully extended its legs and has completed its final power stroke before landing. At touchdown, its legs are fully extended. 21 ms later, the sparrow has nearly come to a halt and its bent legs have absorbed most of the momentum. (Bottom row) In the first frame, the chickadee has just finished its final power stroke before landing. At touchdown, its legs are fully extended and its body is in line with the feeder. In the final frame, its body has collided with the feeder. The displacement of the chickadee in the first two frames is larger than the displacement of the sparrow; this indicates that the chickadee has a higher speed at touchdown.

cise kinematics generating aerodynamic forces vary between species and depend on external factors (*e.g.* distance from the perch or ambient windspeed (Carruthers et al., 2007)). However, some patterns emerge. Birds reorient their bodies from a horizontal to vertical posture during landing (Carruthers et al., 2007; Berg & Biewener, 2010; Provini et al., 2014), and exhibit higher angles of attack and stroke amplitude when landing or flying more slowly (Dial, 1992a; Tobalske & Dial, 1996; Tobalske et al., 2003; Carruthers et al., 2007; Berg & Biewener, 2010).

Several authors have also noted a change in wing shape during landing (Carruthers et al., 2007; Berg & Biewener, 2010). Adjustments of wing shape and a consistent pattern of more upright posture suggest that modification of frontal area generates forces during perching. Studies on rapid area change have shown that large forces can be explained through a combination of boundary-layer vorticity effects and added-mass manipulation (Wibawa et al., 2012; Weymouth & Triantafyllou, 2012, 2013). An obvious yet overlooked method of changing frontal area during flight is to simply pitch control surfaces to larger angles of attack.

Carruthers et al. (2007) noted that a steppe eagle (*Aquila nipalensis*, Hodgson 1833) exhibited a “rapid pitch-up phase” at the end of its perching manoeuvre. This occurred regardless of a gliding or flapping approach. Figure 2.2 shows a smaller black-billed magpie (*Pica hudsonia*, Sabine 1823) filmed in Edmonton, Alberta using a rapid pitch-up manoeuvre to land. A flapping approach is first taken by the bird; it then flexes its wings fully, rapidly increases angle of attack and body angle to the horizontal, and decelerates.

Some authors have begun investigating pitch-up manoeuvres in the context of perching. Visbal (2012) studied a pitch-and-decelerate manoeuvre from  $\alpha = 0$  to  $45^\circ$  computationally, while Granlund et al. (2010) presented preliminary experimental results for a similar manoeuvre to  $\alpha = 90^\circ$ . Both authors showed that forces depart from equivalent constant-free-stream measurements for  $\alpha > 30^\circ$ . Wang & Eldredge (2012) used a vortex-stepping technique with

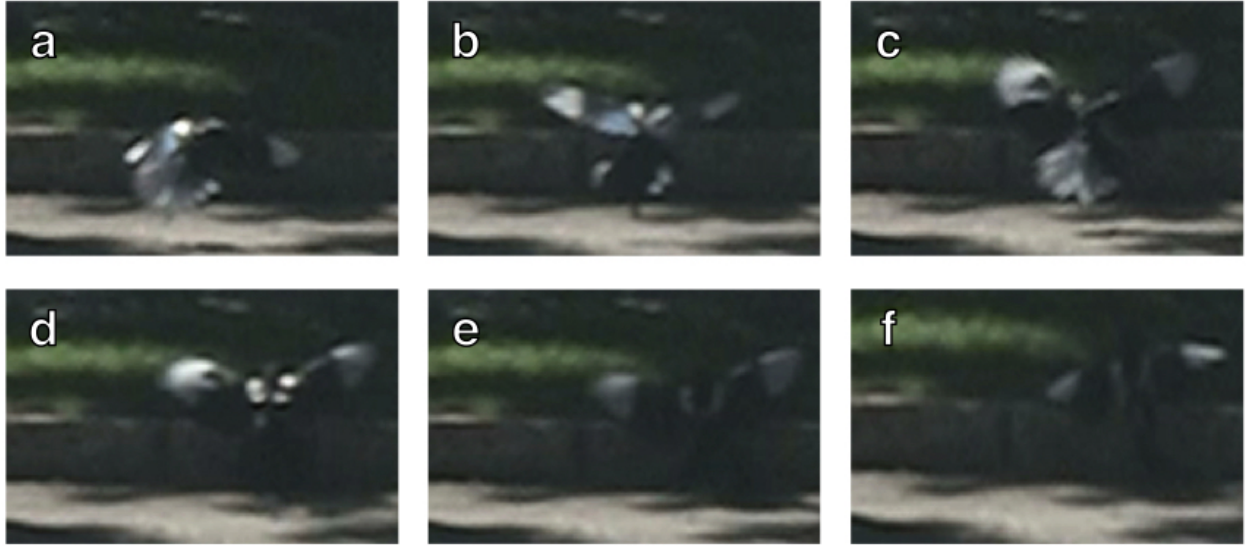


Figure 2.2: A magpie filmed in Edmonton in August 2014 exhibiting a pitch-and-decelerate manoeuvre. (a) The bird finishing the last powerstroke before beginning the pitch-up manoeuvre (b-c) The pitch up manoeuvre involves a large increase in frontal area as the wings approach high angles of attack. The bird takes a more upright posture. (d-e) The wings are flexed slightly and the area decreases (f) less than 20 ms after touchdown, the bird begins retracting its wings. (Time between frames a-b: 88 ms; otherwise, 63 ms.)

only two point vortices to predict forces in a perching manoeuvre. This technique involved far fewer degrees of freedom than typical computational methods, and demonstrated decent agreement with experiment. However, a time-stepping procedure, even with a small number of vortices, does not directly connect kinematics to observed forces. The lack of physical understanding of the mechanisms of force generation in perching manoeuvres inhibits their application to MAVs and limits understanding biological systems.

While Berg & Biewener (2010) measured average angle of attack in time for individual deceleratory strokes, no existing studies have quantified the rate of continuous pitch-up in a perching bird; therefore, appropriate pitch rates to test experimentally are not known. The tests run by Visbal (2012) and Granlund et al. (2010) were performed at  $Re < 50\,000$ , while the magpie and eagle that were observed performing pitch-and-decelerate manoeuvres operate at  $Re > 100\,000$ . The assumption that rapid pitch-up is appropriate for perching aircraft as small as MAVs is as yet without basis in the animal kingdom.

To explore possible differences in perching strategies across size ranges, four bird species

were filmed in perching manoeuvres in Calgary and Edmonton, Alberta between July 2013 and September 2014. A variety of feeders were used, with no attempt to restrict approach speed, direction or distance from takeoff to landing. The inconsistent observational conditions would tend to lead to greater variety in perching kinematics. Yet, remarkably, a consistent pattern emerges.

Wingbeat frequencies were calculated from the first deceleratory wingbeat to the final wingbeat before touchdown for a number of perching sequences. Frequency decreases regularly with body mass on a log-log scale (figure 2.3). An inverse proportionality between size and stroke frequency is also observed in steady flight (Pennycuick, 1996)<sup>1</sup>. Pennycuick (1975) attributed the reduction of frequency with increased mass to minimum lift requirements and the scaling of muscle power to wing inertia. Similar arguments likely apply to the scaling of frequency with mass in perching manoeuvres.

In these video sequences, no gliding-type pitch-up manoeuvres similar to figure 2.2 were observed in any bird less than 100 g. This suggests that rapid pitch-up manoeuvres in small birds differ from large birds. The scaling of wingbeat frequency with mass may be responsible.

Smaller birds need to flap frequently to maintain lift, and birds of mass  $< 30$  g with short, rounded wings seldom glide, preferring instead to use a bounding-flight pattern (Tobalske et al., 2007). Any dynamic changes in angle of attack must therefore occur during power strokes with limited duration, whereas larger birds can change wing shape and orientation in a slow gliding approach (Carruthers et al., 2007).

To explore physical mechanisms of force generation in a pitch-and-decelerate manoeuvre, an experimental investigation is performed on a pitching airfoil in chapter 3. A simple analytical model, developed from the perspective of pitch-up as a rapid area change mechanism,

---

<sup>1</sup>In reality, Pennycuick (1996) showed that flapping frequency scales with a multiplicity of morphological factors, and observed a small *positive* proportionality with mass, holding other variables constant. However, wing span (S) and area (A) scale negatively with stroke frequency (Pennycuick, 1996), and since S and A increase strongly with mass (Taylor & Adrian, 2014), a general trend of decreasing stroke frequency with increasing mass is expected.

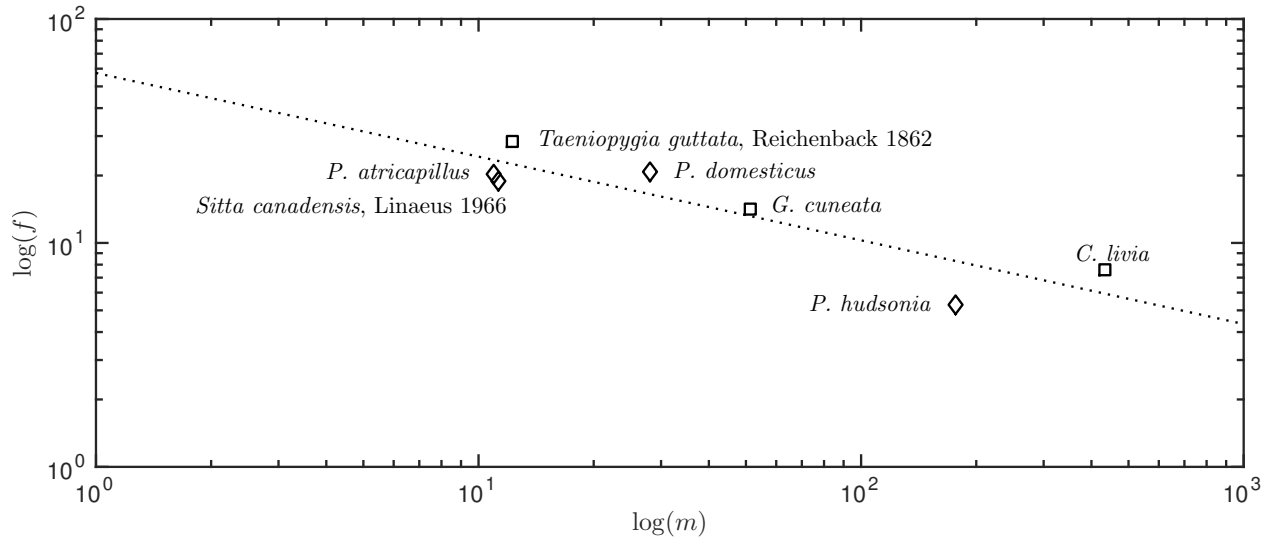


Figure 2.3: Frequency of deceleratory wingbeats ( $f$ , in Hz) is inversely proportional to mass ( $m$ , in g) on a log-log scale ( $R^2 = 0.81$ ). For three species,  $m$  and  $f$  were derived from Provini et al. (2014) and Berg & Biewener (2010) (squares). Remaining data points were derived from videos of perching sequences (diamonds). Frequency was calculated from the first wingbeat until the last wingbeat before touchdown. Mass was not measured for data collected from video trials; therefore, the average mass of that species according to Mugaas & Templeton (1970), Selander & Johnston (1967), Chaplin (1974), or Reese & Kadlec (1982) was used.

demonstrates how a bird can produce enough force to land despite a reduction of speed and high angles of attack. The relevance of pitch-and-decelerate manoeuvres to birds under 30 g is established in chapter 4, where such manoeuvres are observed and quantified in a small bird (the black-capped chickadee, *Poecile atricapillus*, Linnaeus 1766). The simple analytical predictions developed in chapter 3 explain some of the perching behaviour described in chapter 4. In chapter 5, the thesis is synthesized, the relevance of pitch-up manoeuvres to MAVs is discussed, and future directions are proposed.

# Chapter 3

## Unsteady dynamics of rapid perching manoeuvres

### Abstract

A perching bird is able to rapidly decelerate while maintaining lift and control, but the underlying aerodynamic mechanism is poorly understood. In this work we perform a study on a simultaneously decelerating and pitching airfoil section to increase our understanding of the unsteady aerodynamics of perching. We first explore the problem analytically, developing expressions for the added-mass and circulatory forces arising from boundary-layer separation on a flat-plate airfoil. Next, we study the model problem through a detailed series of experiments at  $Re = 22000$  and two-dimensional simulations at  $Re = 2000$ . Simulated vorticity fields agree with Particle Image Velocimetry measurements, showing the same wake features and vorticity magnitudes. Peak lift and drag forces during rapid perching are measured to be more than 10 times the quasi-steady values. The majority of these forces can be attributed to added-mass energy transfer between the fluid and airfoil, and to energy lost to the fluid by flow separation at the leading and trailing edges. Thus, despite the large angles of attack and decreasing flow velocity, this simple pitch-up manoeuvre provides a means through which a perching bird can maintain high lift and drag simultaneously while slowing to a controlled stop.

### 3.1 Introduction

Birds execute precise manoeuvres, such as banking, braking, takeoff and landing, allowing them to navigate dense forests and urban environments. Micro Aerial Vehicles (MAVs) are contemporary flying machines operating on the same scale as small birds, and are designed to

carry out remote sensing and small payload delivery tasks in cluttered airspaces. Mimicking the manoeuvrability of birds, particularly the ability to land safely on narrow platforms, would allow them to complete these tasks effectively and efficiently. Though recent advances have been made in designing MAVs that can land on a perch (Doyle et al., 2011; Moore et al., 2014; Reich et al., 2009), existing MAVs still fall short in achieving the control, speed and precision of natural flyers in landing manoeuvres.

Birds are tremendously adept at controlled, fast landings. Provini et al. (2014) observed that zebra finches are able to decelerate from 15 to 7 body lengths per second in 0.15 seconds, entirely through aerodynamic means. Though the exact kinematic motion used by birds in perching manoeuvres varies between species (Berg & Biewener, 2010; Provini et al., 2014), one relatively simple motion is for a bird to pitch its wings continuously from near-horizontal to approximately  $90^\circ$  angle of attack. Carruthers et al. (2007) observed this motion in a Steppe Eagle and noted that the eagle gained altitude quickly during the landing phase, implying that large lift was produced. However, steady-state analysis predicted that the bird would lose lift at high angles of attack due to stall effects and reduced airspeed (Carruthers et al., 2010). When decelerating most rapidly and gaining height, the eagle entered a “rapid pitch-up phase”, in which it increased its angle of attack quickly while simultaneously spreading its wings.

To model the aerodynamics of the pitch-up wing motion in landing birds, we consider an airfoil that rapidly increases its angle of attack while simultaneously decelerating. Though bird flight and landing is a three-dimensional problem, two-dimensional flow topologies often dominate in highly-unsteady manoeuvres, as was shown by Garmann et al. (2013), and so we restrict ourselves to the two-dimensional pitch-up problem.

When an airfoil pitches to high angles of attack, its frontal area rapidly increases. Rapid frontal area change of bodies in acceleratory manoeuvres results in significant added-mass effects, notably the recapture of added-mass energy as demonstrated by Weymouth & Tri-

antafyllou (2012) in a shrinking cylinder and Weymouth & Triantafyllou (2013) in a squid-like deflating body. Rapid area change can also affect boundary-layer vorticity, causing sudden global shedding of vorticity in a vanishing airfoil (Wibawa et al., 2012) and annihilation of boundary-layer vorticity in a shrinking cylinder (Weymouth & Triantafyllou, 2012).

These above studies have all looked at the fluid dynamics of a body with rapidly-decreasing area. However, the case of a body with rapidly-increasing frontal area has seen comparatively little attention, despite the potential to inform biological and technological designs. We show that the case of a pitching and decelerating airfoil manipulates added-mass forces in a similar way to other rapid area change problems, but here the rapid increase in area bears unique performance challenges. Additionally, the rotation of the body produces lift and dynamic forces from boundary-layer separation, which have hitherto not been considered in rapid area change problems.

To study the unsteady dynamics of pitch-up during stopping manoeuvres, we first develop a low-order analytic model for the lift and drag force-history on an airfoil performing simultaneous pitch and deceleration. Such a model provides two benefits: (a) it identifies the salient features of the flow in order to understand physical mechanisms, and (b) it may be used to predict forces for MAV control at low computational cost.

Next, a complete set of numerical simulations and experimental studies are performed. The results demonstrate that a high-speed pitch and deceleration manoeuvre produces remarkable instantaneous lift and drag forces. By examining these results in the context of the analytic model, we determine that the majority of these forces can be attributed to (i) added-mass energy transfer between the fluid and airfoil, and (ii) to energy dissipated into the fluid by boundary-layer separation at the leading and trailing edges. These effects combine to achieve instantaneous and integrated forces compatible with the perching abilities of birds.

## 3.2 Analytic arguments

We first develop an analytic model of the forces produced during a pitch-up and stop manoeuvre to understand mechanisms of lift and drag generation in perching. Recent studies (Ol et al., 2009; Baik et al., 2012; Pitt Ford & Babinsky, 2013) have shown that classical potential flow theory from Theodorsen (1935), von Kármán & Sears (1938) and Wagner (1925) can provide reasonable predictions for the force histories of unsteady airfoils, even for low- $Re$  cases with pronounced boundary-layer separation. These models have explanatory power as well, as they allow simple decomposition of the added-mass and circulatory forces. However, these potential flow models assume a small angle of attack and a planar wake (Theodorsen, 1935; von Kármán & Sears, 1938; Wagner, 1925), assumptions that are violated with rapid pitch-up to high  $\alpha$ .

In this study we use an added-mass model valid for arbitrary angles of attack and pitch rate and derive a circulatory force model for highly-separated flows around non-oscillatory airfoils. The combined model has no free parameters, being dependent only on the prescribed kinematics of the pitching and decelerating airfoil.

### 3.2.1 Model problem description and the shape change number

Consider an airfoil with chord length  $c$  that is initially at an angle of attack  $\alpha = 0^\circ$  and moving at a constant forward velocity  $U_0$ . As a simple model of a bird's wing during perching manoeuvres, this airfoil section is made to rapidly rotate perpendicular to the translation direction, that is to  $\alpha = 90^\circ$ , while simultaneously decelerating to a full stop over time period  $T$ . This system and its kinematics are sketched in figure 3.1.

We parameterize the magnitude of the geometry change of the system with the *shape change number*

$$\Xi = \frac{V}{U_0}, \quad (3.1)$$

where  $V \equiv c/T$  is the average speed at which the frontal width of the airfoil increases over

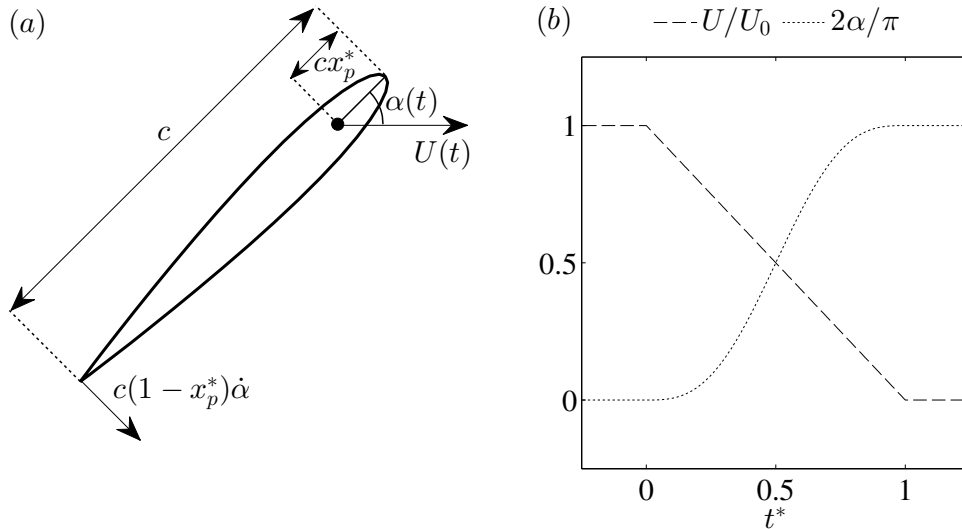


Figure 3.1: (a) A diagram showing the NACA0012 airfoil section with chord  $c$  and pivot point marked by a black dot at a distance  $cx_p^*$  from the leading edge. The instantaneous angle of attack  $\alpha(t)$  and velocity at the pivot  $U(t)$  are prescribed. (b) The kinematics used in experiments and simulations, plotted as a function of non-dimensional time  $t^* = t/T$ , where  $T$  is the time period of the manoeuvre. The velocity is scaled by the initial value  $U_0$ , while the angle is scaled by the final value  $\pi/2$  radians.  $\alpha$  is varied with a cycloidal function given in equation (3.6).

the course of the manoeuvre. Defining the inline deceleration as  $\dot{U} = U_0/T$  and substituting, we have  $\Xi = V^2/(\dot{U}c)$ , matching the definition of shape change number in Weymouth & Triantafyllou (2013). The parameter  $\Xi$  acts as a measure of the unsteadiness of the problem, similar to the reduced frequency,  $k = \pi fc/U_0$ , where  $f$  is a circular frequency. We choose to use  $\Xi$  in this work to emphasize that the motion is not cyclic and that the change in frontal area is fundamental to the perching problem.

For an airfoil rotating from  $\alpha = 0^\circ$  to  $90^\circ$  and simultaneously decelerating from  $U = U_0$  to 0 in time  $T$ , the magnitude of  $\dot{\alpha}$ ,  $\ddot{\alpha}$  and  $\dot{U}$  can be estimated as

$$\dot{\alpha} \propto \frac{1}{T} = \frac{U_0}{c} \Xi, \quad |\ddot{\alpha}| \propto \frac{1}{T^2} = \frac{U_0^2}{c^2} \Xi^2, \quad \dot{U} \propto \frac{U_0}{T} \Xi \quad (3.2)$$

so long as  $U$  and  $\dot{\alpha}$  are continuous functions in time. The relations given by (3.2) show that  $\Xi$  parameterizes the rate of rotation, rotational acceleration and translational acceleration.

### 3.2.2 Added-mass manipulation through frontal area change

This change in frontal area has pronounced consequences on the added-mass forces produced during the manoeuvre. These can be described from very simple relations, and merit a brief discussion for readers unfamiliar with the topic.

Consider a body accelerating in one dimension but allowed to modify its frontal area in time. As the body expands, it displaces more fluid, effectively increasing its added mass. Conversely, a reduction in frontal area would decrease the added mass in time. The one-dimensional added-mass force can be written as

$$F_{AM} = -\frac{\partial}{\partial t}(m_a U) = -\dot{m}_a U - m_a \dot{U} \quad (3.3)$$

where  $m_a$  is the instantaneous added-mass of the body. The terms on the right hand side arise respectively from the rate of change of the added mass ( $\dot{m}_a U$ ) and from the acceleration of the added mass ( $m_a \dot{U}$ ). Weymouth & Triantafyllou (2013) found that the added mass of an accelerating prolate spheroid decreased during body deflation ( $\dot{m}_a < 0$ ). This had a twofold effect in view of equation (3.3). The first was in achieving additional thrust by recovering added-mass energy (the  $-\dot{m}_a U$  term). The second was in reducing parasitic drag throughout the manoeuvre (the  $-m_a \dot{U}$  term). Both effects were beneficial for the performance goal of high acceleration.

However, there is a tradeoff for an expanding body when deceleration is desired. On the one hand, addition of added-mass from frontal area expansion ( $\dot{m}_a > 0$ ) would create drag through  $-\dot{m}_a U$ . But this would also *increase* the total added mass in time, making it difficult to stop the body late in the manoeuvre by producing a net thrust through  $-m_a \dot{U}$ . The sudden change in the direction of forces would tend to yield an uncontrolled perching manoeuvre, which is not observed (Green & Cheng, 1998; Berg & Biewener, 2010; Carruthers et al., 2007). In the next two sections we extend the simple one-dimensional force model equation (3.3) by discussing the effects of rotation on the added-mass force, and by modelling the circulation forces created through the production of vorticity.

### 3.2.3 The added-mass force

The general added-mass force normal to a flat-plate airfoil in translation and rotation at general angles of attack can be developed in a number of ways. The general boundary function method of Milne-Thomson (1968) can be applied to give the potential solution  $\phi$  for the case of a rotating and accelerating flat-plate, from which the added-mass force coefficient is determined to be

$$C_{F\phi} = \frac{\pi c}{2U_0^2} \left[ \dot{\alpha} \cos(\alpha)U + \sin(\alpha)\dot{U} + c\ddot{\alpha}(1/2 - x_p^*) \right] \quad (3.4)$$

where  $cx_p^*$  is the distance from the leading edge of the airfoil to the pivot location. Xia & Mohseni (2013) use an alternative rotating reference frame argument to develop the same added-mass force expression. In the context of equation (3.3), the first term in brackets in equation (3.4) arises from the time rate of change of added mass, and the second from linear acceleration of added mass. The final term arises from rotational acceleration absent in the one-dimensional analogy.

For the perching manoeuvre, we apply the relations given by (3.2) and see that the added-mass force in equation (3.4) should scale by no more than  $\Xi^2$ . We also note that the added-mass force disappears as  $\Xi \rightarrow 0$  (the quasi-steady limit), as expected.

We next study equation (3.4) through a prescribed set of kinematics representing simultaneous deceleration and pitch-up to large  $\alpha$ , relevant to perching manoeuvres in birds (Carruthers et al., 2007):

$$U = U_0(1 - t^*) \quad (3.5)$$

$$\alpha(t) = \frac{\pi}{2} \left[ t^* - \frac{\sin(2\pi t^*)}{2\pi} \right] \quad (3.6)$$

where  $t^* = t/T = tV/c$  is the non-dimensional time ( $0 \leq t^* \leq 1$ ). We also set  $x_p^* = 1/6$ . The resultant added-mass lift and drag

$$C_{l\phi} = C_{F\phi} \cos \alpha \quad (3.7)$$

$$C_{d\phi} = C_{F\phi} \sin \alpha \quad (3.8)$$

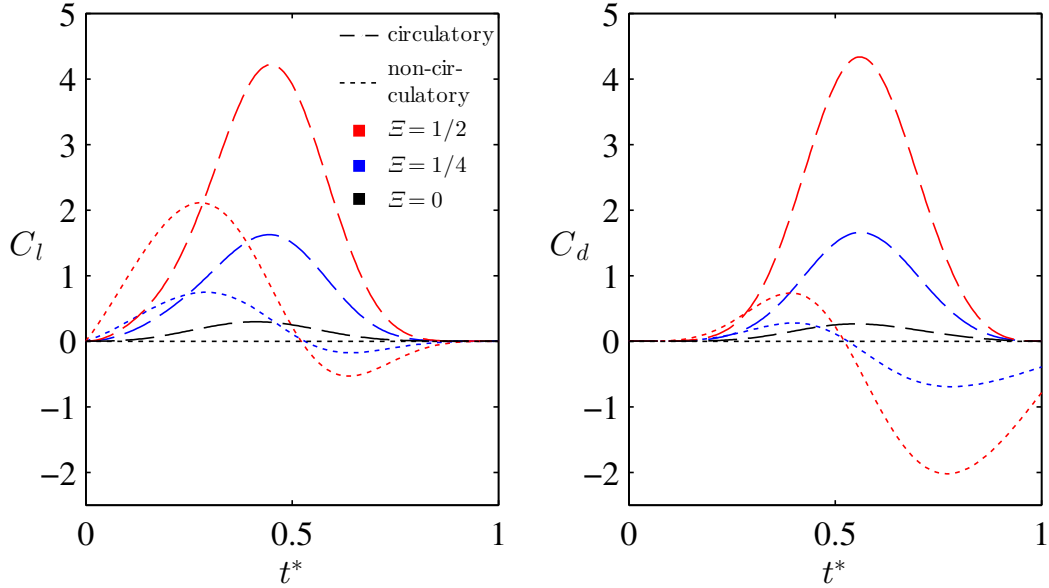


Figure 3.2: Predicted circulatory (equation (3.14), dashed lines) and added-mass (equations (3.7) and (3.8), dotted lines) forces for the kinematic values given by equations (3.5-3.6). For lift, added-mass forces are most pronounced early in the manoeuvre but are quickly surpassed by circulatory forces. Peak circulatory drag dominates peak added-mass drag, however the parasitic thrust from the added-mass force overwhelms circulatory contributions late in the manoeuvre at high  $\Xi$ . As  $\Xi \rightarrow 0$ , added-mass lift and drag approach zero.

are plotted in figure 3.2. The circulatory force is also plotted in this figure, and discussion of its contribution will be left to §3.2.4. Although the added-mass force is completely chord-normal, the peaks of lift and drag have different magnitudes and occur at different times due to the relative timing of  $C_{F\phi}$  and alpha. The added-mass force generates a significant parasitic thrust late in the manoeuvre, as discussed in §3.2.2. The magnitude of the force is increased by the rotational acceleration appearing in equation (3.4), as rotational acceleration must be positive early in the manoeuvre to begin rotation (generating lift) and negative late in the manoeuvre to halt rotation (generating thrust). However, the perfect recovery of added-mass energy implied by equation (3.3) requires the kinetic energy of the entire fluid domain to be zero at the end of the maneuver, and therefore neglects circulatory forces due to the vortex wake.

### 3.2.4 Circulatory forces

von Kármán & Sears (1938) demonstrated that an airfoil wake and bound circulation could be modeled as a superposition of equal strength, counter-rotating, point-vortex pairs. Each vortex pair in two dimensions has an associated hydrodynamic impulse,

$$\mathbf{I} = \Gamma \hat{\mathbf{z}} \times \mathbf{r} \quad (3.9)$$

where  $\Gamma$  is the circulation of one of the vortices,  $\hat{\mathbf{z}}$  is a unit vector pointing normal to the plane, and  $\mathbf{r}$  is the displacement vector from the positive to negative vortex centre. Since the circulatory force is related to the fluidic impulse by  $\mathbf{F}_\gamma = -\rho \frac{d\mathbf{I}}{dt}$ , this results in the following relation for the circulatory contributions to forces on the body:

$$\mathbf{F}_\gamma = -\rho \dot{\Gamma} \hat{\mathbf{z}} \times \mathbf{r} - \rho \Gamma \hat{\mathbf{z}} \times \dot{\mathbf{r}}. \quad (3.10)$$

Equation (3.10) shows that vortex forces can be altered through the addition or elimination of circulation to or from the vortex dipole ( $\dot{\Gamma}$ ) and by the convection of one vortex relative to the other ( $\dot{\mathbf{r}}$ ).

Analysis of the convective term in equation 3.10 is generally either accomplished by assuming the wake is stationary relative to the undisturbed fluid, which leads to a lift proportional to  $U\Gamma$  as in von Kármán & Sears (1938), or by numerically tracking the distribution of vorticity in the wake. As the transient perching flow is certain to be non-stationary, and as the goal of the model is to develop an understandable description of the forcing to complement further numerical and experimental testing, neither of these options is satisfactory. Moreover, in the limit of a very high-speed manoeuvre it is reasonable to assume that the flow simply will not have time to convect significantly, making this term negligible. Whereas in the limit of a very slow manoeuvre with significant vortex shedding, the average value of  $\Gamma$  in the wake will tend to zero, and therefore so will the mean convective force.

Therefore, for simplicity, we focus solely on the generation term. Pitt Ford & Babinsky (2013) showed that net bound circulation was negligible for a flat-plate airfoil undergoing a



pressure side increases an amount equal to the normal velocity of the airfoil whereas the suction side does not (figure 3.3). The velocity difference across the airfoil implies the fluid in the region of the trailing edge should be modelled as a vortex sheet with strength

$$\gamma = \Delta u_{\parallel} = U_{\perp} \quad (3.12)$$

where  $U_{\perp}$  is the velocity of the trailing edge of the airfoil normal to the chord. Over a time  $dt$  this sheet streams off the airfoil as the trailing edge covers a distance  $ds = U_{te}dt$ . As  $d\Gamma = \gamma ds$ , the production of circulation in the fluid is therefore

$$\dot{\Gamma} = U_{te}U_{\perp}. \quad (3.13)$$

From equation (3.11), this results in a force coefficient of

$$C_{F\gamma} = \frac{2U_{te}U_{\perp}}{U_0^2}. \quad (3.14)$$

It is informative to expand these speeds in terms of the airfoil kinematics. We have

$$U_{te} = \sqrt{U^2 + 2U\eta_p^*c\dot{\alpha}\sin\alpha + \eta_p^{*2}c^2\dot{\alpha}^2} \quad (3.15)$$

$$U_{\perp} = U\sin\alpha + \eta_p^*c\dot{\alpha} \quad (3.16)$$

$$\eta_p^* \equiv 1 - x_p^*. \quad (3.17)$$

Since  $\dot{\alpha} \propto \Xi$  from equation (3.2), when  $\Xi \gg 1$  we have  $F_{\gamma} \rightarrow \rho c(\eta_p^*c\dot{\alpha})^2$ , showing that the translational component becomes negligible and that the production of circulation is dominated by the rotation of the sharp trailing edge. Also note that as  $\Xi \rightarrow 0$ ,  $F_{\gamma} \rightarrow \rho c \sin(\alpha)U^2$ , showing that this circulatory model has a quasi-steady contribution. Unlike the steady Kutta lift force, which is valid for attached flows at low angles of attack, this mean force estimate is chord-normal and assumes fully detached flow.

Returning to figure 3.2, we note that the circulatory forces increase with  $\Xi$ , and the peak lift and drag at  $\Xi = 1/2$  are  $\sim 10$  times the steady-state values. Because the force is due solely to the production of leading and trailing-edge vorticity, energy is transferred in only one direction - from the airfoil to the wake.

### 3.2.5 The net force on an airfoil

By superimposing the added-mass (3.4) and circulatory (3.14) contributions we arrive at our analytic model of the force coefficient:

$$C_F = \frac{2}{U_0^2} \left[ \sin(\alpha)U + c\dot{\alpha}(1 - x_p^*) \right] \sqrt{U^2 + 2Uc\dot{\alpha}(1 - x_p^*) \sin(\alpha) + c^2\dot{\alpha}^2(1 - x_p^*)^2} + \frac{\pi c}{2U_0^2} \left[ \dot{\alpha} \cos(\alpha)U + \sin(\alpha)\dot{U} + c\ddot{\alpha}(1/2 - x_p^*) \right]. \quad (3.18)$$

This model depends only on two geometric and two kinematic (time-dependent) parameters: the chord length  $c$ , the pivot point  $x_p^*$ , the translational speed  $U(t)$ , and the angle of attack  $\alpha(t)$ .

We next present our experimental and numerical investigations of the two-dimensional perching problem. We then discuss the results in the context of our simplified analytic model.

## 3.3 Experimental setup

To quantitatively assess the fluid dynamics induced by rapid perching, we performed a set of experimental manoeuvres by varying  $\Xi$  using a towed NACA0012 airfoil. Forces on the airfoil were measured directly, and the velocity field was measured using Particle Image Velocimetry (PIV) to evaluate circulatory effects. All experiments were performed in a free-surface towing facility at the University of Calgary. The water channel test section is 38.6 cm wide, and water level was maintained at a 42 cm depth. An aluminum NACA0012 airfoil with 48 mm chord was positioned midway between the channel walls in a vertical orientation (figure 3.4b and 2c) and pierced the free surface from above. The airfoil tip was 4 mm from the bottom of the test section to reduce tip effects. Thus the airfoil had a submerged span of 416 mm and an aspect ratio of 8.7. The high aspect ratio further justifies the assumption of two-dimensional flow. A plastic skim plate of 112 mm diameter and 2 mm thickness was secured to the airfoil and sat 3 mm below the water surface. This skim plate eliminated the formation of free-surface funnel vortices. The airfoil was attached at one end to an ATI

Gamma force/torque balance. The force balance was attached to a two-phase stepper motor with  $0.9^\circ$  step angle. The pitching axis was  $c/6$  from the leading edge. The apparatus was fixed to a Parker linear traverse, which ran along the length of the water channel.

The airfoil first established a steady-state condition at  $\alpha = 0^\circ$  and speed  $U_0 = 0.45$  m/s for at least 10 chord lengths before beginning rotation and deceleration. The Reynolds number at the beginning of the manoeuvre is therefore  $Re = \frac{U_0 c}{\nu} = 22000$ , in the range relevant for small, highly-maneuvrable birds. The start of unsteady kinematics was synced through an induction sensor at a fixed position on the traverse track, which detected the passing traverse stage. The kinematics follow those shown in figure 3.1 and equations (3.5) and (3.6).

### 3.3.1 Force measurements

Force measurements were taken at a 1000 Hz sample rate (16 bit sample depth). Recorded force data was averaged across 10 trials for each test case. The force measurements were repeated for the same kinematics once water had been drained from the channel in order to measure the non-hydrodynamic inertia of the system. Force data was transformed from an airfoil-fixed frame to a lab-fixed frame, and the inertia was subtracted. The transformed data was further smoothed with a two-degree Butterworth low-pass filter. Filter frequency cutoff was chosen as 4 Hz for  $\Xi = 1/32$  and 10 Hz for  $\Xi = 1/2$ . Filter frequency cutoffs for intermediate  $\Xi$  were determined by interpolating linearly between these values. This method was found to best preserve peaks while eliminating noise. To avoid time-shifting of data, a forward-backward filtering technique was used. Force measurements were synchronized through the same induction sensor on the traverse track that triggered the deceleration.

Force measurements were also performed on the same airfoil at a constant speed (0.45 m/s) and constant angle of attack.  $\alpha$  was varied between trials from  $0^\circ$  to  $5^\circ$  with  $1^\circ$  increments, and from  $5^\circ$  to  $90^\circ$  with  $5^\circ$  increments using a rotational stage (figure 3.4c). The same measurements were performed for negative values of  $\alpha$  to assess the symmetry

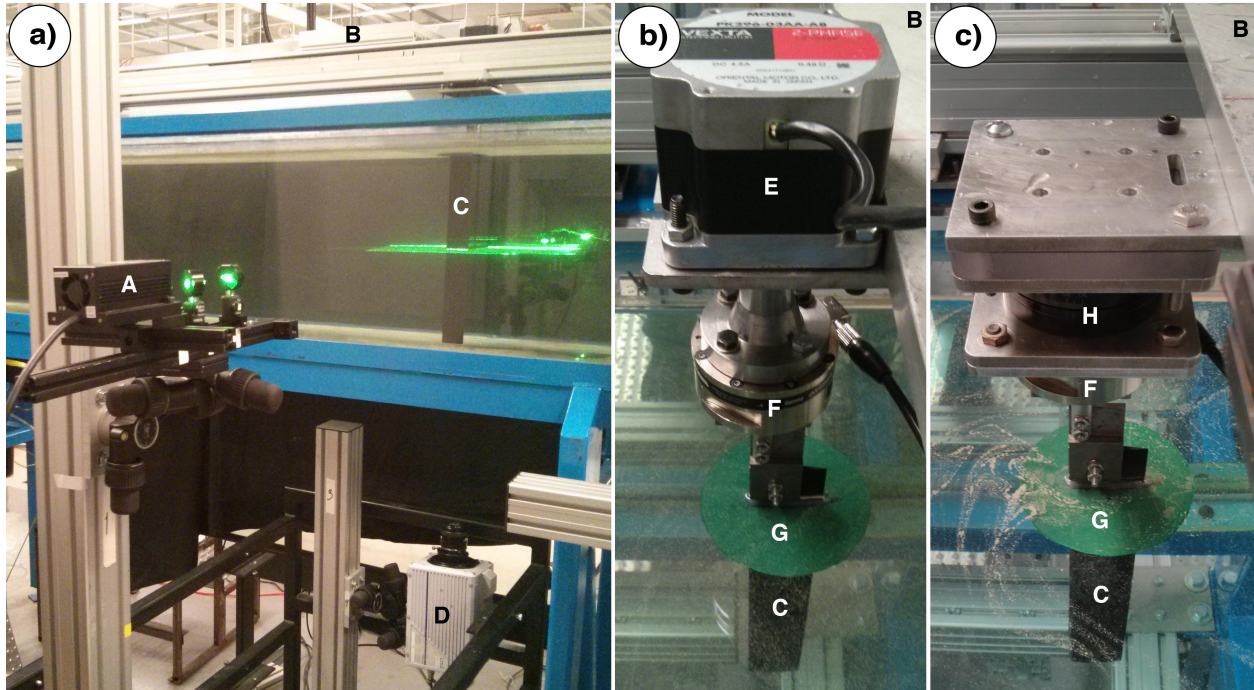


Figure 3.4: (a) PIV setup, showing a laser (A) projecting a laser sheet into the water tunnel from the side. The airfoil (C), attached to the traverse stage (B), was translated through the laser sheet with prescribed kinematics. A Photron SA4 high-speed camera (D) filmed the manoeuvre through the glass bottom of the water channel. (b) The airfoil attachment used for PIV and force measurements. The airfoil (C) was attached to a 6-component force/torque balance (F), which in turn was attached to a stepper motor (E). A plastic skim plate (G) prevented the formation of free-surface vortex funnels. The entire attachment was secured to the stage of a linear traverse (B), which sat on top of the water channel. (c) The airfoil attachment used for steady force measurements. The same airfoil (C), skim plate (G), and force balance (F) attachment as the unsteady setup (b) was used. The force balance was attached to a rotational stage (H), which in turn was secured to the traverse stage (B).

$\Xi$	Lift			Drag		
	$\sigma_f/C_{l_{\max}}$	$\sigma_t/T$	SNR <sub>dB</sub>	$\sigma_f/C_{d_{\max}}$	$\sigma_t/T$	SNR <sub>dB</sub>
1/32	0.040	0.017	-10	0.058	0.039	-14
1/16	0.074	0.017	-6.1	0.033	0.015	-9.2
1/8	0.017	0.008	-0.40	0.033	0.005	-3.7
1/4	0.028	0.014	7.3	0.068	0.009	2.2
1/2	0.028	0.015	13	0.057	0.017	4

Table 3.1: Estimates of uncertainty and signal-to-noise ratios (SNR<sub>dB</sub>, in decibels) for lift and drag.  $\sigma_f$  is the measured standard deviation of the peak force coefficient across trials, and  $\sigma_t$  is the measured standard deviation of peak force time.  $C_{l_{\max}}$  and  $C_{d_{\max}}$  are the peak average lift and drag coefficients, respectively.

of the setup. These measurements were used to make quasi-steady predictions ( $\Xi = 0$ ).

Quasi-steady force coefficients were computed as

$$C_F = \frac{2F}{\rho c S} \frac{U(\alpha)^2}{U_0^4}, \quad (3.19)$$

where  $F$  is the measured force,  $U(\alpha)$  is the speed of the airfoil at a particular angle of attack in the unsteady case, and  $U_0$  is the starting speed.

To estimate the uncertainty of force measurements, the standard deviations of peak lift and drag between trials at each shape change number were measured. Signal-to-noise ratios were also calculated between filtered and ensemble-averaged data. Values are presented in table 3.1. The measured standard deviations of peak forces do not exceed 8% of the corresponding average peak value, and the measured standard deviations of the time of peak forces do not exceed 4% of the corresponding period of deceleration and pitch.

### 3.3.2 Particle Image Velocimetry (PIV)

A 1 W, continuous-wave laser ( $\lambda = 532$  nm) projected a laser sheet into a plane orthogonal to the airfoil (figure 3.4a). This laser sheet was 21.1 cm above the water channel floor. The water was seeded with silver-coated, hollow glass spheres of 100  $\mu\text{m}$  diameter. These particles have a Stokes number of approximately  $2.4 \times 10^{-3}$ , and therefore were assumed to accurately follow the fluid flow. As the airfoil passed through the laser sheet, a Photron SA4

high-speed camera ( $1024 \times 1024$  pixel resolution) captured images at 250 frames per second. PIV data collection was synchronized with the same induction sensor on the traverse track that triggered the profile deceleration.

Raw images were pre-processed with a min/max contrast normalization filter of size  $14 \times 14$  pixels and a sliding-average subtraction filter of 50 pixel width. Velocity fields were calculated with a multi-grid/multi-pass cross-correlation algorithm using DaVis software (LaVision, v8.1.2). Velocity fields were averaged across 9 trials.

Based on the random error estimates of Raffel et al. (2007), pixel displacement uncertainty is taken as  $\delta s = \pm 0.1 \text{ px}$ . Propagation of uncertainty through velocity and vorticity with 4-pixel spacing between velocity vectors yields

$$\delta \omega^* = \frac{\delta s}{4 \Delta t \sqrt{n}} \frac{c}{U_0}, \quad (3.20)$$

where  $\delta \omega^*$  is the non-dimensional uncertainty in vorticity,  $\Delta t$  is the time interval between frames and  $n$  is the number of trials. Given equation (3.20), the uncertainty in non-dimensional vorticity for PIV measurements is estimated as  $\delta \omega^* = \pm 0.2$ .

### 3.4 Numerical method

A set of two-dimensional incompressible Navier-Stokes simulations of the model perching problem introduced in section 3.2 were used to provide high-resolution data with the exact kinematics of this challenging test case. To further this aim, the Reynolds number based on the initial steady speed  $U_0$  is set to  $Re = 2000$  in these simulations to ensure the model flow remains fully two-dimensional near the foil and the vortex structures remain clean and easily identifiable.

The Boundary Data Immersion Method (BDIM), a robust immersed boundary method suitable for dynamic fluid-structure interaction problems detailed in Weymouth & Yue (2011) and Maertens & Weymouth (2015), was used for this purpose. Briefly, the full Navier-Stokes equations and the prescribed body kinematics shown in figure 3.1 are convolved with

a kernel of support  $\epsilon = 2h$ , where  $h$  is the grid spacing. The integrated equations are valid over the complete domain and allow for general solid-body dynamics to be simulated. Previous work has validated this approach for a variety of dynamic rigid-body problems such as accelerating airfoils (Wibawa et al., 2012) and deforming-body problems (Weymouth & Triantafyllou, 2013). In Maertens & Weymouth (2015) this method was validated against stationary and flapping airfoil test cases at moderate  $Re$  and found to produce accurate and efficient numerical solutions.

A non-inertial computational domain is used with dimensions  $8c \times 8c$ , which translates and decelerates with the body but does not rotate. All cases use the no-slip and no-penetration boundary conditions on the solid/fluid interface. No-penetration conditions are applied on the top and bottom walls and a convection exit condition is used. The coupled BDIM equations are discretized using a finite-volume method (third-order convection and second-order diffusion) in space and Heun’s explicit second-order method in time. An adaptive time-stepping scheme is used to maintain stability. Figure 3.5 presents a grid convergence study on the peak lift and drag coefficients for the  $\Xi = 1/4$  test case. The results converge with second-order accuracy overall and the difference in the solution between an extremely fine reference grid (using 400 points along the chord) and a 200 point-per-chord grid is less than 2% in lift and drag. The velocity, pressure and vorticity fields for these grids are indistinguishable. This verifies the convergence of these viscous two-dimensional simulations and the 200 points-per-chord grid is used for the remainder of the paper.

### 3.5 Results and discussion

In §3.5.1, we present velocity-field measurements from two test cases ( $\Xi = 1/4$  and  $1/2$ ) using data from PIV at  $Re = 22000$  and BDIM simulations at  $Re = 2000$ . In §3.5.2, we present results from force measurements and compare them to the low-order analytic model. First, we compare instantaneous forces between  $Re$  at high  $\Xi$  and discuss differences in view

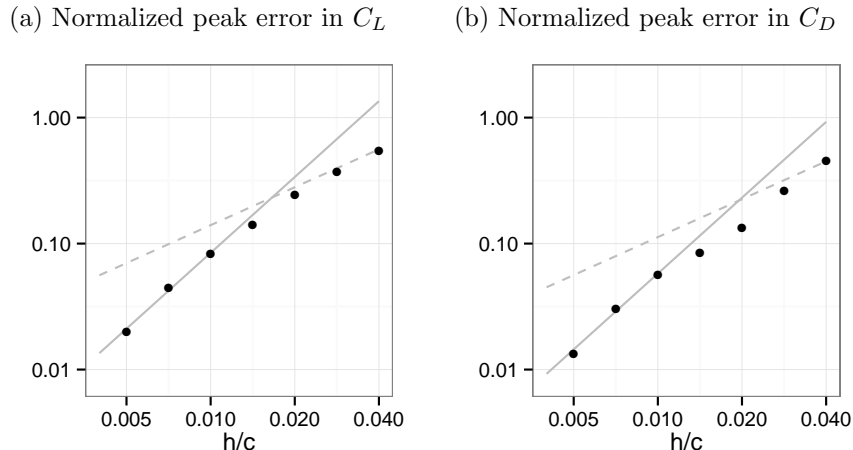


Figure 3.5: Normalized simulation error of the peak values of lift and drag coefficient for the  $\Xi = 1/4$ ,  $Re = 2000$  test case as a function of the grid size  $h$ . The error is computed relative to the values obtained using a fine  $c = 400h$  reference grid. The solid lines indicate second-order convergence with  $h$  and the dashed lines indicate first-order convergence.

of observed flow topology. Next, we compare the model to results from a large range of  $\Xi$ . Finally, in §3.5.3 we present the time-averaged lift and drag generated during the manoeuvre with applications to functional trade-offs in landing birds.

### 3.5.1 Velocity-field results

Figure 3.6 shows vorticity fields arising from the perching manoeuvre, derived from PIV at  $Re = 22000$  and simulations at  $Re = 2000$ . For each  $Re$ , key timesteps from  $\Xi = 1/4$  and  $1/2$  are shown. These particular cases demonstrate key changes to flow topology as  $\Xi$  and  $Re$  are varied. In all cases presented in figure 3.6, positive boundary-layer vorticity separates at the leading edge and rolls up into an LEV. Negative vorticity sheds predominantly from the trailing edge. Between  $t^* = 0.33$  and  $0.83$ , the trailing edge wake appears as a streak of vorticity, connecting with the airfoil at nearly right angles to the chord. At  $t^* = 1$ , a stopping vortex forms at the trailing edge.

Overall the comparison between the high- $Re$  experiments and low- $Re$  two-dimensional simulations is good, with the same magnitudes of vorticity and coherent structures in the wake. However, some of the differences are worth discussion. In figure 3.6, the approximate

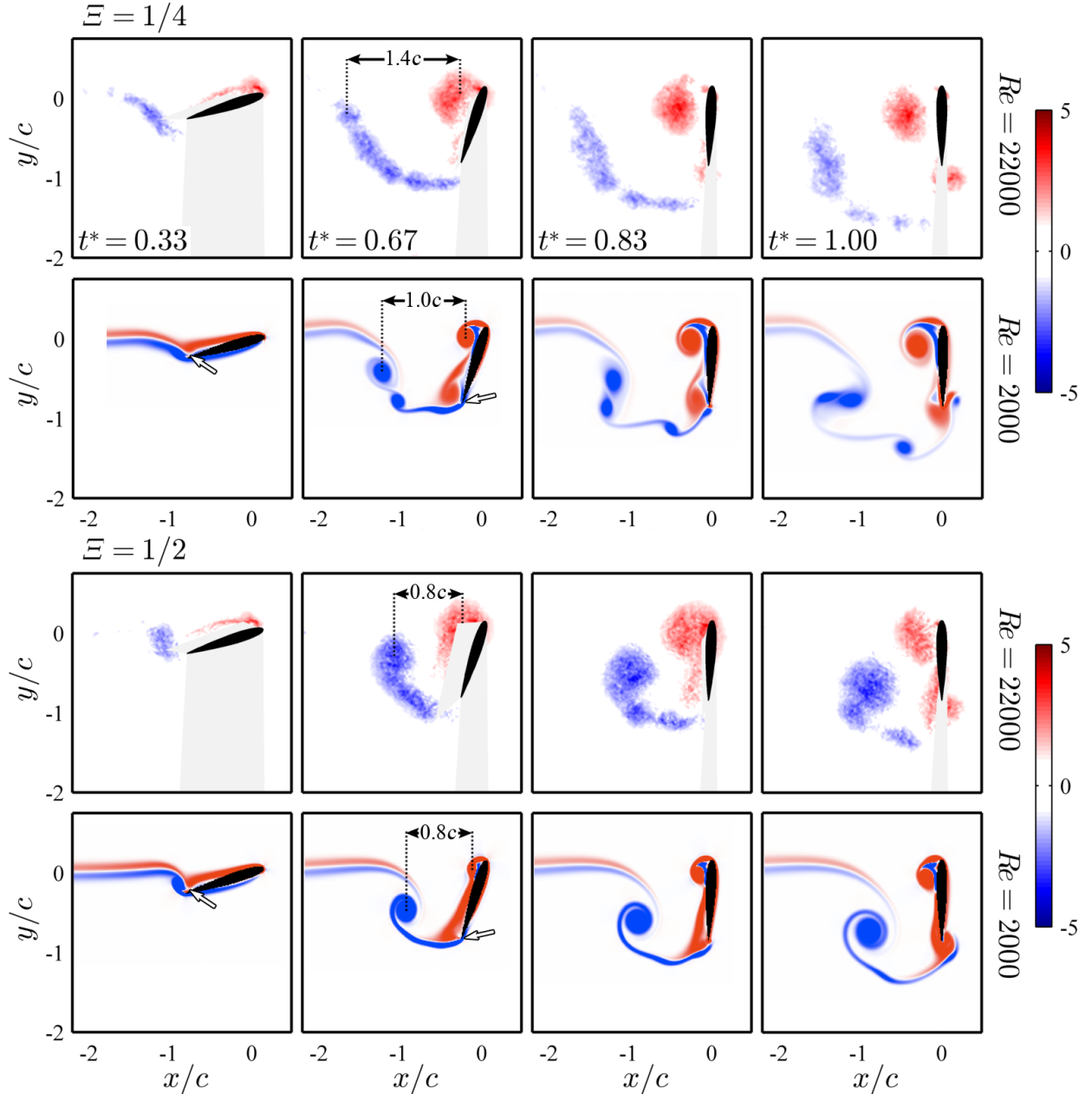


Figure 3.6: PIV measurements ( $Re = 22000$ ) and simulations ( $Re = 2000$ ) of vorticity fields at  $\Xi = 1/4$  (top) and  $\Xi = 1/2$  (bottom). Black dotted lines represent the approximate  $x$ -position of the centre-of-mass of the starting vortex and LEV. In the higher- $Re$   $\Xi = 1/4$  case, the starting vortex trails behind the LEV by a distance of  $x/c = 1.4$  at  $t^* = 0.67$ , whereas the starting vortex trails less than  $x/c = 1.0$  behind the LEV in the other cases. The white arrows, shown at  $Re = 2000$ , point to a stagnation streamline that connects with the airfoil near the trailing edge. At  $t^* = 0.33$ , the stagnation streamline does not lie at the trailing edge. By  $t^* = 0.67$ , the stagnation streamline has moved to the airfoil tip. The reference frame translates such that the origin is fixed at the pivot point. The airfoil is translating in the positive  $x$ -direction. Grey-shaded areas in PIV plots denote regions that have been masked due to shadowing effects or visual obstruction. Vorticity is non-dimensionalized by  $\omega^* = \omega c / U_0$ .

distance between the centre of mass of the LEV and starting vortex are labeled. The LEV remains close to the pivot axis and convects along with the airfoil. For  $\Xi = 1/4$  and  $Re = 22000$ , the starting vortex is approximately 1.4 chord lengths behind the pivot axis by  $t^* = 0.67$ . In contrast, at lower  $Re$  the trailing-edge wake is only  $\sim 1$  chord length from the pivot axis at the same  $\Xi$  and time. The length of the wake is strongly influenced by the positive  $x$ -velocity of the starting vortex induced by the LEV and other wake vortices. For a given strength, a pair of diffuse vortices induce weaker velocities on one another (Saffman & Szeto, 1980; Pierrehumbert, 1980). Figure 3.6 shows that the higher- $Re$  wake vortices and LEV are more diffuse due to turbulent transition and vortex breakdown. Therefore, the difference in wake length is explained by turbulent diffusion of vorticity in the three-dimensional, higher- $Re$  cases, not present in the two-dimensional, lower- $Re$  simulations.

The simulations also clarify some elements of the flow that are obscured in the PIV. A stagnation streamline is observed in the lower- $Re$  cases as the white region between counter-clockwise (red) and clockwise (blue) vorticity near the trailing edge, and is marked with a white arrow at  $t^* = 0.33$  and  $0.67$ . At  $t^* = 0.33$ , this stagnation streamline does not lie at the trailing edge, therefore violating the steady Kutta condition. As discussed by McCroskey (1982), the Kutta condition can break down in highly-unsteady manoeuvres, and abrupt streamline curvature can be present in the trailing-edge region. We find that the Kutta condition appears to be established by  $t^* = 0.67$ . This is consistent with the results of Pitt Ford & Babinsky (2013), who found that the Kutta condition is violated early in an impulsive manoeuvre due to the presence of the starting vortex, but is established as distance from the starting vortex increases.

### 3.5.2 Force history

The forces on the airfoil from the  $Re = 2000$  simulations and  $Re = 22000$  experiments for shape change numbers of  $1/8$ ,  $1/4$  and  $1/2$  are shown in figure 3.7 along with the model predictions from equation (3.18). In all cases, general trends predicted by the analytic

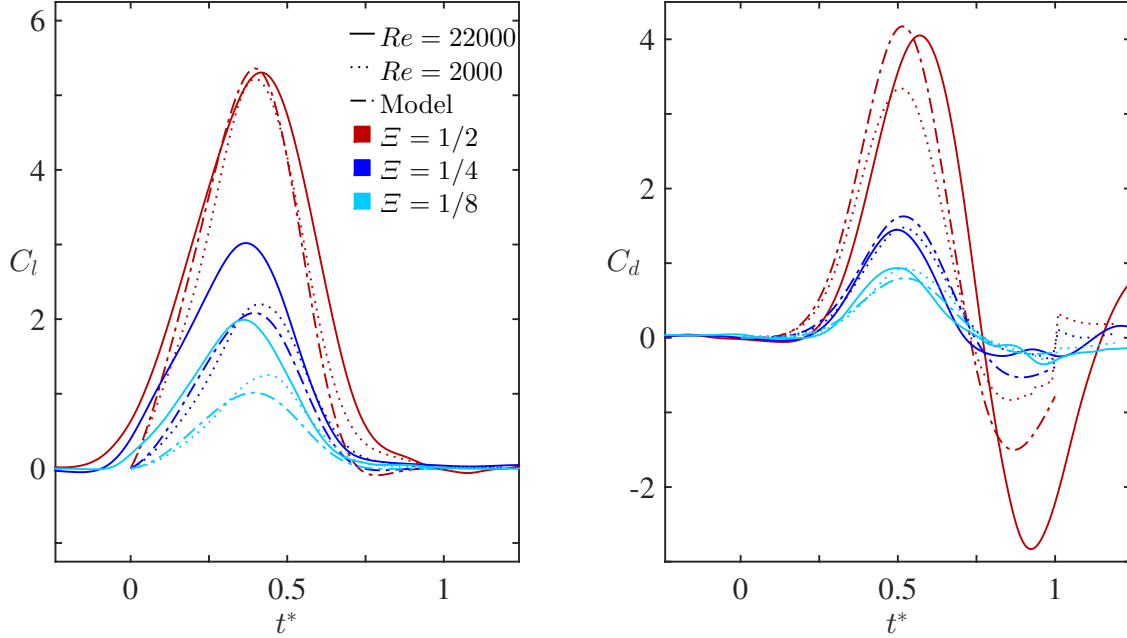


Figure 3.7: A comparison between force results from experiments at  $Re = 22000$  (solid lines), simulations at  $Re = 2000$  (dotted lines), and model predictions (dot-dash lines) for  $1/8 \leq \Xi \leq 1/2$ . The magnitudes and timing of peaks in drag are similar between  $Re$  cases. The timing of peak lift is similar as well. However, magnitudes of lift are similar only in the  $\Xi = 1/2$  case. Model predictions are in close agreement with low- $Re$  force histories.

model are observed: a single lift peak appears close to  $t^* = 0.4$ , a drag peak appears close to  $t^* = 0.5$ , a thrust peak appears late in the manoeuvre, and the magnitudes of all peaks increase with  $\Xi$ .

Overall, the model agrees with lower- $Re$  lift at all  $\Xi$ , suggesting that added-mass forces combined with boundary-layer separation at the leading and trailing edges are the dominant mechanisms of lift generation in lower- $Re$  cases. In the higher- $Re$  cases, however, vortex convection appears to be an important lift-generating mechanism. The vorticity fields shown in figure 3.6 indicate that streamwise vortex convection is greater at  $Re=22000$  than at  $Re=2000$  for  $\Xi = 1/4$ , and the force measurements support this by showing increased lift forces on the airfoil for  $\Xi \leq 1/4$  relative to the simulations and the model. Again, the differences in vortex convection between  $Re$  cases are attributed to turbulent diffusion at higher  $Re$  not present in the simulation resulting in convective force which was neglected in the analytic force model.

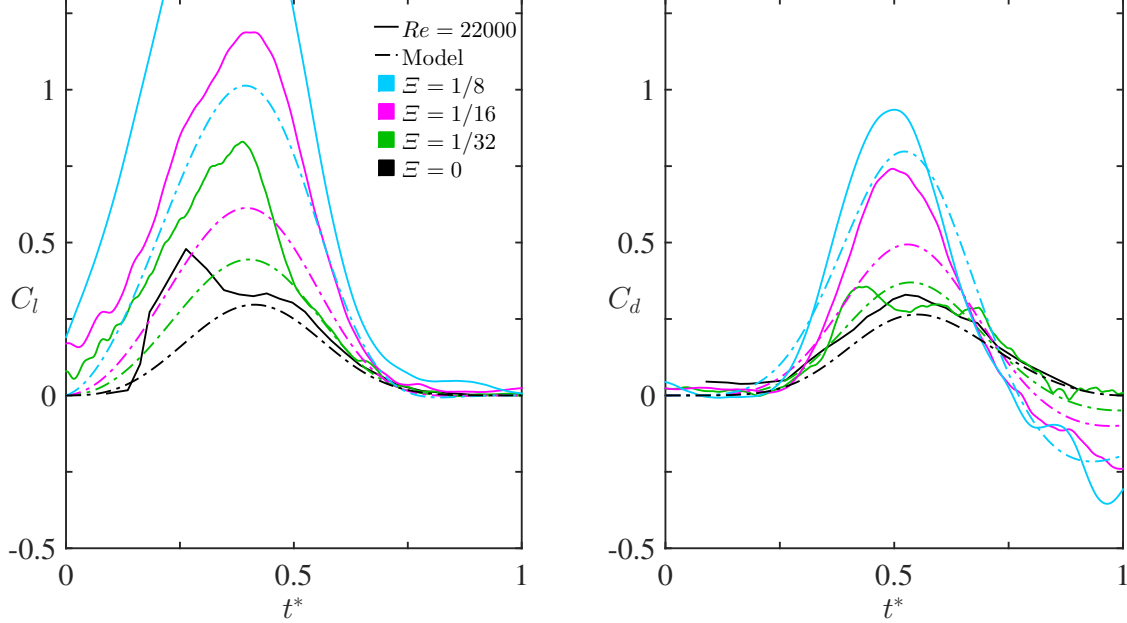


Figure 3.8: Lift and drag coefficients in non-dimensionalized time, plotted for varying  $\Xi$ . The magnitudes of forces increase with  $\Xi$ . At lower  $\Xi$ , results approach quasi-steady predictions (solid black line). The model is overlaid as a dot-dash line. Experiment agrees with the model best at low shape change numbers. The  $\Xi = 0$  case displays a peak lift at pre-stall angles of attack.

Drag histories compare well between the model, simulations, and experiment, particularly in the large drag peak for  $t^* < 0.75$  when added-mass and boundary-layer separation are the dominant mechanism of force generation. From  $0.75 < t^* < 1$ , the measurements and simulations demonstrate the parasitic thrust forces predicted by the added-mass model. The magnitude of the thrust measured for  $\Xi = 1/2$  at higher- $Re$  is larger than that predicted by the combined model, but in line with the thrust predicted by the added-mass estimate in equation (3.3). This indicates the model over-predicts the vortex drag late in the manoeuvre, likely due to interaction effects between the LEV and trailing-edge wake as the airfoil comes to a stop.

Figure 3.7 shows that the accuracy of the model in lift generally increases as  $\Xi$  increases for higher- $Re$ . In §3.2.4, we proposed that the model would also become more accurate in the quasi-steady limit because of the von Kármán vortex street which drives the mean convective force to zero. To assess agreement as  $\Xi \rightarrow 0$ , we performed force measurements

at  $Re = 22000$  with shape change numbers varying from  $1/8$  to  $0$  (figure 3.8). As  $\Xi$  is reduced, measured forces approach quasi-steady values at  $\Xi = 0$ . In the quasi-steady case, note that increased ‘time’ in figure 3.8 corresponds to increased angle of attack via equation (3.6), and the mean forces are shown scaled as in equation (3.3.1).

A continuation of the trends in figure 3.7 are observed in figure 3.8: single peaks in lift, drag and thrust are observed, and the magnitudes of these force peaks continue to decrease as  $\Xi$  decreases. As proposed, the model predicts the quasi-steady measurements well overall as long as the angle of attack is sufficiently large to induce shedding from the leading and trailing edge. The flow remains attached along the suction side of this NACA0012 airfoil section below  $\alpha \sim 10^\circ \rightarrow t^* \sim 0.25$ , enhancing lift well above model predictions. At high angles of attack vortices shed rapidly from the trailing and leading edges, the foil stalls and the lift drops rapidly. Once this rapid shedding begins, the assumptions of the model are satisfied, explaining the better agreement at large  $t^*$ . Similarly, in the  $\Xi = 1/32$  case lift drops off suddenly after reaching its peak and thereafter is closely predicted by the model. The peak and decay in lift for  $\Xi = 1/32$  occur at a higher angle of attack than for  $\Xi = 0$ , which is a manifestation of *dynamic stall*, a phenomenon in which boundary-layer vorticity remains attached beyond static stall angles of attack in pitching airfoils (McCroskey, 1982).

### 3.5.3 Time-averaged forces

Ultimately, the net forces produced over the course of a perching manoeuvre determine if a flying bird or vehicle can safely land. To come to a complete stop, a bird of mass  $m$  flying at an initial horizontal speed  $U_0$  must achieve a time-averaged drag of  $-mU_0/T$  and a time-averaged lift equal to its weight. Birds can and do supply some of the force required to land from their legs at touchdown, but most of the momentum change is generated by aerodynamic means (Provini et al., 2014).

Time-averaged lift and drag for  $0 \leq t^* \leq 1$  are plotted against  $\Xi$  in figure 3.9, with lift and drag coefficients derived from  $Re=2000$  simulations,  $Re=22000$  experiments, and model

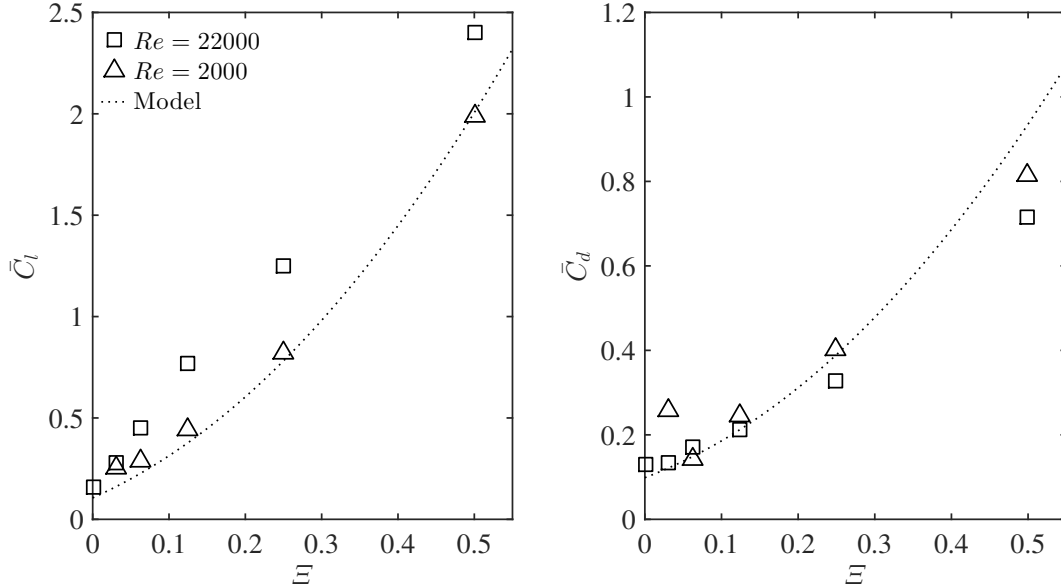


Figure 3.9: Time-averaged lift ( $\bar{C}_l$ ) and drag ( $\bar{C}_d$ ) are always positive and increase with  $\Xi$ . Time-averaged lift is greater than drag at higher shape change numbers due to added-mass forces that contribute to lift but detract from drag (figure 3.2). Time-averaged lift is greater at  $Re = 22000$ , compared to  $Re = 2000$  results and model predictions, due to lift generation from vortex convection present in the higher- $Re$  cases.

predictions. Minimum time-averaged lift and drag coefficients occur at  $\Xi = 0$ . Both lift and drag increase as  $\Xi$  increases, the former more rapidly than the latter, and appear to be unbounded. The minimum lift requirement is proportional to the constant value  $mg$  and can be satisfied by increasing  $\Xi$ . The minimum drag requirement for a full stop is proportional to  $\Xi$ , but since time-averaged drag is predicted to grow as  $\Xi^2$ , this drag criteria can always be met at high  $\Xi$ . This suggests that a bird can simply increase its pitch rate to meet the minimum criteria of a perching manoeuvre, though the costs of fast pitch rates include large torque requirements and high instantaneous loads on the wing.

The model predictions are in close agreement with  $Re=2000$  time-averaged lift. At  $Re = 22000$ , the model is in best agreement with time-averaged lift at  $\Xi = 0$  and  $1/2$ . The maximum error in the predicted lift force occurs at intermediate  $\Xi$  and high- $Re$ , due to neglecting the additional lift mechanism of vortex convection. Model predictions also agree with lower- $Re$  time-averaged drag and are slightly lower than higher- $Re$  results at low  $\Xi$ . The large thrust late in the  $\Xi = 1/2$  experiment reduces the accuracy of the average for that

case.

The model predicts time-averaged lift is much higher than drag at larger  $\Xi$ . This is due to added-mass forces that contribute to lift but detract from drag (figure 3.2). The large differences in integrated lift and drag are amplified by increasing  $Re$  to 22000, due primarily to lift generation from vortex convection. A landing bird may thus generate greater time-averaged lift than drag during a pitch-up manoeuvre. This may help explain why the eagle observed by Carruthers et al. (2007) would consistently approach its perch from below, and exhibited a rapid increase in altitude during its pitch-up phase. As the authors of that study suggested, this may be a means to aid deceleration by transferring kinetic energy to potential energy. However, it may also be that the pitching manoeuvre necessary to generate the required drag produces so much excess lift that an altitude correction is needed to avoid overshooting the perch.

### 3.6 Summary and conclusions

In this study we investigate how high lift and drag can be generated through a controlled pitch-up manoeuvre in the context of bird perching. As a simple perching model, we study the aerodynamics of an airfoil that simultaneously decelerates and pitches to a high angle of attack. The pitch rate and deceleration is parameterized by the *shape change number*,  $\Xi$ , a ratio between the speed of frontal area expansion and initial translational speed. We investigate differences in forces and vorticity fields as shape change number is varied from 0 to 1/2, using force measurements and Particle Image Velocimetry at  $Re = 22000$  and simulations using the Boundary Data Immersion Method at  $Re = 2000$ . A simple analytic model that includes forces from added-mass effects and boundary layer separation at the leading and trailing edges is derived and compared to the measurements.

The simulations and PIV measurements for  $\Xi = 1/4$  and  $\Xi = 1/2$  reveal that the wake of the perching airfoil is dominated by a large leading edge vortex, which remains close

to the foil, and the trailing edge vorticity, which forms a vortex shear layer that rolls up due to Kelvin-Helmholtz instability. The distance between the leading and trailing edge structures is found to be greater than the chord length  $c$  in the  $Re = 22000$  and  $\Xi = 1/4$  case, indicating that vortex convection, neglected in the analytic model, is present in this case. The trailing edge separation point was found to be located on the suction side of the foil initially, only moving to the airfoil tip halfway through the manoeuvre, in agreement with previous experiments.

Both experiments and simulations demonstrated that the lift and drag forces increase super-linearly with  $\Xi$ , achieving peak values of  $C_l = 5.3$  and  $C_d = 4.0$  at  $\Xi = 1/2$ , which are more than an order of magnitude larger than their steady-state peak values. The airfoil is found to experience parasitic thrust at the end of the manoeuvre, but the average drag on the airfoil is always positive and increases with  $\Xi$ .

Analogous to previous rapid area change studies, we find added-mass energy in the perching problem is transferred from the immersed body to the fluid as the frontal area and added-mass increases, producing large lift and small drag. This energy is then recovered by the airfoil late in the manoeuvre in the form of a parasitic thrust, which would be counterproductive to a decelerating manoeuvre. However, a simple model of the vortex force developed in this work predicts that the generation of circulation at the leading and trailing edges dissipates enough energy into the wake to nearly overwhelm this parasitic thrust. We find that the analytic model agrees best with force histories at lower  $Re$ , and with higher- $Re$  cases in the limits of quasi-steady and near-impulsive rotation. In particular, the effects of vortex convection were found to be negligible after stall in near steady-state manoeuvres and were overwhelmed by the production of vorticity in rapid manoeuvres. As these forces can be difficult to estimate in transient flows, the simple kinematic model developed in this work is of great utility.

The large forces observed suggest that pitching rates can be tuned to meet the demanding

lift and drag requirements of perching manoeuvres. Rapid pitch-up may therefore be a means by which a landing bird can maintain lift while quickly braking to a controlled stop and could be effectively applied in manoeuvrable micro-aerial vehicles in the near future.

## Acknowledgements

The authors wish to thank the Natural Sciences and Engineering Research Council of Canada and Alberta Innovates Technology Futures for financial support.

## Chapter 4

# Rapid area change from pitch-up manoeuvres in a small perching bird

### Abstract

Rapid pitch-up during perching manoeuvres has been highlighted as a mechanism to generate large lift and drag, but pitching rates had not been measured in perching manoeuvres. We measure pitch rates in a small, wild bird (*Poecile atricapillus*, Linnaeus 1766). While some perching birds pitch gradually from one stroke to the next, members of *P. atricapillus* pitch up rapidly in one wing stroke. Pitching rates were characterized by the *shape change number*, a metric comparing the rate of frontal area increase to wing acceleration. Members of *P. atricapillus* increase the shape change number during perching to dissipate energy quickly in direct proportion to their total kinetic and potential energy as deceleration begins. The linear relationship between dissipated energy and shape change number is in accordance with simple analytical arguments developed for two-dimensional pitching and decelerating airfoils. Members of *P. atricapillus* use a wing pitch-up manoeuvre during perching to generate large forces and maintain lift and drag through rapid area change. It is suggested that similar pitch-and-decelerate manoeuvres could be used to aid in controlled, precise landings in small manoeuvrable air vehicles.

### 4.1 Introduction

Birds execute such diverse precision manoeuvres as banking, braking, takeoff and landing, in order to navigate dense forests and urban environments. Micro Aerial Vehicles (MAVs) are flying machines of a similar size as small birds, designed to carry out remote sensing tasks in

cluttered airspaces. Mimicking the manoeuvrability of birds, in particular the ability to land on small platforms safely, would allow these vehicles to complete their objectives effectively and efficiently. Though progress has been made in designing perching MAVs (Doyle et al., 2011; Moore et al., 2014; Reich et al., 2009), existing MAVs fall short in achieving the control, speed and precision of natural flyers in landing manoeuvres.

In order to perch, a bird must change its velocity from a cruising speed to a speed close to zero. Birds simultaneously adjust their body and wing posture to become more vertical (Carruthers et al., 2007; Berg & Biewener, 2010; Provini et al., 2014), as horizontal postures reduce drag during cruising flight, but an upright posture facilitates a larger angle of attack for deceleration. Carruthers et al. (2007) noted that the steppe eagle in their study would perform a *rapid pitch-up manoeuvre* during perching sequences, where the angle of attack would change smoothly from near-horizontal to near-vertical. However, steady state aerodynamic analysis predicted a loss of lift at high angles of attack, due to stall effects combined with a reduction of airspeed (Carruthers et al., 2010).

In chapter 3, it was shown that a rapidly-pitching airfoil can achieve large instantaneous and integrated lift and drag, even while decelerating to a stop and pitching to a  $90^\circ$  angle of attack. The pitch rate was parameterized through the shape change number,  $\Xi$ . Forces increased as  $\Xi^2$  through a combination of added-mass energy transfer and vorticity generation. These results suggest that rapid area change through dynamic pitching helps generate the forces required by a perching bird to quickly decelerate and stay aloft.

Though prior works have noted body and wing pitch-up in perching birds (Carruthers et al., 2007; Berg & Biewener, 2010; Provini et al., 2014), no existing studies have reported wing pitching rates in perching birds or demonstrated that the resulting area change is associated with large forces on the body. In this work, we demonstrate fast pitch rates during perching in a small, wild bird (the black-capped chickadee; *Poecile atricapillus* Linnaeus 1766), parameterize these rates in terms of the shape change number, and show that members

of *P. atricapillus* alter their shape change number as the demands of the perching manoeuvre increase, implying that rapid area change through dynamic pitching is a kinematic tool that can be tuned to meet the needs of small landing air vehicles.

#### 4.1.1 Energy dissipation through rapid area change

A change in angle of attack increases the frontal area of a wing. This is an example of *rapid area change*, in which a body in fluid exhibits a rapid expansion or contraction of area while moving. Weymouth & Triantafyllou (2013) showed that rapid area change is characterized by the *shape change number*,

$$\Xi = \frac{V^2}{aL} \quad (4.1)$$

where  $V$  is the outward or inward velocity of area change,  $a$  is the body acceleration and  $L$  is a body length scale. Weymouth & Triantafyllou (2013) demonstrated that by changing the shape change number, the added mass, boundary-layer vorticity and forces on the body can be modified dramatically.

These arguments were extended in chapter 3 to a two-dimensional, rapidly-pitching airfoil decelerating from initial velocity  $U_0$  to a halt. Substitution of kinematic parameters into equation 4.1 revealed that

$$\Xi = \frac{V}{U_0}, \quad (4.2)$$

showing that the shape change number is a measure of the change in frontal area relative to a characteristic change in forward velocity. The parameter  $\Xi$  acts as a measure of the unsteadiness of the problem, similar to the reduced frequency,  $k = \pi fc/U_0$ , where  $f$  is a circular frequency. As in chapter 3,  $\Xi$  is chosen in the present study to emphasize that the manoeuvre of interest is not cyclic and the change in frontal area is fundamental to the perching problem.

As the metric (4.2) was constructed in two dimensions, it requires some modification to be applied to a three-dimensional perching bird. We derive an analogous shape change number

in section 4.3.2, after establishing the characteristic perching behaviour of *P. atricapillus*.

As rapid area change is an effective means to shed energy, we expect a relationship between the shape change number used by these birds and the energetic demands of a perching manoeuvre. Once the bird has perched successfully, its kinetic and gravitational potential energy relative to the perch are both zero. The total change in energy is therefore

$$\Delta E = mg\Delta z + \frac{1}{2}mU_0^2, \quad (4.3)$$

where  $m$  is the bird's mass,  $U_0$  the initial speed of its center of mass (CoM) and  $\Delta z$  the height of its CoM relative to the perch. In principle, any amount of energy could be dissipated with the smallest force, given sufficient time. In practice, however, a bird needs to stay airborne until it lands. Slow deceleration requires longer periods of sustained lift, costing metabolic energy.

Whereas a large bird may sustain lift by gliding, a small bird must flap its wings frequently to stay aloft. Thus, while the eagle observed by Carruthers et al. (2010) could pitch its wings gradually during a perching manoeuvre, a small bird such as *P. atricapillus* has only a short time to pitch before it must flap again to stay airborne. Since rapid area change through pitching is a highly-effective means to quickly shed energy into the surrounding fluid, it would be ideal to shed most of the energy quickly during a rapid pitch-up manoeuvre.

In chapter 3, a perching and decelerating airfoil produced drag as  $D \propto \Xi^2$ , while the translational distance was  $d \propto 1/\Xi$ , due to higher rates of deceleration. The total energy dissipated in such a manoeuvre scales as

$$\Delta E \propto dD \propto \Xi. \quad (4.4)$$

Therefore, we expect the shape change number used by these small birds to increase linearly with the energetic requirements of perching manoeuvres.

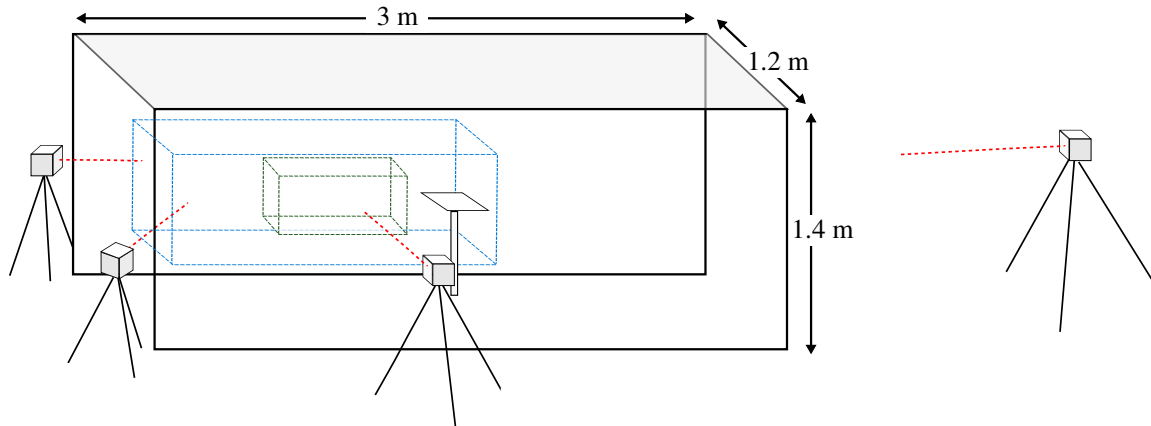


Figure 4.1: A diagram of the setup used in data collection. A feeder was placed at the centre of an enclosure, which was open on two ends. Four cameras were positioned around the enclosure, forming effectively two reconstruction volumes: a smaller control volume for improved resolution of the pitch-up manoeuvre (green) and a larger control volume to capture the entire perching sequence (blue).

## 4.2 Experimental setup

A rectangular enclosure, 3 m long, 1.2 m wide and 1.4 m high was built to encourage birds to approach from a consistent direction (figure 4.1). Two sheets of white polyethylene were attached to the long sides, and two layers of 1" hexagonal wire mesh was fixed on the upper surface. A plastic tray feeder was set 0.9 m above the ground in the centre of the enclosure, and filled with commercially-available birdseed. The two smaller faces on opposite sides of the enclosure were left open. As Green & Cheng (1998) showed that birds will manoeuvre differently to land on a novel perch, filming began 11 days after the feeder was placed and five days after the enclosure was finished, allowing the birds time to acclimate to the setup.

Four Casio EX-ZR700 high-speed cameras were arranged around the enclosure to allow multiple views of perching sequences. The cameras recorded colour images at 480 frames per second in 13-minute intervals while birds flew to the perch freely. Camera frame offsets were calculated based on a flashing LED. Camera positions were calibrated using the Sparse

Bundle Adjustment algorithm packaged in the MATLAB<sup>TM</sup> script *easyWand* (Theriault et al., 2014). A 10 cm calibration wand was waved through the reconstruction volume as a calibration target. The reference frame was aligned to gravity by measuring the acceleration of an object falling through the reconstruction volume. Calibration reconstruction error was estimated as  $\sim 1$  mm, based on the standard deviation of the wand length for all wand images, and synchronization error was estimated as  $\pm 1$  ms.

Perching sequences were digitized manually using the MATLAB<sup>TM</sup> script *DLTdv5*, written by Hedrick (2008). Details of the body parts digitized can be found in figures 4.2B and 4.2C. After digitization, position data was processed using custom MATLAB<sup>TM</sup> scripts (Appendix C). Three-dimensional kinematic position data was smoothed with a second-order low-pass Butterworth filter with 50 Hz cutoff. Velocities and accelerations were computed using two-sided finite difference schemes:

$$\mathbf{u}_i = (\mathbf{x}_{i-2} - 8\mathbf{x}_{i-1} + 8\mathbf{x}_{i+1} - \mathbf{x}_{i+2})/(12\Delta t), \quad (4.5)$$

$$\mathbf{a}_i = (-\mathbf{x}_{i-2} + 16\mathbf{x}_{i-1} - 30\mathbf{x}_i + 16\mathbf{x}_{i+1} - \mathbf{x}_{i+2})/(12\Delta t^2), \quad (4.6)$$

where  $\mathbf{x}$ ,  $\mathbf{u}$  and  $\mathbf{a}$  refer to position, velocity and acceleration vectors, respectively, and  $\Delta t$  is the time increment between frames.

The CoM was taken as the average position between rump tip and beak (figure 4.2). The rump tip was used because it was relatively easy to distinguish in all trials. However, as both rump tip and head are mobile relative to the center of mass, artifacts in acceleration can appear as the bird adjusts its body orientation. To compensate for this somewhat in instantaneous CoM acceleration plots, the true rump location (point 2b in figure 4.2C) was digitized for one trial where it could be distinguished easily. However, movement of the head can still induce artifacts of CoM acceleration, and these will be noted where they appear in the results.

As a metric for the dynamic demands of a perching manoeuvre, we estimated the bird's initial total energy as described in equation 4.3. As the mass of each bird was not measured,

we assumed a simple geometric scaling of body length to mass ( $m \propto L^3$ ). To attain the correct units of mass in equation 4.3,  $L^3$  was multiplied by the arbitrary density 1000 kg/m<sup>3</sup>. Body length was taken as the mean distance between beak and rump tip from the end of the ballistic phase up to the straightening of the arm.  $U_0$  is the average CoM speed from the end of the ballistic phase ( $t_0$ ) to when the wrist is first straightened ( $t_1$ ).  $\Delta z$  is the height of the CoM relative to the perch at  $t_1$ , and  $g$  is the acceleration due to gravity (9.8 m/s<sup>2</sup>).

### 4.3 Results and discussion

Eleven perching sequences were analyzed from two filming sessions five days apart. Based on these sequences, the qualitative perching behaviour is described in section §4.3.1. An extension of the two-dimensional shape change number as presented in chapter 3 to these perching manoeuvres is established in §4.3.2, followed by quantitative kinematic results.

#### 4.3.1 Overview of perching behaviour in *P. atricapillus*

Members of *P. atricapillus* exhibit a *ballistic phase* before beginning rapid deceleration (figure 4.2A; see supplemental video S1 for a representative perching sequence). This phase is characterized by the wings folding tightly around the body and the tail being fully closed, with no apparent active force generation. The bird then enters a *deceleration phase*, characterized by changes in body orientation and wing and tail kinematics. At the start of this deceleration phase, the wings rapidly extend with a forward power stroke. The body also shifts from a horizontal orientation to a more vertical orientation. The tail feathers open as the body posture becomes more vertical. After the first forward stroke, the bird performs a rearward recovery stroke and begins a sequence of between one and four subsequent power-recovery stroke cycles before touchdown (median 2, mean 2.4, standard error 0.28).

Power strokes from the wing cause a torque about the bird's center of mass, as made evident by the rotation of the body into a vertical position following the first power stroke in

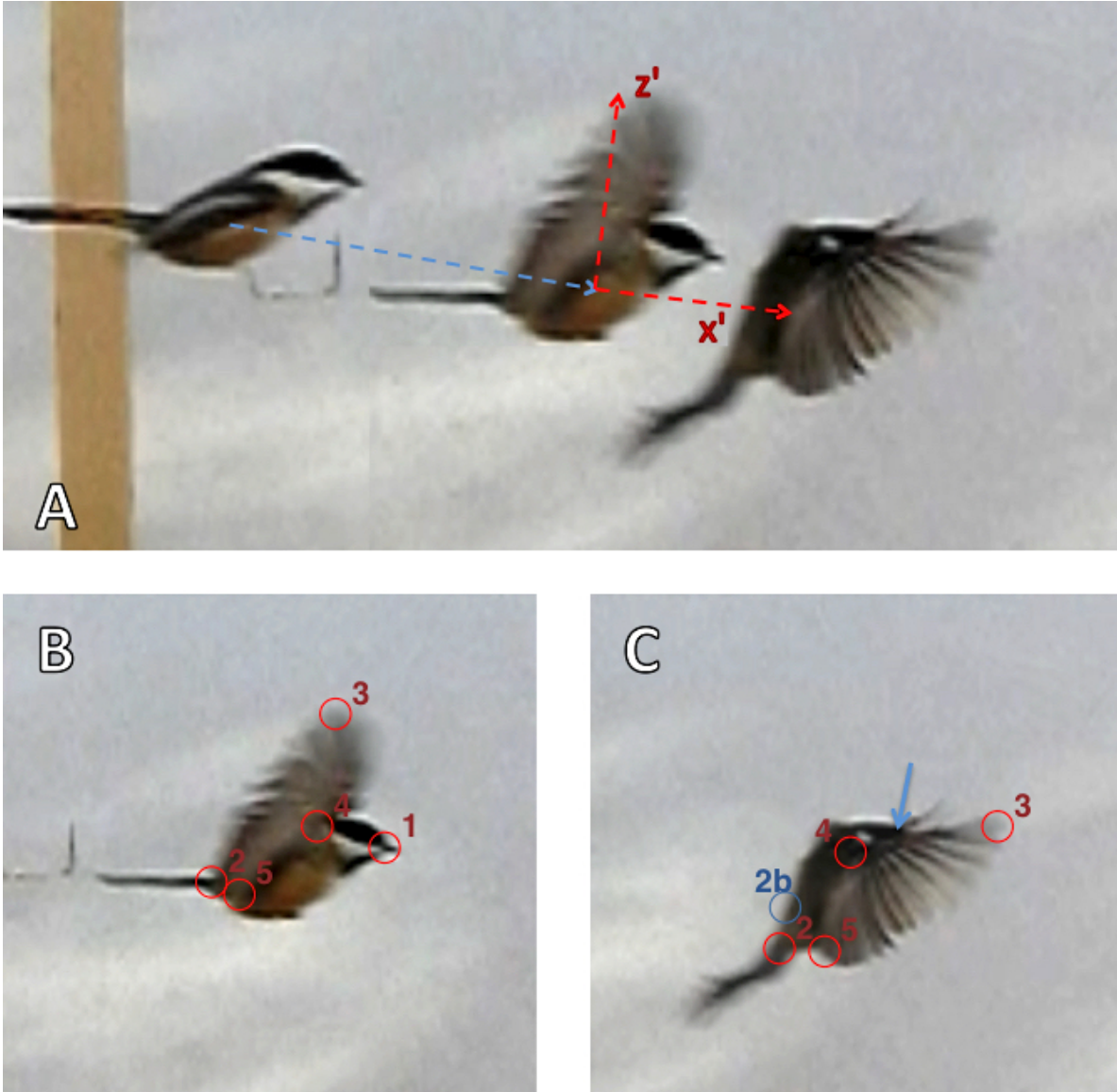


Figure 4.2: **(A)** A compound image from a single perching sequence, showing (left to right) the end of the ballistic phase ( $t_0$ ), the first frame where the wrist straightens ( $t_1$ ), and the final frame before the wrist flexes ( $t_2$ ). The shape change number is calculated between  $t_1$  and  $t_2$ .  $x'$  denotes the displacement vector of the center of mass from  $t_1$  to  $t_2$ . The angle between  $x'$  and the horizontal denotes the angle by which the vertical is rotated to form  $z'$ . Angle of attack is measured relative to the plane whose normal is  $z'$ . ( $t_0 \rightarrow t_1$  : 38 ms.  $t_1 \rightarrow t_2$  : 23 ms.) **(B)** Video still at  $t_1$ . Digitized points are shown as red circles. Points 1 and 2 are the beak and rump tip, respectively. The average of points 1 and 2 was used as a proxy for the CoM. Point 3 is the wing tip, distinguished as the next-to-last primary feather. Points 4 and 5 were used to measure wing chord and angle of attack and are, respectively, the shoulder and the tip of the secondary feather most proximal and posterior to the bird. **(C)** Video still at  $t_2$ . Note the more vertical orientation of both body and wing as compared to **(B)**. The approximate location of the left wrist is shown as a blue arrow. For instantaneous CoM acceleration plots, the true rump location (point 2b) was digitized for one trial where it could be distinguished easily.

the deceleration phase. However, further rotation of the body generally ceases with further forward wing strokes when the tail is fully expanded. This suggests that the tail counteracts the torque produced by the wings while also producing greater drag.

In all observed perching sequences, the birds performed the majority of body reorientation in the first power stroke. This is in contrast to rock pigeons, diamond doves and zebra finches (Berg & Biewener, 2010; Provini et al., 2014), which alter their body angle continuously during the perching sequence. Since this first stroke is associated with the largest change in posture, and therefore presumably the largest pitch rates, we analyzed this stroke in detail to quantify the shape change number and associated forces.

#### 4.3.2 A three-dimensional analogue to the two-dimensional shape change number

Here we extend the two-dimensional shape change number for a pitching and decelerating airfoil (equation 4.1) to an analogous metric relevant to the first perching power stroke described above. During the first stroke, there are three ways in which members of *P. atricapillus* can use control surfaces to change frontal area: (1) extending the wings as they unfold from the body, (2) expanding and pitching the tail and (3) pitching the wings. The latter is most similar to earlier work on two-dimensional pitching airfoils, and so is most amenable to comparative analysis. The first two effects merit future study but are beyond the scope of this thesis.

For *P. atricapillus*, the majority of wing pitching occurs after the wings are fully extended. Once the wing is extended, its change in planform shape appears minimal, fortuitously separating the effects of area change due to pitching from wing expansion. Therefore,  $\Xi$  is calculated from the timestep where the wrist is first straightened ( $t_1$ ) to the timestep immediately before the wrist flexes again ( $t_2$ ; see figure 4.2). The pitch angle to the horizontal is measured at these two points ( $\alpha_1$  and  $\alpha_2$ , respectively). Taking the chord length,  $c$ , and

setting  $T = t_2 - t_1$ , the shape change velocity is then

$$V = \frac{c(\sin \alpha_2 - \sin \alpha_1)}{T}. \quad (4.7)$$

The shape change number requires a characteristic translational velocity change ( $\Delta U$ ). Between  $t_1$  and  $t_2$ , the wing is relatively stiff and performs a sweeping motion that is effectively a solid body rotation about the shoulder. The average chord-wise airspeed across the wing is approximately equal to the speed of the wing, normal to the span, at the midpoint between shoulder and wingtip. We calculate these airspeeds at  $t_1$ ,  $t_2$ , producing  $U_1$  and  $U_2$  respectively. Conveniently, the wings are decelerating from  $t_1$  to  $t_2$  while pitching up, similar to a two-dimensional pitch-and-decelerate manoeuvre. Thus, the deceleration analogous to this two-dimensional case is  $a = \Delta U/T = (U_2 - U_1)/T$ .

Inserting these kinematic values into equation 4.1, we arrive at

$$\Xi = \frac{V[\sin(\alpha_2) - \sin(\alpha_1)]}{\Delta U}. \quad (4.8)$$

Taking the parameters used in chapter 3 ( $\alpha_1 = 0^\circ$ ,  $\alpha_2 = 90^\circ$ ,  $\Delta U = U_0$ ), we recover equation 4.2. Thus, equation 4.8 compares the rate of change of frontal width to the rate of change of sweep velocity in a pitching wing.

Note that equation 4.8 no longer requires a deceleration to a halt, in contrast to equation 4.2. Therefore, it is not necessarily true that  $d \propto 1/\Xi$ , and thus a correction factor is necessary in the relationship between  $\Delta E$  and  $\Xi$ . Assuming constant deceleration from  $U_1$  to  $U_2$ , we can express

$$d = (U_1 + U_2)T/2. \quad (4.9)$$

Using equations 4.7 and 4.8, it can be easily shown that

$$d = \frac{U_1 + U_2}{U_1 - U_2} \frac{c(\sin \alpha_2 - \sin \alpha_1)}{2\Xi}. \quad (4.10)$$

Thus, the relationship between  $\Delta E$  and  $\Xi$  becomes

$$\Delta E \propto \left( \frac{U_1 + U_2}{U_1 - U_2} c(\sin \alpha_2 - \sin \alpha_1) \right) \Xi. \quad (4.11)$$

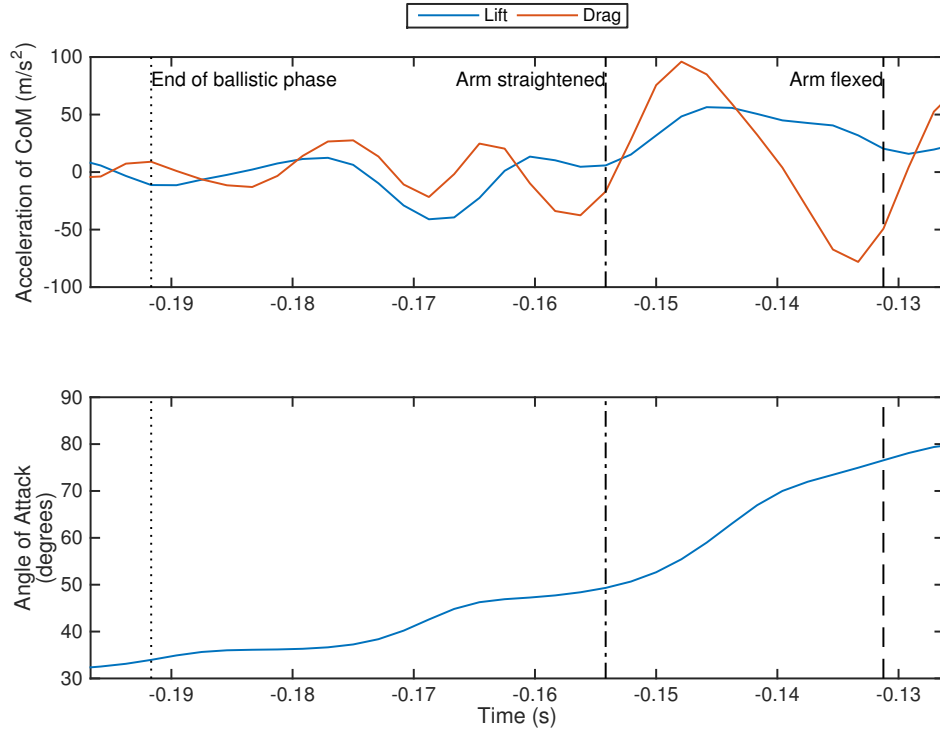


Figure 4.3: Members of *P. atricapillus* exhibit large center-of-mass accelerations along with a rapid increase in angle of attack from the moment when the wing wrist is straightened to the moment where it is bent again. The peak thrust near the point of arm flexion is likely an artifact due to head movement relative to the center of mass.

The relation 4.11 amplifies any error associated with digitization, as kinematic parameters are multiplied. Therefore, both equation 4.4 and 4.11 will be tested.

#### 4.3.3 Rapid pitch-up manoeuvres and area change to increase force production

Figure 4.3 shows the instantaneous lift and drag, divided by mass, for a representative trial, as determined by the acceleration of the CoM. Vertical lines denote the end of the ballistic phase, the straightening of the wrist, and the point where the wrist is bent again. The greatest pitching occurs from the moment where the wrist is straightened to the moment where the wrist is bent. A large peak in lift and drag occurs at the onset of the pitch-up manoeuvre. The peak in drag is followed by a peak thrust; this is likely an artifact of our definition of CoM, due to the forward rotation of the body relative to the head. Therefore, the actual acceleration due to drag on the body is likely larger than the values shown here.

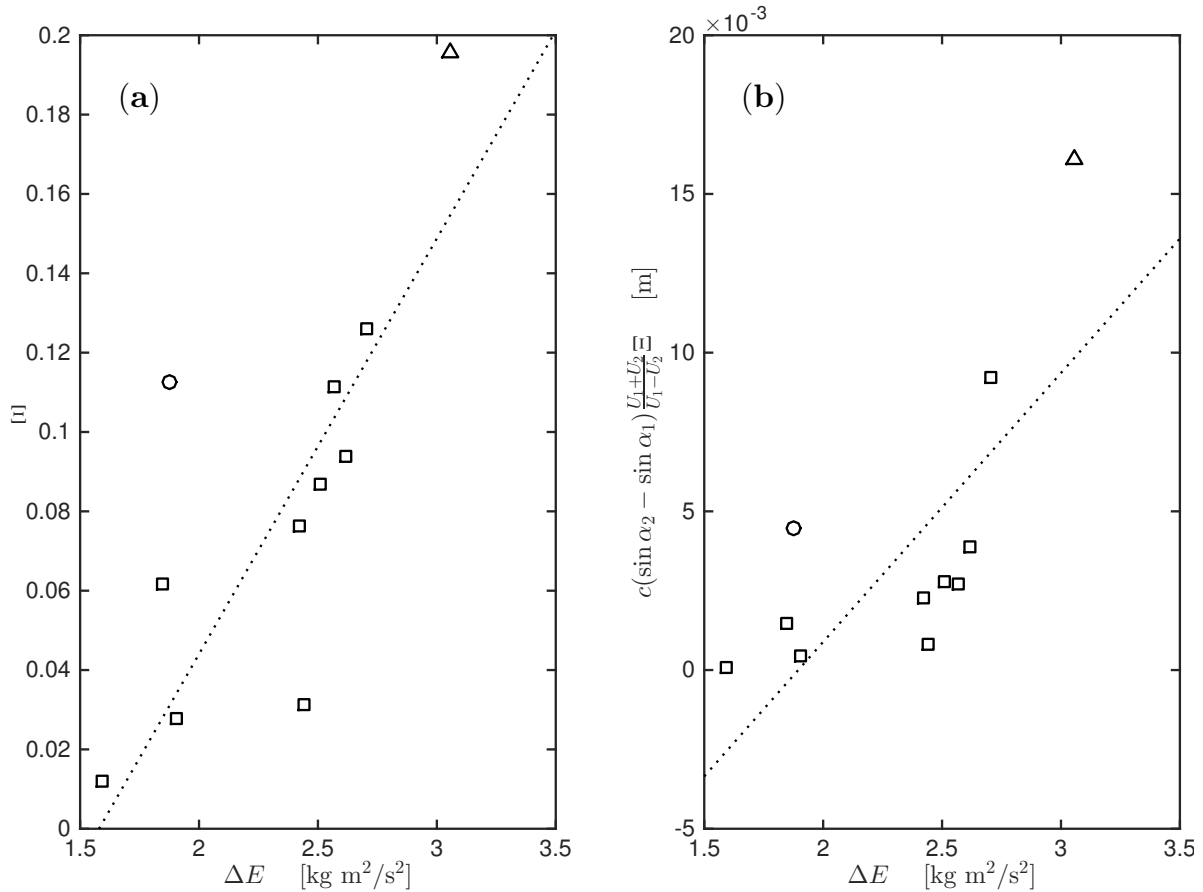


Figure 4.4: Members of *P. atricapillus* pitch their wings at a higher shape change number as the total energetic requirements of the perching manoeuvre increase. (a) The linear trend observed here is consistent with predictions based on analytic force models of pitching and decelerating airfoils, without corrections for the new shape change metric. The trial denoted with a circle is an outlier from the central tendency, exhibiting a much higher shape change number given its initial energy. The bird in this trial exhibited different landing patterns than the others. Excluding this outlier, the least-squares residual is shown as a dotted line ( $R^2 = 0.73$ ,  $p = 0.002$ ). The triangle represents the single trial where the wingtip could not be discerned for a minimum two frames after the pitch-up manoeuvre; in that case, the shape change number was calculated up to the last frame where wing speed could be determined according to equation 4.5. (b) Shape change number, when multiplied by a correction factor for the new three-dimensional metric (equation 4.11), continues to display a strong linear relationship with energetic requirements ( $R^2 = 0.58$ ;  $p = 0.01$ ). Multiplicity of kinematic parameters amplifies any digitization error, and is thought responsible for the slightly reduced  $R^2$  value in this case.

Figure 4.4a plots the shape change number according to equation 4.8 for individual perching sequences against each bird's total initial potential and kinetic energy. Shape change number varies from 0.01 to 0.20, within the range of those tested in chapter 3. Shape change number increases with initial kinematic energy, supporting the hypothesis that pitch rates are tuned by small birds to the energetic demands of the perching manoeuvre. Using all trials, the  $R^2$  value of the linear least-squares fit is 0.55 ( $p = 0.004$  for the linear model). Of note is a single trial, denoted by a circle in figure 4.4, which exhibits a much higher shape change number given its initial energy, as compared to the others. In this sequence, unlike the others, the bird slowed to a near halt before landing, and required an extra lunge near the perch to achieve touchdown (see supplementary video S2). It may be that this individual overestimated its energy requirements and used a higher shape change number than needed to land smoothly. Excluding this outlier, the  $R^2$  value is 0.71. This corresponds to  $p = 0.002$  under the linear model hypothesis, supporting the relationship developed in equation 4.4.

In §4.3.2, it was noted that the new three-dimensional shape change metric does not necessarily require  $d \propto 1/\Xi$ , and therefore a correction factor is necessary in the relationship between  $\Xi$  and  $\Delta E$ .  $\Xi$ , multiplied by this correction factor, is plotted in figure 4.4b. The trend remains linear, however larger scatter is observed due to the amplification of measurement error. Excluding the outlier as before, the  $R^2$  value is 0.58 with  $p = 0.01$  under the linear hypothesis.

The strong dependence of shape change number on total energy change, rather than total power, is due to the constraints of flight and thus perching at small sizes. Because small birds must flap frequently to stay airborne, members of *P. atricapillus* perform a pitch-up manoeuvre during a power stroke rather than through a gliding approach. Performing the majority of pitch-up at the beginning of the deceleration phase immediately positions the bird in the correct posture for landing while dissipating a large amount of energy, facilitating slower speeds as the bird approaches the perch and precise control becomes more vital. This

allows for remarkable performance, enabling these birds to decelerate on average from 47 body lengths per second to a halt in less than 0.3 seconds.

The acceleration artifacts from head rotation and the difficulty in digitizing the true rump in all trials means that no direct comparison between shape change number and acceleration can be made during the pitch-up manoeuvre for this dataset. Future work could achieve better CoM estimates using markers on captive birds, but this is not an option for wild specimens. While figure 4.4 shows a strong relationship between shape change number and energetic demands, the exact nature of this relationship should be taken cautiously. Mass could only be estimated as a proportion to length, and any error in estimating this length is compounded by the factor  $L^3$ . Future studies could implement a weight-scale into the perch itself, enabling accurate measurements of mass once the bird has landed. This would then allow a better experimental measure of the exact relationship between area change and energetic demands.

The large peaks in lift and drag at the onset of pitching and the choice of larger pitch rates for more energetic perching manoeuvres support the hypothesis that members of *P. atricapillus* use dynamic pitching to induce large forces for a successful landing. Though high angles of attack can be associated with a loss of lift and control in steady state flight, members of *P. atricapillus* appear to use a rapid pitch-up manoeuvre to simultaneously reorient the body to the correct landing posture while dissipating large amounts of energy dynamically.

## 4.4 Conclusions

Body reorientation is unavoidable for a bird transitioning from a horizontal cruising posture to an upright landing posture, and is often associated with increases in wing angles of attack. Unlike some birds, which pitch gradually from one stroke to the next, members of *P. atricapillus* pitch their wings up rapidly in one stroke. Pitching rates in perching birds

were characterized by the *shape change number*, a metric comparing the rate of frontal area increase to wing acceleration. Chapter 3 revealed that forces dramatically increase with the shape change number. Members of *P. atricapillus* were shown to exhibit large forces at the onset of rapid pitch-up. These birds increase the shape change number during perching manoeuvres to dissipate energy quickly as the total energy of the manoeuvre increases. Further, the relationship between shape change number and energetic requirements of perching is linear, in accordance with simple analytical arguments developed for two-dimensional pitching and decelerating airfoils. Members of *P. atricapillus* use a pitch-up manoeuvre during perching to dissipate energy quickly and maintain lift and drag through rapid area change. It is speculated that similar pitch-and-decelerate manoeuvres could be used to aid in controlled, precise landings in small manoeuvrable air vehicles.

## Acknowledgements

The authors wish to thank the Natural Sciences and Engineering Research Council of Canada and Alberta Innovates Technology Futures for financial support.

# Chapter 5

## Synthesis and conclusions

In chapter 3, the physics of a pitch-and-decelerate manoeuvre was investigated. A metric for rapid area change, the *shape change number*,  $\Xi$ , was applied to the manoeuvre of interest. A simple analytical model was synthesized and presented, and considered force generation through rapid shedding of boundary-layer vorticity and added-mass effects. The model agreed well with laboratory experiments at  $Re = 22\,000$  and simulations at  $Re = 2000$ . The net drag was shown to increase in proportion to  $\Xi^2$ , as predicted by the analytical model.

In chapter 4, the physics developed in chapter 3 was applied to a small, wild bird (the black-capped chickadee: *P. atricapillus*). These small birds were observed to pitch their bodies and wings during the first power stroke during deceleration. A three-dimensional analogue to the two-dimensional shape change number presented in chapter 3 was developed and was used to parameterize the rate of frontal area change due to wing pitch-up. It was revealed that black-capped chickadees used  $1/10 < \Xi < 1/5$ , within the parameter range of chapter 3. As  $\Xi \propto 1/d$ , where  $d$  is the total distance traveled during pitch up, energetic dissipation during rapid pitch-up was predicted to scale as  $\Delta E \propto \Xi$ . It was shown that as the energetic requirements of the perching manoeuvre increase, so too does the shape change number chosen by the bird, in accordance with these predictions. Inspired by this behaviour, it is speculated that a simple MAV perching algorithm could start by estimating the initial energy relative to the perch and initiating a proportional rapid pitch-up manoeuvre.

The success of the model in describing observed forces in an airfoil and in predicting aspects of perching behaviour in chickadees suggests these small birds use a combination of rapid boundary-layer separation and added-mass effects to achieve rapid energy dissipation during perching. A rapid pitch-up manoeuvre could be applied to dissipate energy in a



Figure 5.1: A black-capped chickadee showing covert deflection during a perching power stroke. This is indicative of a stalled state near the leading edge. It is unknown whether covert deflection plays a role in stabilizing the LEV.

perching MAV, and the analytical model developed in chapter 3 may be used as a first-order approximation for predicting the forces and pitch rates to use in landing.

Though pitch-up was highlighted in this thesis, it is not the only way for birds to change frontal area during perching. Several authors have noted wing planform shape change during landing manoeuvres (Carruthers et al., 2007; Berg & Biewener, 2010). These changes in shape may be amenable to rapid area change arguments. For instance, prior to beginning the pitch-up phase, the chickadees in chapter 4 fully extended their wings from a tucked-in posture. The change in frontal area would rapidly increase added mass, generating drag. In contrast to the pitch-and-decelerate manoeuvre, a parasitic thrust would *not* be expected from this change in area, as the wings do not decelerate until the end of the power stroke. The aerodynamics of planform shape change in perching could be investigated using a similar method to Wibawa et al. (2012), by increasing the submerged span of a surface-piercing airfoil. This form of rapid area change may be an important aspect of bird perching, and merits further investigation to provide fresh inspiration for wing-morphing autonomous aircraft.

Bird wings can exhibit dynamic changes not only in area, but also in surface roughness. Particularly relevant to perching, Carruthers et al. (2007, 2010) noted the upper- and underwing covert feathers deploy during pitch-up manoeuvres, and suggested that underwing coverts act as leading-edge flaps, stabilizing pitch-up at high  $\alpha$  and promoting the formation

of the LEV. Underwing covert deflection was not observed during perching in chickadees, however upperwing covert deflection was observed (figure 5.1). Beyond indicating a stalled state on the wing, the deflection of these feathers may modify flow near the wing. Experimental results in chapter 3 suggested that turbulent diffusion of vortices can ultimately lead to larger lift coefficients. Leading-edge serrations can enhance mixing and thus vortex diffusivity, and higher-amplitude leading-edge protrusions enhance lift in a post-stall regime (Hansen et al., 2011). Thus, the deflecting covert feathers may be a passive mechanism to enhance lift. To investigate this, airfoils with leading-edge serrations, or real wings from birds collected post-mortem, could be used in pitch-and-decelerate manoeuvres. In the latter scenario, force production in cases where the feathers are glued down so they cannot deflect can be compared to cases where the feathers are allowed to deflect, and the aerodynamic influence of wing feathers during perching could be directly established.

As perching birds range in mass from less than 10 g to over 2 kg, it is important to consider how a bird's size can impact its perching strategy. In chapter 2, a reduction in perching stroke frequency for increasing mass was observed. In chapter 4, the use of a pitch-up manoeuvre during a power stroke as opposed to a gliding approach was tied to the requirements of higher stroke frequency in the smaller bird. An aerodynamic mechanism as to why larger birds differ in their approach to pitch-up has not been established, and there may be a critical size at which a gliding-type pitch-up approach becomes more advantageous. Determining this criterion would require a sampling of perching manoeuvres across a larger size range of birds than is currently available in the literature. It would also require extending the laboratory experiments to a larger range of  $Re$ . While  $Re \leq 22\,000$  sampled in chapter 3 are relevant to small birds, the birds that exhibit gliding-type perching all operate at  $Re > 100\,000$ .

Combining a power stroke with pitch-up may attenuate the added-mass thrust observed at high angles of attack in chapter 3. The forward sweep of the wing during pitch-up causes

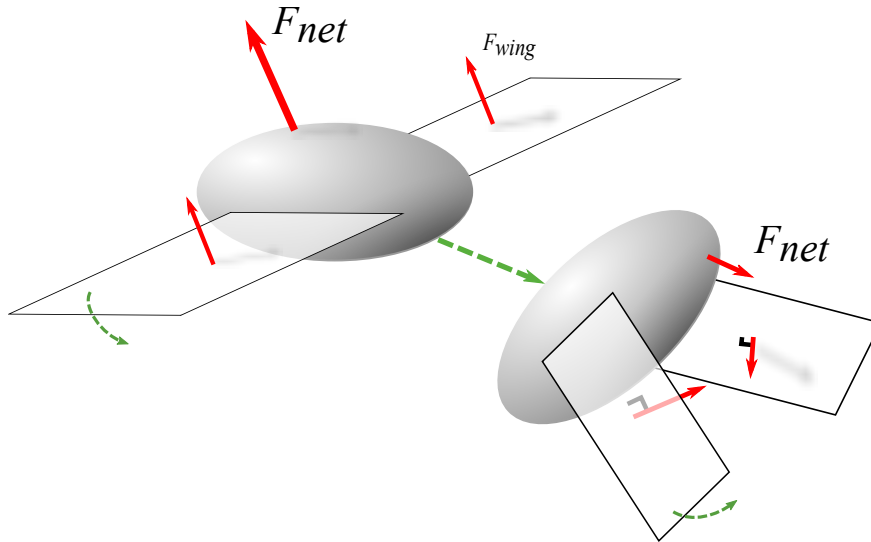


Figure 5.2: For a small bird at the onset of the pitch-up phase, the sweep angle is approximately  $90^\circ$  to the translation direction. Net forces generate lift and drag. At the end of the pitch-up phase, sweep angle is close to  $180^\circ$ . Each wing may generate a parasitic thrust, as observed in chapter 3 at high angles of attack and low speed, but this thrust is largely canceled due to wing orientation.

any thrust forces from opposite wings to cancel (figure 5.2). The fact that large birds do not exhibit sweep during pitch-up and maintain a perpendicular sweep angle suggests one of four options: (1) large birds use an as-yet unknown mechanism to counteract this thrust, (2) large birds exhibit pitch-up at low shape change numbers with little thrust, (3) thrust is mitigated at higher  $Re$ , in contrast to experimental results suggesting forward thrust increases with  $Re$ , or (4) the actual thrust on bird wings is small or non-existent.

The thrust observed in experiments may result from coupled acceleration and pitch rates. It is not known how force history might change if translational acceleration were unconstrained, however Weymouth & Triantafyllou (2013) found an increase in the performance of a squid-like rocket when acceleration was decoupled from area change. Computational approaches can be easily modified to relax the constraint of prescribed acceleration, while laboratory investigations would require a force-feedback system. Of note, the analytical model presented in chapter 2 depends only on *instantaneous* kinematics. It can therefore be reapplied to a decoupled system, and the resulting translational speed can be solved through a system of differential equations. If parasitic thrust disappears with a decoupling

of pitch and deceleration, this would explain why large birds do not sweep their wings during pitch-up manoeuvres, as maintaining a wing area perpendicular to the translational direction would maximize drag. The sweep observed in smaller birds could then be explained by the requirement of frequent power strokes to maintain lift.

Birds reorient to a more vertical body posture during perching. This change in posture is necessary because birds rest on their hind limbs and cruise with their bodies oriented horizontally. As angle of attack often increases along with body angle (Berg & Biewener, 2010), a rapid pitching of the wings is a useful way to dissipate energy while rotating the body to the proper orientation for landing. However, in MAVs not constrained to a bird's body plan, a change in posture may be unnecessary and more efficient or effective means of deceleration may be possible. Other means of deceleration, such as wing morphing, spoilers and forward power strokes, should be compared to the pitch-up manoeuvre to fully assess utility in MAVs.

In this thesis, the unsteady aerodynamics of bird flight was explored to understand the biological system and to apply the learned principles to MAVs. Perching, a complex manoeuvre, was quantified in simple physical terms that can be applied to man-made machines. This is one of numerous steps in designing MAVs with better manoeuvrability than ever before. Many avenues remain to be investigated, as birds are remarkable flyers and still have much to teach us. This thesis is a small glimpse into the physical world of birds, full of possibilities that we have just begun to explore.

# Appendix A

## A derivation of the added-mass force in a pitching and translating plate

### A.1 Motivating problem

Consider a flat airfoil constrained to two degrees of freedom in an inviscid fluid. It may pivot about some arbitrary pivot position along its length ( $x_p$ ) at a rate  $\alpha(t)$ , and its pivot point may translate along a straight line at a speed  $U(t)$ . The forces acting on the airfoil are a function of the time history of the generation and propagation of vortical structures in the wake and the instantaneous acceleration. It is difficult or impossible describe the former relations generally, but the latter is not so difficult.

The inviscid contribution to the forces due to the acceleration of the body is known as the *added-mass* force, so called because this force resists the body's acceleration, and so appears as an apparent increase in the body's mass. In a potential flow, this force is due entirely to the unsteady boundary conditions at the body's surface. Explicitly, a velocity potential  $\phi$  is determined by solving the continuity equation

$$\nabla^2 \phi = 0 \tag{A.1}$$

with two boundary conditions (Katz & Plotkin, 2001). First, the far field sees no perturbation from the body,

$$\lim_{r \rightarrow \infty} \nabla \phi = U_\infty. \tag{A.2}$$

Second, the body has an impermeable boundary

$$(\nabla \phi - \mathbf{v}_b) \cdot \hat{\mathbf{n}} = 0, \tag{A.3}$$

with  $\mathbf{v}_b$  describing the instantaneous rotation and velocity of the body, and  $\hat{\mathbf{n}}$  is a body normal vector. Ultimately, the added-mass force originates from the final boundary condition (A.3) as it changes in time. Other circulatory forces arise from other prescribed conditions (*e.g.* the Kutta condition). Due to the linearity of Laplace’s equation, and thus potential flow solutions, the potential flow solution can be split into a portion owing to the translating body ( $\phi_B$ ) and a portion owing to the wake ( $\phi_W$ ) as (Katz & Plotkin, 2001)

$$\phi = \phi_B + \phi_W. \quad (\text{A.4})$$

Since  $\phi_B$  dictates the added-mass forces, we can determine non-circulatory forces independently of circulatory effects.  $\phi_B$  is found by solving the Neumann boundary value problem formed from equation (A.1) along with the boundary conditions (A.2) and (A.3).

Of note is that equation (A.1) is independent of time, as is boundary condition (A.2). Since (A.3) requires the *instantaneous* velocity of the body, solutions to the Neumann problem at each timestep are the same as the steady-state solution (with a constant velocity corresponding to the instantaneous velocity)<sup>1</sup>. Therefore, we need only solve the steady state solution at each timestep to yield the unsteady potential (Katz & Plotkin, 2001).

To calculate the pressure gradient, the unsteady Bernoulli equation may be used,

$$\frac{\Delta p}{\rho} = \frac{1}{2}(q_2^2 - q_1^2) - (\mathbf{V}_0 + \boldsymbol{\Omega} \times \mathbf{r}) \cdot (\nabla \phi_2 - \nabla \phi_1) + \frac{\partial}{\partial t}(\phi_2 - \phi_1), \quad (\text{A.5})$$

where 2 and 1 refer to points along the streamline of interest. To calculate the force on the airfoil, we need only determine the potential at the airfoil surface and integrate using equation (A.5). The potential consists of a portion owing to translation and reorientation of the airfoil, as well as a portion owing to the rapid rotation of the airfoil. Due to linearity, these potentials may be superimposed to achieve the final potential.

Joukowski transforms map potentials for various cylinders in the (mapping)  $\zeta$  plane to

---

<sup>1</sup>Physically, this comes about because of the incompressibility assumption in potential flow. Information about the boundary is transmitted instantaneously to every part of the fluid. In effect, it takes the flowfield an infinitesimal time to reach steady state

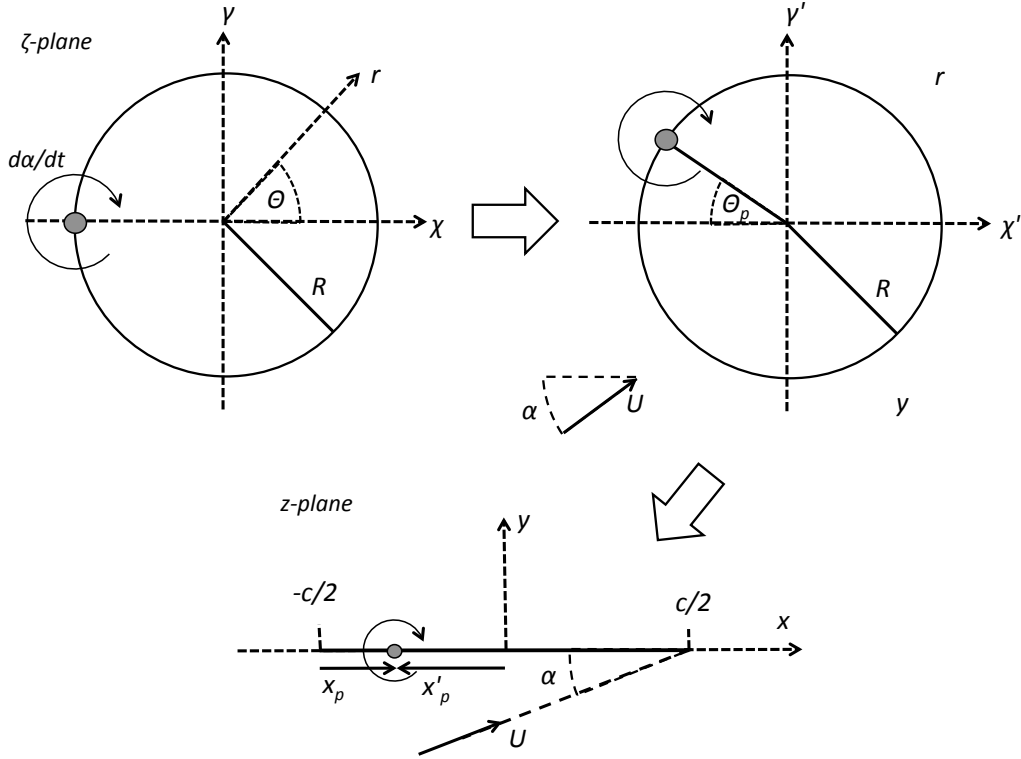


Figure A.1: The conformal maps used in this derivation. We start with a circle in the  $\zeta$  plane rotating about its edge. We then rotate the cylinder by  $\theta_p$ , and impose a free-stream velocity  $U$ . Finally, we map this back to the  $z$  plane using the Joukowski Transform (Eq. A.7)

airfoils in the (physical)  $z$  plane. These transforms may be written generally as

$$z = x + iy, \quad \zeta = \chi + i\gamma; \quad (\text{A.6})$$

$$z = \frac{1}{n} \left( \zeta + \frac{R^2}{\zeta} \right), \quad (\text{A.7})$$

where  $R$  is a unit length in the  $\zeta$  plane, and  $n$  is some prescribed integer. A circle of radius  $R$  centered at the origin will map to an infinitesimally thin, flat airfoil (figure A.1).

Care must be taken to choose the appropriate map, depending on the problem of interest. In particular, consider how the coordinates in the physical plane  $(x, y)$  relate to the

coordinates in the mapping plane  $(\chi, \gamma)$ . Defining  $\zeta\bar{\zeta} \equiv r^2$ , we have

$$z = \frac{1}{n} \left( \frac{\zeta r^2 + \bar{\zeta} R^2}{r^2} \right); \quad (\text{A.8})$$

$$= \frac{1}{n} \left( \frac{(\chi + i\gamma)r^2 + (\chi - i\gamma)R^2}{r^2} \right); \quad (\text{A.9})$$

$$x = \frac{1}{n} \chi \frac{r^2 + R^2}{r^2} \quad , \quad y = \frac{1}{n} \gamma \frac{r^2 - R^2}{r^2}. \quad (\text{A.10})$$

In the far field,  $r \gg R$  and  $(x, y) = \frac{1}{n}(\chi, \gamma)$ . In the near field,  $r \sim R$  and  $(x, y) = \frac{2}{n}(\chi, 0)$ .

This has subtle consequences when transforming velocities from the mapping plane to the physical plane. If we define velocities in the far field (e.g.  $U_\infty$ ) we should choose  $n = 1$  to preserve length. If we instead define velocities in the near field (e.g. rotational velocities as  $\dot{\alpha}R$ ), we should choose  $n = 2$  to preserve length.

Therefore, for the present derivation, we use the following maps:

$$z = \left( \zeta + \frac{R^2}{\zeta} \right) \quad (\text{Everywhere, for translations}), \quad (\text{A.11})$$

$$x = \frac{c}{2} \cos \theta \quad , \quad R = c/4 \quad (\text{On surface, for translations}), \quad (\text{A.12})$$

$$z = \frac{1}{2} \left( \zeta + \frac{R^2}{\zeta} \right) \quad (\text{Everywhere, for rotations}), \quad (\text{A.13})$$

$$x = \frac{c}{2} \cos \theta \quad , \quad R = c/2 \quad (\text{On surface, for rotations}). \quad (\text{A.14})$$

The polar coordinates  $\theta$  and  $r$  will be used in the  $\zeta$  plane, for convenience (see figure A.1).

## A.2 Added-mass force of a slowly-rotating thin airfoil

In this section, the added-mass force is derived for an airfoil accelerating in an otherwise calm fluid. We allow the airfoil to ‘*slowly rotate*’, such that the far-field ambient flow is unidirectional in the airfoil-fixed frame of reference. We leave derivation of the potential due to rapid rotation until §A.3.

For a cylinder at rest in an ambient of uniform flow ( $\mathbf{U}_\infty = U[\cos(\alpha)\hat{\mathbf{x}} + \sin(\alpha)\hat{\mathbf{y}}]$ ), the potential function is,

$$\phi(r, \theta) = U \left( r + \frac{R^2}{r} \right) \cos(\theta - \alpha). \quad (\text{A.15})$$

This yields the tangential and radial velocities,

$$\mathbf{V}_\theta = -U\left(1 + \frac{R^2}{r^2}\right) \sin(\theta - \alpha) \hat{\theta}, \quad (\text{A.16})$$

$$\mathbf{V}_r = U\left(1 - \frac{R^2}{r^2}\right) \cos(\theta - \alpha) \hat{\mathbf{r}}. \quad (\text{A.17})$$

The impermeable boundary condition (A.3) is satisfied in equation (A.17) at  $r = R$ . Additionally, the far field boundary condition (A.2) is met as  $\mathbf{V} \rightarrow \mathbf{U}_\infty$  with  $r \rightarrow \infty$ .

To determine the forces acting on the body, we need only about the potential at the airfoil's surface ( $x$ ). Using the mapping function (A.12), this potential is

$$\phi_a(x) = \frac{Uc}{2} \left( \frac{2x}{c} \cos \alpha \pm \sin \alpha \sqrt{1 - (2x/c)^2} \right), \quad (\text{A.18})$$

where  $x$  is the position along the chord ( $x = 0$  is the half chord). The positive square root refers to the top surface and the negative square root to the bottom surface.

In the unsteady case,  $\alpha$  and  $U$  are time-dependent. However, equation (A.18) satisfies the boundary conditions at each instant, even when these parameters are time-dependent (ignoring the rotational speed). Thus, equation (A.18) is the unsteady surface potential for an accelerating and slowly-rotating flat airfoil.

Equation (A.5) may be used to calculate the pressure gradient between the top and bottom surfaces. We will consider only chord-normal forces and neglect any chord-parallel forces, which are likely small. Before proceeding, we should note the first term of equation (A.5) is identical in the steady-state Bernoulli equation. However, in the absence of circulation, the Bernoulli equation predicts no net force acting on a body in a potential flow (this is known as d'Alembert's paradox). The unsteady potential at any instant is the same as the steady potential with equivalent kinematics. Thus this term may be safely ignored. The second term refers to the translation and rotation of the coordinate system. We recognize that  $\boldsymbol{\Omega} \times \mathbf{r} \parallel \hat{\mathbf{y}}$ , but  $\nabla\phi \parallel \hat{\mathbf{x}}$ . Therefore  $\boldsymbol{\Omega} \times \mathbf{r} \cdot \nabla\phi = 0$ , and this term may also be ignored.

Next we consider  $\mathbf{V}_0 \cdot (\nabla\phi_2 - \nabla\phi_1)$ , with  $\mathbf{V}_0 = U[\cos(\alpha)\hat{\mathbf{x}} + \sin(\alpha)\hat{\mathbf{y}}]$ . Taking the gradient

of equation (A.18) yields

$$\nabla\phi_a(x) = U \left( \cos\alpha \pm \frac{2x \sin\alpha}{c\sqrt{1-(2x/c)^2}} \right) \hat{x}; \quad (\text{A.19})$$

$$\mathbf{V}_0 \cdot (\nabla\phi_{a+} - \nabla\phi_{a-}) = 2U^2 \cos\alpha \frac{2x \sin\alpha}{c\sqrt{1-(2x/c)^2}}. \quad (\text{A.20})$$

Let us now compute the net force<sup>2</sup> acting across the airfoil surface due to this term:

$$\begin{aligned} F &= \int_{-c/2}^{c/2} \Delta p \, dx \\ &= 2U^2 \cos\alpha \int_{-c/2}^{c/2} \frac{2x \sin\alpha}{c\sqrt{1-(2x/c)^2}} \, dx = 0. \end{aligned}$$

The only remaining contribution comes from  $\Delta\dot{\phi}$ . Thus, the force acting perpendicular to the airfoil can be reduced to

$$F_{a\perp} = \int_{-c/2}^{c/2} \rho \frac{\partial\Delta\phi_a}{\partial t} \, dx \quad (\text{A.21})$$

$$= \rho \frac{\pi c^2}{4} [\sin(\alpha)\dot{U} + \dot{\alpha} \cos(\alpha)U] \quad (\text{A.22})$$

where  $\Delta\phi_a$  is the difference in potential between the top and bottom surfaces.

### A.3 Rapidly rotating airfoil

Next, we consider the added-mass force due to rapid rotation of an airfoil about a position  $x_p$  from the leading edge. We start with a circular cylinder of radius  $R$  initially centered at the origin as before, but this time rotating at a rate  $\dot{\alpha}$  (counterclockwise) about a point to be determined (figure A.1).

Before proceeding, we must recognize the rotation point  $x_p$  maps to *two* points along the cylinder surface<sup>3</sup>. Using the relation  $2x_p/c = \cos\theta_p$ , we denote these points as  $\pm\theta_p$ , representing the angle clockwise from the  $-\chi$  axis. However, a cylinder in solid body rotation cannot rotate about both points simultaneously. This issue must be addressed, but for now

<sup>2</sup>All forces describes in this appendix are actually forces per unit span

<sup>3</sup>one for the top surface of the airfoil, the other for the bottom surface

we select only one point on the circle's edge as the pivot point, denoted as  $\theta_p$ . We first rotate our coordinate system so that  $\theta_p$  lies along the  $-\chi$  axis. The inverse rotation can be performed before transforming to the plate.

The potential for a cylinder rotating about its edge is given by Sarpkaya (1966). For completeness, an alternative derivation of his result is given below. Starting with conservation of mass for an incompressible fluid, we arrive at Laplace's equation,

$$\nabla^2 \phi = 0. \quad (\text{A.23})$$

We apply the condition that the far field must be unaffected by the movement of the body,

$$\lim_{r \rightarrow \infty} \nabla \phi = 0, \quad (\text{A.24})$$

and the impermeable boundary condition at the body surface,

$$\nabla \phi|_{r=R} \cdot \hat{r} = \mathbf{v}_{\text{spin}}|_{r=R} \cdot \hat{r}, \quad (\text{A.25})$$

where  $\mathbf{v}_{\text{spin}}$  is the velocity of the spinning body at the boundary. Note that in the statement of boundary condition (A.25) we have implied a coordinate system where the center of the cylinder is at the origin. This will only be valid in the case of (a) a cylinder-fixed coordinate system or (b)  $t = 0$  in a lab-fixed frame. However, if (a) is assumed then boundary condition (A.24) is no longer valid. Fortunately, we are lucky in that the boundary condition equation (A.25) has rotational symmetry about the pivot point, and hysteresis can be ignored in the absence of wake effects. Therefore, we need only solve the problem for  $t = 0$ , and can rotate the initial potential counter clockwise by  $\dot{\alpha}t$  to find the instantaneous potential for any  $t$ .

At  $t = 0$ , the spinning of the cylinder induces body velocities entirely in the  $\hat{y}$  direction,

$$\mathbf{v}_{\text{spin}0} = -\dot{\alpha}(x - R)\hat{y}. \quad (\text{A.26})$$

Using  $x = r \cos \theta$  and  $\hat{y} = \sin(\theta)\hat{r} + \cos(\theta)\hat{\theta}$ , equation (A.25) becomes

$$\partial_r \phi|_{r=R} = -\dot{\alpha}(r \cos \theta + R) \sin \theta|_{r=R} \quad (\text{A.27})$$

$$= -\dot{\alpha}R \left( \frac{\sin 2\theta}{2} + \sin \theta \right). \quad (\text{A.28})$$

Equation (A.23) in combination with equation (A.25) and equation (A.28) is a Neumann boundary value problem, whose solution for  $\phi$  is unique to within a constant in a simply connected domain (Katz & Plotkin, 2001). Since the boundary conditions are in polar coordinates and separable in terms of the variables  $r$  and  $\theta$ , this problem lends itself to a solution by separation of variables.

We start by assuming

$$\phi = \mathcal{R}(r)\Theta(\theta). \quad (\text{A.29})$$

Then equation (A.23) becomes,

$$\frac{1}{r} \frac{\partial}{\partial r} \left( \frac{1}{r} \mathcal{R}' \right) \Theta + \frac{1}{r^2} \Theta'' \mathcal{R} = 0. \quad (\text{A.30})$$

Separating variables to opposite sides, we have

$$\frac{\Theta''(\theta)}{\Theta(\theta)} = \frac{r^2 \mathcal{R}''(r) + r \mathcal{R}'(r)}{\mathcal{R}(r)} = -\lambda_n^2. \quad (\text{A.31})$$

The step towards a solution is to note that the left side is dependent on  $\theta$  only, while the right side is dependent on  $r$  only, and the only way these two sides can be equal is if they are both equal to the same constant. We give the (possibly infinite) set of constants that satisfy this problem as  $\{\lambda_n^2, n = 1, 2, 3, \dots\}$ . Equation (A.31) yields a second-order, homogeneous linear equation in  $\Theta$ , with a solution

$$\Theta(\theta) = \sum_{n=1,2,3,\dots} A_n \sin(\lambda_n \theta) + B_n \cos(\lambda_n \theta), \quad (\text{A.32})$$

while equation (A.31) yields an Euler second-order differential equation in  $\mathcal{R}$ , with solution

$$\mathcal{R}(r) = \sum_{n=1,2,3,\dots} C_n r^{\lambda_n} + D_n r^{-\lambda_n}. \quad (\text{A.33})$$

For equation (A.33) to satisfy boundary condition (A.24), we have two<sup>4</sup> options: either (1)  $\lambda_n \geq 1$  and  $C_n = 0$  or (2)  $0 \leq \lambda_n < 1$ .

---

<sup>4</sup>In fact, there are two more options:  $\lambda \leq -1$  and  $-1 < \lambda < 0$ . But, in going through these cases, one can easily see that they merely invert the constants  $C_n$  and  $D_n$  and cause  $A_n$  to absorb a negative sign.

Using case (1), boundary condition (A.28) becomes,

$$\sum_{n=1,2,3,\dots} -\lambda_n R^{-\lambda_n-1} (A_n \sin(\lambda_n \theta) + B_n \cos(\lambda_n \theta)) = -\dot{\alpha} R \left( \frac{\sin 2\theta}{2} + \sin \theta \right), \quad (\text{A.34})$$

where, for convenience, we have absorbed  $D_n$  into  $A_n$  and  $B_n$ . Comparing the left side to the right, we see immediately that choosing  $\lambda_1 = 1$  and  $\lambda_2 = 2$  satisfies the boundary condition (and since the solution is unique,  $0 \leq \lambda_n < 1$  is not valid). Therefore, we set  $B_n = 0 \forall n$  and  $A_n = 0, n > 2$ . This generates two equations for the coefficients:

$$-R^{-2} A_1 = -\dot{\alpha} R \Rightarrow A_1 = \dot{\alpha} R^3; \quad (\text{A.35})$$

$$-2R^{-3} A_2 = -\dot{\alpha} \frac{R}{2} \Rightarrow A_2 = \dot{\alpha} \frac{R^4}{4}. \quad (\text{A.36})$$

Thus the potential for the cylinder is

$$\phi = \dot{\alpha} R^2 \left( \frac{R \sin \theta}{r} + \frac{R^2 \sin 2\theta}{4r^2} \right). \quad (\text{A.37})$$

To properly map back to the airfoil, we must first rotate back to the original frame:

$$\phi = \dot{\alpha} R^2 \left( \frac{R}{r} \sin(\theta - \theta_p) + \frac{R^2 \sin(2\theta - 2\theta_p)}{4r^2} \right). \quad (\text{A.38})$$

To determine the pressure gradient using the unsteady Bernoulli equation (Eq. A.5), we need only the potential at the surface of the airfoil. This is found by taking the potential at the surface of the cylinder,

$$\phi|_{r=R} = \dot{\alpha} R^2 \left( \sin(\theta - \theta_p) + \frac{\sin(2\theta - 2\theta_p)}{4} \right) \quad (\text{A.39})$$

$$= \dot{\alpha} R^2 \left( \cos \theta_p \sin \theta - \sin \theta_p \cos \theta + \frac{\cos(2\theta_p) \cos \theta \sin \theta}{2} - \frac{\sin(2\theta_p) \cos(2\theta)}{4} \right). \quad (\text{A.40})$$

We can now map back to the airfoil surface, but must first address the issue brought forward at the beginning of this section. The pivot point  $x_p$  on the airfoil maps to two points on the cylinder surface, at  $\pm\theta_p$ . The  $\cos \theta_p$  terms in equation (A.40) map unambiguously to a single value, since  $\cos(\theta_p) = \cos(-\theta_p)$ . However, the  $\sin \theta_p$  terms are ambiguous.

Xia & Mohseni (2013) used a rotating reference frame argument to circumvent this issue, but the derivation becomes quite complex. However, it is interesting to note that the correct result for the added-mass force can be achieved by *superimposing* the potential flow solutions from rotation about either point, and taking the average, as

$$\bar{\phi} = \frac{\phi_{p+} + \phi_{p-}}{2}. \quad (\text{A.41})$$

We will proceed using equation (A.41), without justification, resting in the comfort that the correct final answer is achieved. However, it must be emphasized that this could be a mere mathematical coincidence. Determining why using a superposition of two rotational “states” yields the correct final potential in this case is an interesting avenue of investigation.

Determining  $\phi_{\theta_{p-}}$  in the same way as before and using equation (A.41), all the  $\sin(\theta_p)$  and  $\sin(2\theta_p)$  terms cancel, while all the other terms from equation (A.40) remain unchanged. Noticing that only rotational velocity has been defined ( $\dot{\alpha}R$ ), we use the map (A.14) to translate back to the airfoil surface. Letting  $x'_p \equiv \frac{c}{2} \cos \theta_p$ , the potential at the surface is

$$\phi_b(x, 0) = \pm \dot{\alpha} \frac{c^2}{4} \left[ 2x'_p/c + \frac{x}{c} (8x_p'^2/c^2 - 1) \right] \sqrt{1 - (2x/c)^2}, \quad (\text{A.42})$$

where the negative and positive portions refer to the top and bottom surfaces, respectively.

Equation (A.5) may be used as before to calculate the pressure gradient across the surface. Again, we ignore the first term due to D'Alembert's paradox. Since the airfoil is not translating, we need only consider  $\boldsymbol{\Omega} \times \mathbf{r} \cdot \nabla \phi$ , which is zero due to the impermeable boundary condition. Once again, only the  $\Delta \dot{\phi}$  term remains. The resulting force is

$$F_{b\perp} = \rho \ddot{\alpha} \frac{\pi x'_p c^2}{4}. \quad (\text{A.43})$$

Here we note that  $x'_p$  refers to a positive distance from the airfoil centre (Fig. 4.1). Defining the distance from the leading edge as  $x_p \equiv cx_p^*$ , and using the relation  $x'_p = c(1/2 - x_p^*)$ , we get

$$F_{b\perp} = \rho \ddot{\alpha} \frac{\pi (1 - 2x_p^*) c^3}{8}. \quad (\text{A.44})$$

## A.4 Total added-mass force

Due to the linearity of potential flow solutions, the total potential will be  $\phi = \phi_a + \phi_b$ :

$$\begin{aligned} \phi(x, 0) = \frac{Uc}{2} \left( \frac{2x}{c} \cos \alpha \pm \sin \alpha \sqrt{1 - (2x/c)^2} \right) \\ \pm \dot{\alpha} \frac{c^2}{4} \left[ 2x'_p/c + \frac{x}{c} (8x_p'^2/c^2 - 1) \right] \sqrt{1 - (2x/c)^2}. \end{aligned} \quad (\text{A.45})$$

To calculate the total force, we can ignore the  $q^2$  terms as per usual. We have also shown that  $\mathbf{\Omega} \times \mathbf{r} \cdot \nabla \phi_{a,b} = 0$  due to the impermeable boundary condition, and that the net pressure contribution from  $\mathbf{V}_0 \cdot \nabla \phi_a$  is zero. Next we consider the contribution of  $\mathbf{V}_0 \cdot \nabla \phi_b$ . We have

$$\begin{aligned} \nabla \phi_b(x, 0) = \pm \dot{\alpha} \frac{c^2}{4} \left[ \left( \frac{1}{c} (8x_p'^2/c^2 - 1) \right) \sqrt{1 - (2x/c)^2} \right. \\ \left. + \left( 2x'_p/c - \frac{x}{c} (8x_p'^2/c^2 - 1) \right) \frac{4x}{c^2 \sqrt{1 - (2x/c)^2}} \right]. \end{aligned} \quad (\text{A.46})$$

$\mathbf{V}_0$  applies a constant term to the above expression, so the total pressure across the airfoil surface is determined by the following integrals:

$$\begin{aligned} \int_{-c/2}^{c/2} \sqrt{1 - (2x/c)^2} dx &= \pi c/4; & \int_{-c/2}^{c/2} \frac{4x}{c^2 \sqrt{1 - (2x/c)^2}} dx &= 0; \\ \int_{-c/2}^{c/2} -\frac{4x^2}{c^2 \sqrt{1 - (2x/c)^2}} dx &= -\pi c/4. \end{aligned}$$

Thus we have

$$p_{tot} = \int_{-c/2}^{c/2} \mathbf{V}_0 \cdot \nabla \phi_{\pm b} dx \quad (\text{A.47})$$

$$= 2U \cos \alpha \dot{\alpha} \frac{c^2}{4} \left[ \frac{1}{c} (8x_p'^2/c^2 - 1) \pi c/4 + 0 - \frac{1}{c} (8x_p'^2/c^2 - 1) \pi c/4 \right] = 0. \quad (\text{A.48})$$

Since only the  $\Delta \dot{\phi}$  terms contribute to forces in either case, the total force will be a simple superposition of these forces (equations A.22 and A.44):

$$F_\phi = \rho \frac{\pi c^2}{4} [\dot{\alpha} \cos(\alpha) U + \sin(\alpha) \dot{U}] + \rho \ddot{\alpha} \frac{\pi (1 - 2x_p^*) c^3}{8}. \quad (\text{A.49})$$

The total normalized added-mass force is therefore

$$C_{F\phi} = \frac{\pi c}{2U_\infty^2} \left( \dot{\alpha} \cos(\alpha) U + \sin(\alpha) \dot{U} - c \ddot{\alpha} (x_p^* - 1/2) \right). \quad (\text{A.50})$$

This is identical to the result for chord-normal non-circulatory force achieved by Xia & Mohseni (2013) and used in chapter 3. Note that  $C_F$  maps to lift and drag as  $C_{l\phi} = C_F \cos \alpha$  and  $C_{d\phi} = C_F \sin \alpha$ . For small  $\alpha$  and steady flow ( $\dot{U} = 0$ ), equation (A.50) generates a lift

$$C_{l\phi} = \frac{\pi c}{2U_\infty^2} (\dot{\alpha}U - c\ddot{\alpha}(x_p^* - 1/2)), \quad (\text{A.51})$$

which is identical to Theodorsen's (1935) famous result.

# Appendix B

## Experimental error

### B.1 Force balance resolution and calibration error

Run-to-run uncertainty in force measurements (sample standard deviation across trials) was previously characterized in chapter 3. In the following, two specific aspects of force transducer measurement error are estimated: resolution error and calibration bias error. The former can be assessed from manufacturer specifications, which list the resolution of the ATI Gamma DAQ force sensor at 6 mN. This corresponds to a force coefficient resolution of 0.003 using the parameters in chapter 3, or approximately 1% of the smallest observed peak in forces. Therefore, transducer precision is not a significant source of error.

The calibration error of the force transducer may be assessed directly by comparing a known applied force to the output recorded by the transducer, such as by loading the force balance with a standardized weight. However, this calibration test was not performed at the time of experimentation. As the force balance has been used numerous times since, any calibration error (or lack thereof) measured at present may not be a good representation of the error at the time of experimentation. Instead, as a first approximation, calibration bias error will be assessed by comparing chapter 3 steady measurements at constant angles of attack to forces previously measured on NACA0012 profiles at similar  $Re$ . Moreover, lift coefficients from symmetrical profiles will follow the theoretical trend of  $2\pi\alpha$  prior to the onset of stall; this theoretical trend provides a standard to which experiments may be compared.

Lift coefficients for the NACA0012 profile were collected from two external sources. Critzos et al. (1955) measured lift at  $Re = 5 \times 10^5$  for an aspect-ratio 6 airfoil that completely spanned their wind tunnel. NACA0012 airfoil data for  $10^4 < Re < 10^5$  and low  $\alpha$  could not

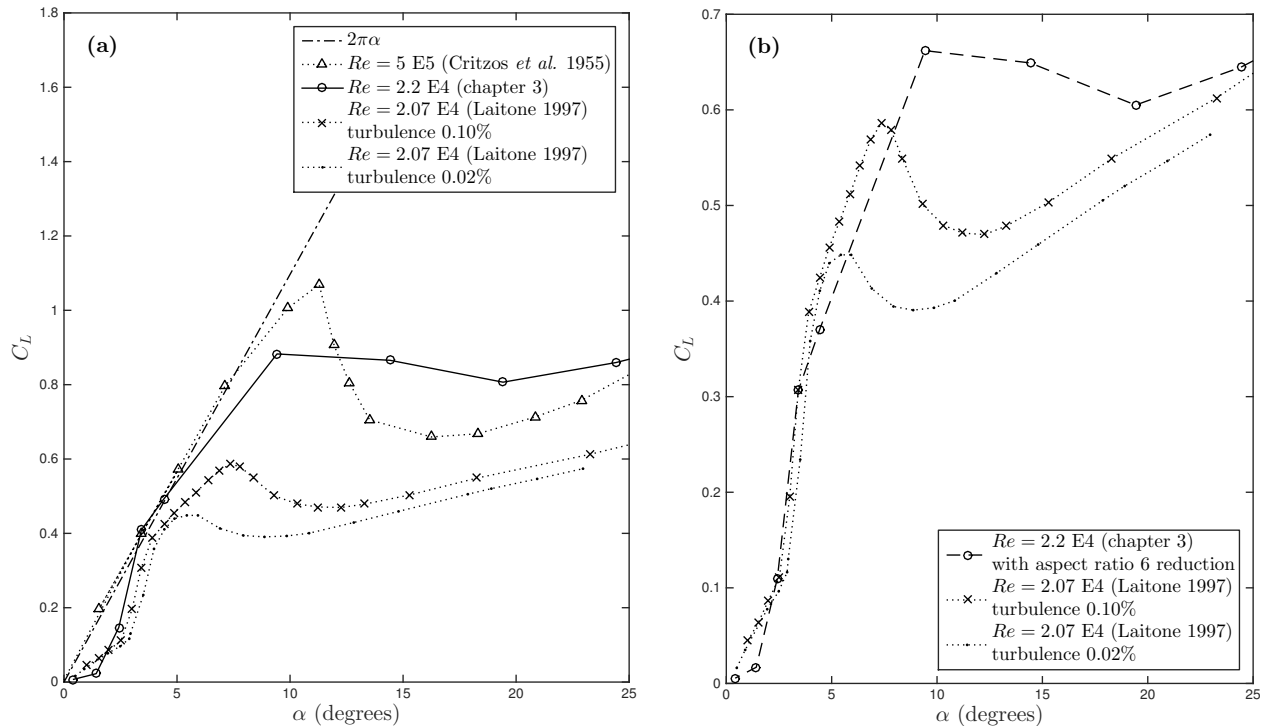


Figure B.1: A comparison of lift coefficients from a variety of sources for the NACA0012 profile. **(a)** Lift coefficients from chapter 3 steady lift measurements at  $Re = 2.2 \times 10^4$  and pre-stall angles of attach ( $\alpha < 10^\circ$ ) follow the trend of  $2\pi\alpha$  and are bounded from above by lift coefficients measured at  $Re = 5 \times 10^5$ , in accordance with theoretical expectations. Results from an aspect-ratio 6 wing (Laitone, 1997) at two turbulence levels are comparatively reduced. **(b)** Airfoil lift from chapter 3 has been reduced by the factor 6/8, in accordance with equation B.1 using the aspect ratio of the wing used by Laitone (1997). The reduced airfoil and wing lift are in close agreement, validating chapter 3 measurements and indicating that calibration error is small.

be found in the literature, however Laitone (1997) measured forces on a NACA0012 wing (aspect ratio 6) for  $\alpha < 24^\circ$  at  $Re = 2.07 \times 10^4$ . These sources provide lift coefficients at Reynolds numbers above and below the value of  $Re = 2.2 \times 10^4$  used in chapter 3 on an airfoil with an aspect ratio of 8.7. The lift coefficients from all these sources are compared in figure B.1a.

Prior to the onset of stall, lift coefficients follow the theoretical trend of  $C_L = 2\pi\alpha$  (figure B.1a) for the highest  $Re$  and for the steady measurements from chapter 3. The  $Re = 2.07 \times 10^4$  results from a NACA0012 wing (Laitone, 1997) do not follow this trend, which is in accordance with reductions in lift associated with tip vortex losses. As chapter 3 measurements are close to the theoretical predictions for low  $\alpha$ , this provides confidence that the measured values are reasonable and that calibration bias, if present, is small.  $Re = 5 \times 10^5$  measurements exhibit a higher stall angle and peak lift than the  $Re = 2.2 \times 10^4$  case; this is again in accordance with theoretical predictions and further validation of the experimental results.

Additional validation of chapter 3 results is attained by introducing the appropriate correction factor for comparing airfoil and wing data. Assuming an elliptical circulation distribution, lifting line theory predicts finite-span symmetrical wings exhibit lift coefficients as

$$C_{L3D} = C_{L2D}(\alpha) \left( \frac{AR}{AR + 2} \right), \quad (\text{B.1})$$

where  $C_{L3D}$  is the lift coefficient for the three-dimensional wing,  $C_{L2D}(\alpha)$  is the two-dimensional lift coefficient at a given angle of attack, and  $AR$  is the wing aspect ratio (Perry, 1952). Since the wing used by Laitone (1997) had an aspect ratio of 6, we would expect the lift coefficients of the airfoil in chapter 3 to agree with those of the wing if the former are reduced by a factor 6/8. Indeed, implementing this reduction causes the wing and airfoil results to collapse (figure B.1b), especially using wing lift coefficients at the higher turbulence level.

The stall-induced drop in lift occurs around  $\alpha = 10^\circ$  for the  $Re = 22\,000$  airfoil, as

opposed to around  $7^\circ$  at the highest turbulence level (0.1%) for the  $Re = 20\,700$  wing. The increase in stall angle in the chapter 3 experiments as compared to Laitone (1997) may be due to increased turbulence in the airfoil experiments or differences in model roughness; however, roughness and turbulence were not characterized in chapter 3. Therefore, comparisons in lift coefficients should be made before and after stall.

At post-stall angles of attack, reduced airfoil lift approaches wing lift (figure B.1b). For pre-stall angles of attack, the largest discrepancy between reduced chapter 3 airfoil lift coefficients and the results of Laitone (1997) is less than 0.05, or about 8% of the reported peak lift in the reduced airfoil data. This error is of the same order as run-to-run uncertainty in forces (which were reported up to 8% of peak values). The reduced airfoil lift oscillates around the results of Laitone (1997), the former being occasionally smaller than the latter ( $\alpha < 3^\circ; \alpha = 5^\circ$ ), and occasionally greater than the latter ( $\alpha = 3^\circ, 4^\circ; \alpha \geq 20^\circ$ ). However, calibration error should generate a consistent bias in forces rather than random scatter. Since the maximum discrepancies between the reduced lift coefficients from the airfoil and lift coefficient from the wing are of the same order as run-to-run uncertainties and do not exhibit a consistent bias, it is concluded that calibration error is small relative to random errors in force measurements.

## B.2 Uncertainty in angle of attack

A cycloidal function was chosen for the experiments in chapter 3 to establish finite jerk at the start and end of rotation. This was important to avoid unbounded added-mass forces, which depend on the second time derivative of angle of attack. However, prescribing this function using a Velmex VXM motor controller was difficult, given the command syntax. This led to some discrepancy between the cycloidal function and the actual position. As forces were measured in a wing-fixed frame, establishing instantaneous angle of attack is important for determining lift and drag accurately.

Two methods were used to establish the discrepancy between the cycloidal function and the actual rotational position: (1) determining instantaneous angle of attack using PIV raw video data and (2) determining the commanded position based on the Velmex command syntax. Because PIV was performed solely on the  $\Xi = 1/2$  and  $\Xi = 1/4$  cases, the error was established for those two cases only.

Determining rotational position for each video frame would be tedious, and the trailing edge was not visible in all frames due to shadowing. Instead, error in angle of attack was assessed by considering the difference in airfoil angle between two frames. For  $\Xi = 1/2$ , it was first assumed that most error would come about from position lag and would compound through the motion. Therefore, angle of attack was measured at  $t^* = 0$  as well as the last frame where the trailing edge was visible ( $t^* = 0.73$ ). Five out of ten videos were analyzed. The angle of attack according to the video was on average  $+2^\circ$  from the angle of attack of the cycloidal at  $t^* = 0.73$  (standard deviation =  $\sigma = 0.8^\circ$ ). The standard deviation is close to the stepper motor accuracy of  $0.9^\circ$ , indicating that this error is consistent between trials.

Next, the commanded position was established based on the instructions passed to the Velmex motor. Figure B.2a shows the commanded position against the cycloidal function. At  $t^* = 0.73$ , the expected discrepancy was  $-2^\circ$ , a  $4^\circ$  difference from optical measurements. The largest deviation of  $-5^\circ$  occurs midway through the motion.

Error was established in a similar way for  $\Xi = 1/4$ . It was found in the previous case that the largest error occurred midway through the motion. For the smaller  $\Xi$ , the angle of attack was measured optically at  $t^* = 0$  and  $t^* = 0.5$ . Optical measurements revealed an average bias error of  $+8^\circ$  from the cycloidal function ( $n=10$ ,  $\sigma = 2^\circ$ ). The commanded position was established for this case as before and is shown in figure B.2. The largest error occurs midway through the motion and is  $+13^\circ$ . The  $5^\circ$  difference between commanded position and optically-measured position highlights the difficulty in establishing precise measures of position error, however both methods predict a positive bias in angle of attack relative to

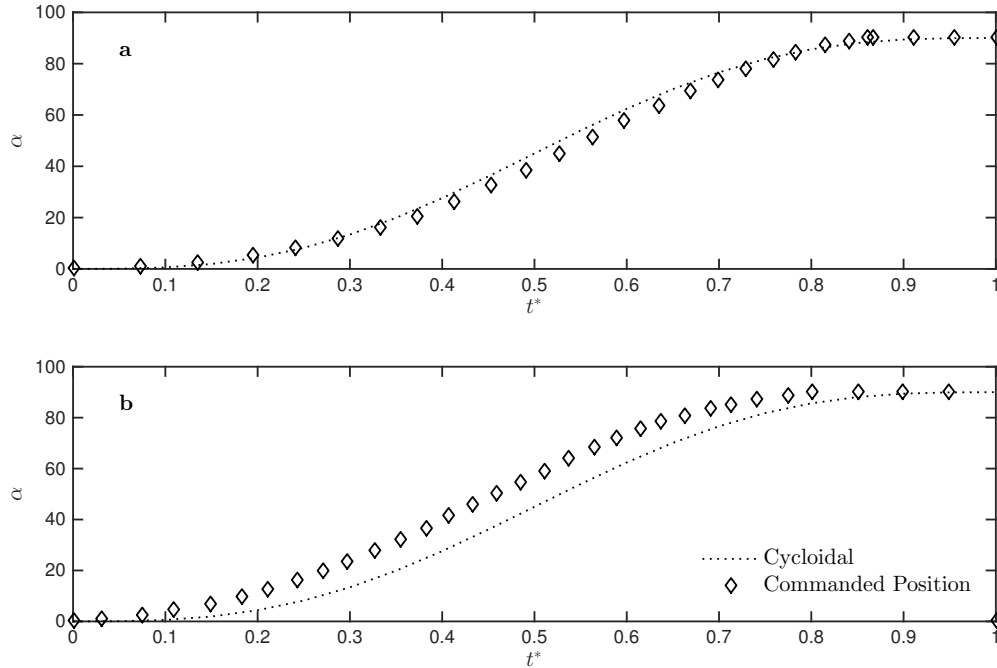


Figure B.2: Rotation error for (a)  $\Xi = 1/2$  and (b)  $\Xi = 1/4$ . Diamonds denote the rotational position of the motor based on the command syntax, while the dotted line is the cycloidal function used to transform forces from the wing-fixed to laboratory frame in chapter 3.  $t^*$  and  $\alpha$  are defined as in chapter 3.

the cycloidal function.

As the cycloidal function was used in chapter 3 to transform forces into the lab frame, an increase in angle of attack relative to the cycloidal would tend to decrease lift and increase drag from the reported values. A key finding in chapter 3 was that peak lift was larger at higher  $Re$  than at lower  $Re$ . We must therefore establish whether a positive bias in the angle of attack would change this conclusion.

The peak lift at  $\Xi = 1/4$  occurred at  $t^* = 0.38$ . The commanded angle of attack at this time gave  $37^\circ$  compared to  $25^\circ$  prescribed by the cycloidal function. As chord-normal forces were multiplied by  $\cos \alpha$  to yield lift, the maximum reduction in peak lift would be  $\cos(37^\circ)/\cos(25^\circ) = 0.88$  times the reported value. However, peak lift at the lower  $Re$  was established as 0.67 times the higher- $Re$  lift. Therefore, while a positive bias in angle of attack would reduce lift, it would not change the central conclusion that higher  $Re$  cases displayed higher lift at intermediate shape change numbers.

The cycloidal function was used to transform force data from the wing-fixed frame to the laboratory frame, as the error in rotational position was difficult to establish precisely and the worst-case bias error does not affect the conclusions of chapter 3.

# Appendix C

## MATLAB scripts

This appendix contains a sample of MATLAB<sup>TM</sup> scripts used for kinematic processing in chapter 4 that may be useful to others performing similar research. The preamble of each script describes the functionality and usage<sup>1</sup>. All scripts and functions were tested on MATLAB<sup>TM</sup> r2014b for Macintosh.

### C.1 A script for batch shape change number calculation

```
%% quick_compute_SCN
% This script quickly batch-computes the shape change number as defined in
% chapter 4. The kinematic data must be in files compatible with DLTdv5,
% and arranged as follows:
% Point 1: Beak/Head
% Point 2: Rump
% Point 3: Wingtip
% Point 4: Shoulder
% Point 5: Most proximal and posterior remige
% Point 6: Perch tips (left-right, separated by one frame)
% Details on how to arrange data files in a directory tree are below.

% Filters all raw position data FIRST, and performs calculations on
% filtered position data. AoA calculated relative to z'

% These are many parameters that may be included in the kinematic
% results array. Options include:
% Xi - The shape change number
% L - average length from beak to rump before the first powerstroke
% Usx, Usz - The x and z components of the speed at t1, the first timestep
%           from which Xi is calculated,
% Ufx, Ufz - The x and z components of the speed at t2, the final timestep
%           to which Xi is calculated
% Uox, Uoz, Uo - The average speed of the center of mass (in x, z and
%               total, respectively) from the end of the ballistic phase to t1
% U1, U2 - The speed of the wing midspan at t1 and t2, respectively
% T - The time period of pitching (t2 - t1)
% Tp - The perching time from the end of the ballistic phase to touchdown
% Ts - The time from the first full extension of the wrist to the flexing
%       of the wrist (regardless of t2, which depends on the last available
```

---

<sup>1</sup>Please email [dtpolet@ucalgary.ca](mailto:dtpolet@ucalgary.ca) with any comments, questions or concerns

```

% timestep at which the wing speed can be calculated)
% V - The shape change velocity: c*(sin(alpha2) - sin(alpha1))/T
% c - The average wing chord measured from t1 to t2
% Sbar - The average wing span, measured from t1 to t2
% alpha1, alpha2 - The angle of attack to the plane perpendicular to z' at
% t1 and t2, respectively
% dx,dz - the total horizontal and vertical displacement of the center of
% mass from t1 to touchdown
% w - this is a WARNING parameter and is ALWAYS included by default. Is 1
% if speed of the mid-wing could not be calculated at t2, is 0 otherwise.
% If 1, will calculate Xi until the last available timestep at which
% speed could be calculated, and T will differ from Ts.

% NOTE ON USEAGE:
% The script requires a few other custom functions: metric, naninterp_cols,
% nan_surround, quickfiltkin and truncateNaN. These are available in
% appendix C.3

clear % Clear the workspace first

% Input the parameters of interest. Seperate by spaces.
Kin_results_cols = ...
'Xi L Usx Usz Ufx Ufz Uo Uox Uoz U1 U2 T Tp Ts V c Sbar alpha1 alpha2 dx dz';

% These values should only be modified once for a whole batch
parent = '~/parent_directory/'; % The parent directory of the data tree
varpend = 1; %Specify whether to append results into Kin_results variable
fc = 50; % The low-pass filter frequency cutoff in Hz. Only used if ~filt
rate = 480; %framerate in Hz
filt = 0; % If true, the script will use data filtered using the
% built-in DLTdv5 algorithm

% This nested cell array represents the data tree holding the kinematic
% data. The variable "sequences" and the associated tree are described in
% detail below.

sequences = ...
{20141022, {{1356, 'a', 0}};...
20141024, {{1204, 'a', 0};{1209, 'a', 'b', 0}};...
20141029, {{1043, 'b', 'g', 'h', 'o', 'q', 1};{1056, 'b', 1};{1110, 'a', 'd', 'e', 1}}...
};

% A schematic of how the data tree holding kinematic data should be organized:
%
%
%                               / perch_a_kin.xyzFilt.csv
%                               | perch_a_kin.xyzpts.csv
% Parent -| date_1  / time_1  / perch_a  -| perch_a
%           -| date_2 -| time_2 -| perch_b  \ key_frames.txt
%           | .      | .      | .
%           | .      | .      | .
%           | .      | .      | .
%                               / perch_last_kin.xyzFilt.csv
%           \ date_m  \ time_n  | perch_last -| perch_last_kin.xyzpts.csv
%                               \ R_g.mat   \ key_frames.txt
%
% Note the order of items in the cell array "sequences":

```

```

% sequences = ...
% {date, {{time1, perch_1, ..., perch_m, use_Rg, }; {time2, perch1, ..., perch_n, use_Rg}}}; ...
% next_date, {{next_time, etc.. }}; .. etc. };
%
% use_Rg refers to whether the set of data should be rotated to gravity
% using a rotation matrix from 'RotateToGravity.m'. This applies to all
% videos at a given 'time'. R-g.mat should be located in the local 'time'
% directory (see schematic above and RotationToGravity.m in Appendix C.2).
%
% Note that a tab-delimited 'key_frames.txt' file should be located in the
% same directory as the 'perch_suffix_kin_xyzpts.csv' file. A
% representative file is shown below:
%
% Touchdown      End ballistic phase  Arm First Straightened  Arm Flexed
% 228            138                    152                     158
%
% The first line are column headers and the second line denotes the video
% frames when the events denoted in line 1 occurred.

%%

Kin_results_cols = [Kin_results_cols, ' w'];
numdates = size(sequences,1);
for i = 1:numdates
    date = num2str(sequences{i,1});
    numtimes = size(sequences{i,2},1);
    disp(['Date is ', date, '; ', num2str(numtimes), ' times']);
    for j = 1:numtimes
        time = num2str(sequences{i,2}{j}{1});
        numperches = size(sequences{i,2}{j},2)-2;
        disp(['Time is ', time, '; ', num2str(numperches), ' perches'])

        use_Rg = sequences{i,2}{j}{numperches+2};
        if use_Rg
            disp('Rotating to gravity for this time')
        else
            disp('Not rotating to gravity for this time')
        end
        for k = 2:numperches+1
            perch = sequences{i,2}{j}{k};
            disp(['Perch ', perch])

            % Import data
            dir = [parent, date, '/', time, '/perch-', perch, '/'];
            if filt
                file = ['perch-', perch, '_kin_xyzFilt.csv'];
                disp('Using data filtered in DLTdv5')
            else
                file = ['perch-', perch, '_kin_xyzpts.csv'];
                disp('Using raw data from DLTdv5')
                [b, a] = butter(2, fc/(rate/2), 'low');
            end

            A = importdata([dir,file]);

```

```

xyz=A.data;

file = 'key_frames.txt';
path = [dir, file];
B = importdata(path);
B = B.data;
tdframe = B(1); ebframe = B(2); arm_st = B(3); dsusframe = B(4);

n = size(xyz,2)/3;
XYZ = NaN(size(xyz,1),3,n+1);
for ii = 1:n;
    XYZ(:, :, ii) = xyz(:, [1 2 3]+3*(ii-1));
end

if use_Rg % Reorient to gravity if specified
    load([parent, date, '/', time, '/R-g.mat']);
    for ii = 1:n+1
        XYZ(:, :, ii) = (R-g*(XYZ(:, :, ii))')';
    end
    disp('Reoriented data to gravity')
end

% assign to different variables and filter
if filt
    filtnames = {'Beakfilt', 'Rmpfilt', 'Wgtpfilt', 'Sldfilt', ...
                'Rmgfilt'};

    s = size(XYZ(:, :, 1));
    for ii = 1:length(filtnames)
        f1 = find(~isnan(XYZ(:, :, ii)), 1);
        eval([filtnames{ii}, ...
              ' = nan_surround(s, naninterp_cols(truncateNaN(XYZ(:, :, ', ...
              int2str(ii), '))), f1);'])
    end
else
    Beakfilt = quickfiltkin(b, a, XYZ(:, :, 1));
    Rmpfilt = quickfiltkin(b, a, XYZ(:, :, 2));
    Wgtpfilt = quickfiltkin(b, a, XYZ(:, :, 3));
    Sldfilt = quickfiltkin(b, a, XYZ(:, :, 4));
    Rmgfilt = quickfiltkin(b, a, XYZ(:, :, 5));
end

% Compute COM displacement and D
COMfilt = (Beakfilt+Rmpfilt)/2;
D = COMfilt(dsusframe, :)-COMfilt(arm_st, :);
D = D/metric(D); % normalize D to its length.
z = [0, 0, 1];
x = D - dot(D, z)*z;
x = x/metric(x);

% Compute angle of attack (to z')
SR = Sldfilt - Rmgfilt;

y = cross(D, z);
zp = cross(y, D);

```

```

zp = zp/sqrt(dot(zp,zp));
AoAHfilt = nan(length(SR),1);
for ii = 1:length(SR)
    AoAHfilt(ii) = 180/pi*(pi/2 ...
        - acos(dot(SR(ii,:),zp)/sqrt(dot(SR(ii,:),SR(ii,:),2))));
end

% Compute c
C = sqrt(dot(SR,SR,2));
C = C(arm_st:dsusframe);
c = mean(C(~isnan(C)));

% Compute dU
MWfilt = (Wgtpfilt + Sldfilt)/2;
S = Wgtpfilt - Sldfilt;
u_MW = NaN(size(MWfilt));
for l=3:length(MWfilt)-2
    u_MW(l,:) = (MWfilt(l-2,:) - 8*MWfilt(l-1,:) ...
        + 8*MWfilt(l+1,:) - MWfilt(l+2,:))/(12/rate);
end

u_MWpl = NaN(size(u_MW));
pl = dot(u_MW,S,2)./sqrt(dot(S,S,2));
for ii = 1:length(pl)
    u_MWpl(ii,:) = S(ii,:)*pl(ii);
end
u_MWpd = u_MW - u_MWpl;

use_t3 = 0; w=0;

U1 = u_MWpd(arm_st,:);
U1 = sqrt(dot(U1,U1));
U2 = u_MWpd(dsusframe,:);
if isnan(U2)
    [fu2, ~] = find(~isnan(u_MWpd),1, 'last');
    U2 = u_MWpd(fu2,:);
    use_t3 = 1;
    t3 = fu2/rate;
    disp(['Warning: No wing velocity at t_2, ',...
        'using last wing velocity'])
    disp(['Will calculate Xi from ', num2str(arm_st/rate), ...
        ' to ', num2str(t3) 's'])
    w=1;
end
U2 = sqrt(dot(U2,U2));

% Compute the average span
Sbar = sqrt(dot(S,S,2));
Sbar = Sbar(arm_st:dsusframe);
Sbar = mean(Sbar(~isnan(Sbar)));

% Calculate the shape change number
dU = U1 - U2;
t1 = arm_st/rate;

```

```

t2 = dsusframe/rate;
T = t2-t1;
alpha1 = AoAHfilt (arm_st)*pi/180;
alpha2 = AoAHfilt (dsusframe)*pi/180;
if use_t3
    T = t3-t1;
    alpha2 = AoAHfilt (fu2)*pi/180;
end
V = c*(sin(alpha2)-sin(alpha1))/T;
a = dU/T;
Xi = V*(sin(alpha2)-sin(alpha1))/(dU);
disp(['Xi is ', num2str(Xi)])

% Compute Uo, L, Tp and Ts
Tp = (tdframe-ebframe)/rate;
Ts = (dsusframe-arm_st)/rate;

u_com = NaN(size(COMfilt));
for ii=3:length(COMfilt)-2
    u_com(ii,:) = (COMfilt(ii-2,:) - 8*COMfilt(ii-1,:) ...
        + 8*COMfilt(ii+1,:) - COMfilt(ii+2,:))/(12/rate);
end
Us = u_com(arm_st,:);
Usx = dot (Us,x);
Usz = dot (Us,z);
if use_t3
    Uf = u_com(fu2,:);
else
    Uf = u_com(dsusframe,:);
end
Ufx = dot (Uf,x);
Ufz = dot (Uf,z);

% Compute Uo
Uo = u_com(ebframe:arm_st,:);
Uo = mean (Uo(~any(isnan(Uo),2),:),1);
Uoz = dot (Uo,z);
Uox = dot (Uo,x);
Uo = metric(Uo);

% Compute L
L = Beakfilt - Rmpfilt;
L = sqrt(dot(L,L,2));
L = L(ebframe:arm_st);
Lsd = std(L(~isnan(L)));
L = mean(L(~isnan(L)));

disp(['Uo is ', num2str(Uo), ' m/s'])
disp(['L is ', num2str(L), ' m'])
disp(['Powerstroke time is ', num2str(Ts), ' s'])
disp(['Perching time is ', num2str(Tp), ' s', char(10)])

% Compute dx, dz
P1 = COMfilt(arm_st,:); % position of bird

```

```

P2 = truncateNaN(XYZ(:, :, 6));
P2 = mean(P2(1:2, :));
dz = P1(3) - P2(3);
dx = sqrt(dot(P1-P2, P1-P2) - dz^2);

% Append to variable
if varpend
    if ~exist('Kin_results', 'var')
        Kin_results = [];
        Trial = cellstr('Trials');
    end
    [ii, ~] = size(Kin_results);
    eval(['Kin_results(ii+1,:) = [, Kin_results_cols, '];']);
    Trial(ii+1) = cellstr([date, ' ', time, ' ', perch]);
end
end
end

%% Separate Kin_results into variables
% If the user would rather store everything in individual variables, rather
% than one big array, running this section does so. Excluding particular
% trials is also optional

% First, clear everything except the important variables
clearvars -except 'Kin_results' 'Kin_results_cols' 'Trial'

% Exclude particular trials and separate values according to column names
% For instance, in the trials below one camera did not work properly
exclude = {'20141022 1356 a', '20141024 1204 a'};
rnge = 1:length(Trial);
k=0;
for i = 1:length(Trial)
    for j = 1:length(exclude)
        if strcmp(Trial{i}, exclude{j})
            rnge(1:end == i-k) = [];
            k=k+1;
        end
    end
end
end

varbles = strsplit(Kin_results_cols);
for i=1:length(varbles)
    eval(['varbles{i}, ' = Kin_results(rnge, i);'])
end

Trial_excl = Trial(rnge);
clearvars i j k varbles

```

C.2 A script for calculating the gravity-based rotation matrix from a falling object.

```

%% RotationToGravity

% In easyWand5, gravitational alignment is achieved by tracking an object
% falling under the influence of gravity. However, the algorithm has some
% setbacks: it requires views of the object from all perspectives at all times,
% and the data points for tracking the object are used to "enhance" the
% calibration. The latter is a great feature if the user is confident that
% the accuracy of object tracking is on the order of wand tracking accuracy,
% but if object tracking was more difficult then the falling object data can
% detract from 3D reconstruction accuracy.

% This script computes the rotation matrix to align an existing calibration
% to gravity. The rotation matrix can then be applied to a set of 3D points
% using the same existing calibration to align the set to gravity.

% Notes on options:
% USE TWO POINTS
% Sometimes one may have better confidence of proper tracking of the center
% of mass if two points on opposite sides of the object are averaged. This
% is especially useful for non-spherical, rotating projectiles.
%
% PLANAR REGRESSION
% To reduce tracking error, the script will optionally first
% compute a planar regression of the data and calculate acceleration in the
% regression plane. This is especially useful if the object takes on a
% large arcing trajectory. Otherwise, the algorithm will simply calculate
% the acceleration from raw data, without first computing planar regression.
%
% LOW-PASS FILTERING
% If enabled, the script performs initial low-pass butterworth filtering on
% the raw 3D data at the specified filter cutoff frequency.

% Some notes on usage:
% -3D tracking of the object should be in the same format as xyz output from
% DLTdv5
% -If using two points, the points used must be points 1 and 2 in DLTdv5
% -If using planar regression, the 'fit_3D_data' function is required:
%   (File ID: #12395)
% -The script will not function correctly if there are intermediate NaN
%   values in between the first and last 3D point. This is because the
%   'mean' function will return a NaN value. Functionality can be added to
%   the script by making the 'mean' function ignore NaN values whenever it is
%   called
% -The script requires a few other custom functions: nan_surround,
% truncateNaN and plot3quick. These are available in appendix C.3

% USER INPUTS:

% dirpath: the path to the folder containing the file. This allows R.g to
% be saved to the same folder
dirpath = '~/parent_directory'; % no '/' on the end.
prefix = 'projectile_'; % The file name up to the default 'xyz.csv' portion
file = [prefix, 'xyz.csv']; % The suffix can be changed if it differs from
% 'xyz.csv', but must be in the same format as

```

```

                                % a 3D points file from DLTdv5.

rate = 480; % frame rate in Hz
use_2pts = 0; % Should COM be computed as the average of 2 points?
planar_reg = 1; % Should planar regression be performed on the data?
use_lp = 0; % Should a low-pass filter also be applied to the data?
Fc = 40; % Frequency cutoff of low-pass filter in Hz

% IMPORT DATA:
clear
A = importdata([dirpath, '/', file]);
xyz=A.data;
n = size(xyz,2)/3;
XYZ = NaN(size(xyz,1),3,n+1);
for i = 1:n;
    XYZ(:, :, i) = xyz(:, [1 2 3]+3*(i-1));
end

if use_2pts
    XYZ(:, :, 1) = (XYZ(:, :, 1) + XYZ(:, :, 2))/2;
end

if use_lp
    s = size(XYZ(:, :, 1));
    XYZfill = truncateNaN(XYZ(:, :, 1));
    [b, a] = butter(2, Fc/(rate/2), 'low');
    f1 = find(~isnan(XYZ(:, :, 1)), 1);
    XYZfilt = filtfilt(b, a, XYZfill);
    XYZ(:, :, 1) = nan_surround(s, XYZfilt, f1);
end

t = (1:length(xyz))/rate;

if planar_reg
    % Perform planar regression
    disp('Using Planar Regression')
    XYZc = truncateNaN(XYZ(:, :, 1));
    [Err, N, P] = fit_3D_data(XYZc(:, 1, 1), XYZc(:, 2, 1), XYZc(:, 3, 1), 'plane');

    % Calculate rotation matrix
    z = [0; 0; 1];
    u = cross(N, z)/sqrt(dot(cross(N, z), cross(N, z)));
    ct = dot(N, z);
    R = ct*eye(3) - (N*z'-z*N') + (1-ct)*kron(u, u');
    XYZr = R*(XYZ(:, :, 1))';

    % Compute accel in trajectory plane
    xy = truncateNaN(XYZr([1 2], :))';
    a=NaN(size(xy));
    for i=3:length(xy)-2
        a(i, :) = (-xy(i-2, :) + 16*xy(i-1, :) -30*xy(i, :) + 16*xy(i+1, :) ...
            - xy(i+2, :))/(12/rate^2);
    end
    am = mean(a(~any(isnan(a), 2), :));

```

```

disp(['Acceleration due to gravity is ', ...
      num2str(sqrt(dot(am,am)), 4), ' m/s^2'])
am = am/sqrt(dot(am,am));

else
disp('No Planar Regression')
XYZc = truncateNaN(XYZ(:, :, 1));

a=NaN(size(XYZ(:, :, 1)));
for i=3:length(XYZ)-2
    a(i, :) = (-XYZ(i-2, :, 1) + 16*XYZ(i-1, :, 1) -30*XYZ(i, :, 1) ...
              + 16*XYZ(i+1, :, 1) - XYZ(i+2, :, 1))/(12/rate^2);
end

am = mean(a(~any(isnan(a), 2), :), 1);
disp(['Acceleration due to gravity is ', ...
      num2str(sqrt(dot(am,am)), 4), ' m/s^2'])
am = am/sqrt(dot(am,am));
quiver3(xyzm(1), xyzm(2), xyzm(3), am(1)/10, am(2)/10, am(3)/10, 'r')
R = [eye(3); [0 0 0]];
end

% Compute new rotation matrix for 3D data
z_r = R'*(-[am';0]); %the real z-axis.
z = [0;0;1]; %the z-axis of the non-gravity-oriented calibration
v = cross(z_r, z)/sqrt(dot(cross(z_r, z), cross(z_r, z))); %the rotation axis
ct = dot(z, z_r);
R_g = ct*eye(3) + (z*z_r' - z_r*z') + (1-ct)*kron(v, v');

XYZ_r = R_g*(XYZ(:, :, 1))';

% Plot various diagrams to assess the validity of results
close all
if planar_reg
    % Displays the data in the trajectory plane, with each instantaneous value
    % of acceleration and the mean value of acceleration. First data point
    % is in green, final data point is in red.
    figure(1)
    hold on
    plot(xy(:, 1), xy(:, 2), 'bo')
    plot(xy(1, 1), xy(1, 2), 'go')
    plot(xy(end, 1), xy(end, 2), 'ro')
    axis equal
    quiver(xy(:, 1), xy(:, 2), a(:, 1), a(:, 2))
    xym = mean(xy);
    am = mean(a(~any(isnan(a), 2), :));
    am = am/sqrt(dot(am, am));
    quiver(xym(1), xym(2), am(1)/20, am(2)/20, 'r')
    title('Instantaneous and mean Acceleration in the trajectory plane')

    % Displays the raw data, data transformed to the trajectory plane, and data
    % transformed to the gravitational reference frame. Arrows point in the
    % direction of z in each frame.
    figure(2)

```

```

hold on
plot3quick(XYZ,'bd')
plot3quick(XYZr','go')
plot3quick(XYZ_r','rs')
arp = mean(truncateNaN(XYZ(:,:,1))); arl = z_r/10;
quiver3(arp(1),arp(2),arp(3),arl(1),arl(2),arl(3),'b')
arp = mean(truncateNaN(XYZr')); arl = -[am';0]/10;
quiver3(arp(1),arp(2),arp(3),arl(1),arl(2),arl(3),'g')
arp = mean(truncateNaN(XYZ_r')); arl = R_g*z_r/10;
quiver3(arp(1),arp(2),arp(3),arl(1),arl(2),arl(3),'r')
legend('Initial reference frame', 'Trajectory plane',...
      'Gravitational reference frame')
axis equal

else
% Displays the data in the initial reference frame, with each
% instantaneous value of acceleration and the mean value of acceleration.
% First data point is in green.
hold on
plot3quick(XYZ(:,:,1),'bo')
plot3quick(XYZ(find(~isnan(XYZ),1),:,1),'go')
axis equal
quiver3(XYZ(:,1,1), XYZ(:,2,1), XYZ(:,3,1), a(:,1), a(:,2), a(:,3))
xyzm = mean(truncateNaN(XYZ));
am = mean(a(~any(isnan(a),2),:));
am = am/sqrt(dot(am,am));
quiver3(xyzm(1),xyzm(2),xyzm(3), am(1)/10,am(2)/10,am(3)/10,'r')

% Displays the raw data and data transformed to the gravitational
% reference frame. Arrows point in the direction of z in each frame.
figure(2)
hold on
plot3quick(XYZ,'bd')
plot3quick(XYZ_r','rs')
arp = mean(truncateNaN(XYZ(:,:,1))); arl = z_r/10;
quiver3(arp(1),arp(2),arp(3),arl(1),arl(2),arl(3),'b')
arp = mean(truncateNaN(XYZ_r')); arl = R_g*z_r/10;
quiver3(arp(1),arp(2),arp(3),arl(1),arl(2),arl(3),'r')
legend('Initial reference frame', 'Gravitational reference frame')
axis equal
end

%% Save your rotation matrix!
save([dirpath, '/', 'R_g.mat'],'R_g')

```

### C.3 Smaller functions called by the larger scripts

```

function [ V ] = metric( v )
%METRIC computes the Euclidean length of a vector v
V = sqrt(dot(v,v));
end

```

```

function B = nan_surround( s, A, n)
%NAN_SURROUND surrounds the input array with nans
% Takes an input array 'A' and places it in a NaN array of size s,
% starting at the nth row.
temp = NaN(s);
sz = size(A);
temp(n:(n+sz(1)-1), :) = A;
B = temp;
end

function X = naninterp_cols(X)
% Interpolate over NaNs along columns of a two-dimensional array
% See INTERP1 for more info
% Based on 'naninterp' by E. Rodriguez (2005). File ID: #8225.
ncol = size(X,2);
for i = 1:ncol
    X(isnan(X(:,i)),i) = interp1(find(~isnan(X(:,i))), ...
                                X(~isnan(X(:,i)),i), find(isnan(X(:,i))), 'PCHIP');
end
return

function plot3quick(xyz, varargin)
%plot3quick quickly plots the column vectors of xyz as x, y and z coordi-
% nates, respectively.
% column vectors must be in the order x -> y -> z
% can take as varargin any other string variable input that might be used
% in the 'plot3' function; e.g. 'r:^' or 'Color', 'r'
if nargin == 1
    plot3(xyz(:,1),xyz(:,2),xyz(:,3))
else
    text = '';
    for i=1:nargin-1
        text = [text, ', ', '', varargin{i}, '']; %#ok<*AGROW>
    end
    inp = ['plot3(xyz(:,1),xyz(:,2),xyz(:,3))', text, ''];
    eval(inp)
end
end

function [ XYZfilt ] = quickfiltkin(b,a, XYZ)
%QUICKFILTKIN performs filtfilt on 3D position data with possible NaNs
% interpolates over intermediate NaNs but NOT boundary NaNs
% interpolates over each column seperately
% each column should be X,Y,Z position data in time, respectively

XYZfill = naninterp_cols(truncateNaN(XYZ));
f1 = find(~isnan(XYZ(:, :, 1)), 1);
s = size(XYZ);
XYZfilt = filtfilt(b,a,XYZfill);
XYZfilt = nan_surround(s,XYZfilt,f1);

```

```
end
```

```
function M = truncateNaN(M)
%truncateNaN This function removes NaNs from the start and end of a matrix,
% searching down columns
[i, ~] = find(~isnan(M),1);
[k, ~] = find(~isnan(M),1,'last');
M = M(i:k,:);
end
```

## Bibliography

- Baik, Y., Bernal, L., Granlund, K., & Ol, M. (2012). Unsteady force generation and vortex dynamics of pitching and plunging aerofoils. *Journal of Fluid Mechanics*, 709, 37–68.
- Berg, A., & Biewener, A. (2010). Wing and body kinematics of takeoff and landing flight in the pigeon (*Columbia livia*). *Journal of Experimental Biology*, 213, 1651–1658.
- Biewener, A. A., Corning, W. R., & Tobalske, B. W. (1998). In vivo pectoralis muscle force-length behavior during level flight in pigeons (*Columba livia*). *The Journal of Experimental Biology*, 201(24), 3293–3307.
- Bonser, R., & Rayner, J. (1996). Measuring leg thrust forces in the common starling. *The Journal of Experimental Biology*, 199(2), 435–439.
- Campbell, N., Reece, J., Urry, L., Cain, M., Wasserman, S., Minorsky, P., & Jackson, R. (2008). *Biology*. Pearson Benjamin Cummings, 8 ed.
- Carruthers, A. C., Thomas, A. L. R., & Taylor, G. K. (2007). Automatic aeroelastic devices in the wings of a steppe eagle *Aquila nipalensis*. *Journal of Experimental Biology*, 210(23), 4136–4149.  
URL <http://jeb.biologists.org/content/210/23/4136.abstract>
- Carruthers, A. C., Thomas, A. L. R., Walker, S. M., & Taylor, G. K. (2010). Mechanics and aerodynamics of perching manoeuvres in a large bird of prey. *Aeronautical Journal*, 114(1161), 673–680.
- Chaplin, S. B. (1974). Daily energetics of the black-capped chickadee, *parus atricapillus*, in winter. *Journal of Comparative Physiology*, 89(4), 321–330.
- Critzos, C. C., Heyson, H. H., & Boswinkle, R. W., Jr. (1955). Aerodynamic characteristics

- of NACA 0012 airfoil section at angles of attack from  $0^\circ$  to  $180^\circ$ . Technical Note 3361, National Advisory Committee for Aeronautics.
- Deng, Y. (2011). *Ancient Chinese Inventions*. Cambridge University Press.
- Dial, K. P. (1992a). Activity patterns of the wing muscles of the pigeon (*Columba livia*) during different modes of flight. *Journal of Experimental Zoology*, *262*(4), 357–373.
- Dial, K. P. (1992b). Avian forelimb muscles and nonsteady flight: Can birds fly without using the muscles in their wings? *The Auk*, (pp. 874–885).
- Doyle, C., Bird, J., Isom, T., Johnson, C., Kallman, J., Simpson, J., King, R., Abbott, J., & Minor, M. (2011). Avian-inspired passive perching mechanism for robotic rotorcraft. In *Intelligent Robots and Systems (IROS), 2011 IEEE/RSJ International Conference on*, (pp. 4975–4980).
- Garmann, D. J., Visbal, M., & Orkwis, P. D. (2013). Three-dimensional flow structure and aerodynamic loading on a revolving wing. *Physics of Fluids*, *25*, 034101.
- Granlund, K., Ol, M., Garmann, D., Visbal, M., & Bernal, L. (2010). Experiments and computations on abstractions of perching. In *28th AIAA Applied Aerodynamics Conference; Chicago, Illinois*, (p. 4943).
- Green, P. R., & Cheng, P. (1998). Variation in kinematics and dynamics of the landing flights of pigeons on a novel perch. *Journal of Experimental Biology*, *201*(24), 3309–3316.
- Hansen, K. L., Kelso, R. M., & Dally, B. B. (2011). Performance variations of leading-edge tubercles for distinct airfoil profiles. *AIAA Journal*, *49*(1), 185–194.
- Hedrick, T. L. (2008). Software techniques for two-and three-dimensional kinematic measurements of biological and biomimetic systems. *Bioinspiration & Biomimetics*, *3*(3), 034001.

- Katz, J., & Plotkin, A. (2001). *Low-Speed Aerodynamics*. Cambridge University Press.
- Laitone, E. (1997). Wind tunnel tests of wings at reynolds numbers below 70 000. *Experiments in Fluids*, 23(5), 405–409.
- Leishman, J. G. (2006). *Principles of Helicopter Aerodynamics*. Cambridge University Press; 2nd ed.
- Maertens, A. P., & Weymouth, G. D. (2015). Accurate cartesian-grid simulations of near-body flows at intermediate reynolds numbers. *Computer Methods in Applied Mechanics and Engineering*, 283, 106–129.
- McCroskey, W. (1982). Unsteady airfoils. *Annual Review of Fluid Mechanics*, 14(1), 285–311.
- Milne-Thomson, L. M. (1968). *Theoretical hydrodynamics*. MacMillan and Co. Ltd, London, 5th ed.
- Moore, J., Cory, R., & Tedrake, R. (2014). Robust post-stall perching with a simple fixed-wing glider using lqr-trees. *Bioinspiration & Biomimetics*, 9(2), 025013.  
URL <http://stacks.iop.org/1748-3190/9/i=2/a=025013>
- Mueller, T., & DeLaurier, J. D. (2001). An overview of micro air vehicle aerodynamics. *Progress in Astronautics and Aeronautics*, 195, 1–10.
- Mugaas, J. N., & Templeton, J. R. (1970). Thermoregulation in the red-breasted nuthatch (*Sitta canadensis*). *Condor*, (pp. 125–132).
- Ol, M. V., Bernal, L., Kang, C.-K., & Shyy, W. (2009). Shallow and deep dynamic stall for flapping low Reynolds number airfoils. *Experiments in Fluids*, 46, 883–901.
- Pennycuik, C. (1996). Wingbeat frequency of birds in steady cruising flight: new data and improved predictions. *Journal of Experimental Biology*, 199(7), 1613–1618.

- Pennycuik, C. J. (1975). Mechanics of flight. In D. S. Farner, & J. R. King (Eds.) *Avian Biology*, vol. 5, (pp. 1–75). Academic.
- Perry, B. (1952). The effect of aspect ratio on the lift of flat planing surfaces. Report E-24.5, DTIC.
- Pierrehumbert, R. (1980). A family of steady, translating vortex pairs with distributed vorticity. *Journal of Fluid Mechanics*, 99(01), 129–144.
- Pitt Ford, C. W., & Babinsky, H. (2013). Lift and the leading edge vortex. *Journal of Fluid Mechanics*, 720, 280–313.
- Provini, P., Tobalske, B. W., Crandell, K. E., & Abourachid, A. (2014). Transition from wing to leg forces during landing in birds. *The Journal of Experimental Biology*.  
URL <http://jeb.biologists.org/content/early/2014/05/08/jeb.104588.abstract>
- Raffel, M., Willert, C., Wereley, S., & Kompenhans, J. (2007). *Particle Image Velocimetry: a practical guide*. Springer, 2 ed.
- Reese, K. P., & Kadlec, J. A. (1982). Determining the sex of black-billed magpies by external measurements. *Journal of Field Ornithology*, 53(4), 417–418.
- Reich, G., Wojnar, O., & Albertani, R. (2009). Aerodynamic performance of a notional perching mav design. In *47th AIAA Aerospace Sciences Meeting*. American Institute of Aeronautics and Astronautics.  
URL <http://dx.doi.org/10.2514/6.2009-63>
- Saffman, P., & Szeto, R. (1980). Equilibrium shapes of a pair of equal uniform vortices. *Physics of Fluids (1958-1988)*, 23(12), 2339–2342.

- Sarpkaya, T. (1966). A theoretical and experimental study of the fluid motion about a flat plate rotated impulsively from rest to a uniform angular velocity. NU-Hydro-Report 027-TS, DTIC Document.
- Selander, R. K., & Johnston, R. F. (1967). Evolution in the house sparrow. i. intrapopulation variation in north america. *Condor*, (pp. 217–258).
- Taylor, G. K., & Adrian, L. R. T. (2014). *Evolutionary Biomechanics: selection, phylogeny, and constraint*. Oxford University Press.
- Theodorsen, T. (1935). General theory of aerodynamic instability and the mechanism of flutter. *NACA Report 496*.
- Theriault, D. H., Fuller, N. W., Jackson, B. E., Bluhm, E., Evangelista, D., Wu, Z., Betke, M., & Hedrick, T. L. (2014). A protocol and calibration method for accurate multi-camera field videography. *The Journal of Experimental Biology*, 217(11), 1843–1848.
- Tobalske, B. W., Altshuler, D. L., & Powers, D. R. (2004). Take-off mechanics in hummingbirds (trochilidae). *Journal of Experimental Biology*, 207(8), 1345–1352.
- Tobalske, B. W., & Dial, K. P. (1996). Flight kinematics of black-billed magpies and pigeons over a wide range of speeds. *Journal of Experimental Biology*, 199, 263–280.
- Tobalske, B. W., Hedrick, T. L., & Biewener, A. A. (2003). Wing kinematics of avian flight across speeds. *Journal of Avian Biology*, 34, 177–184.
- Tobalske, B. W., Warrick, D. R., Clark, C. J., Powers, D. R., Hedrick, T. L., Hyder, G. A., & Biewener, A. A. (2007). Three-dimensional kinematics of hummingbird flight. *Journal of Experimental Biology*, 210(13), 2368–2382.
- URL <http://jeb.biologists.org/content/210/13/2368.abstract>

- Visbal, M. (2012). Flow structure and unsteady loading over a pitching and perching low-aspect-ratio wing. In *42nd AIAA Fluid Dynamics Conference and Exhibit*, June. American Institute of Aeronautics and Astronautics.
- von Kármán, T., & Sears, W. R. (1938). Airfoil theory for non-uniform motion. *Journal of Aeronautical Sciences*, *5*, 379–390.
- Wagner, H. (1925). Über die entstehung des dynamischen auftriebes von tragflügeln. *ZAMM-Journal of Applied Mathematics and Mechanics/Zeitschrift für Angewandte Mathematik und Mechanik*, *5*(1), 17–35.
- Wang, C., & Eldredge, J. D. (2012). Low-order phenomenological modeling of leading-edge vortex formation. *Theoretical and Computational Fluid Dynamics*, (pp. 1–22).
- Weymouth, G., & Triantafyllou, M. S. (2012). Global vorticity shedding for a shrinking cylinder. *Journal of Fluid Mechanics*, *702*, 470–487.
- Weymouth, G., & Triantafyllou, M. S. (2013). Ultra-fast escape of a deformable jet-propelled body. *Journal of Fluid Mechanics*, *721*, 367–385.
- Weymouth, G., & Yue, D.-P. (2011). Boundary data immersion method for cartesian-grid simulations of fluid-body interaction problems. *Journal of Computational Physics*, *230*(16), 6233 – 6247.
- Wibawa, M. S., Steele, S. C., Dahl, J. M., Rival, D. E., Weymouth, G. D., & Triantafyllou, M. S. (2012). Global vorticity shedding for a vanishing wing. *Journal of Fluid Mechanics*, *695*, 112–134.
- Xia, X., & Mohseni, K. (2013). Lift evaluation of a two-dimensional pitching flat plate. *Physics of Fluids*, *25*, 091901.
- Zhou, Z. (2004). The origin and early evolution of birds: discoveries, disputes, and perspectives from fossil evidence. *Naturwissenschaften*, *91*, 455–471.